Nutrient Transport through Submarine Groundwater Discharge on Curaçao

Numerical simulation to estimate the effect of leakage from onsite sewage disposal systems

MSc Thesis - Anne Versleijen

Delft University of Technology

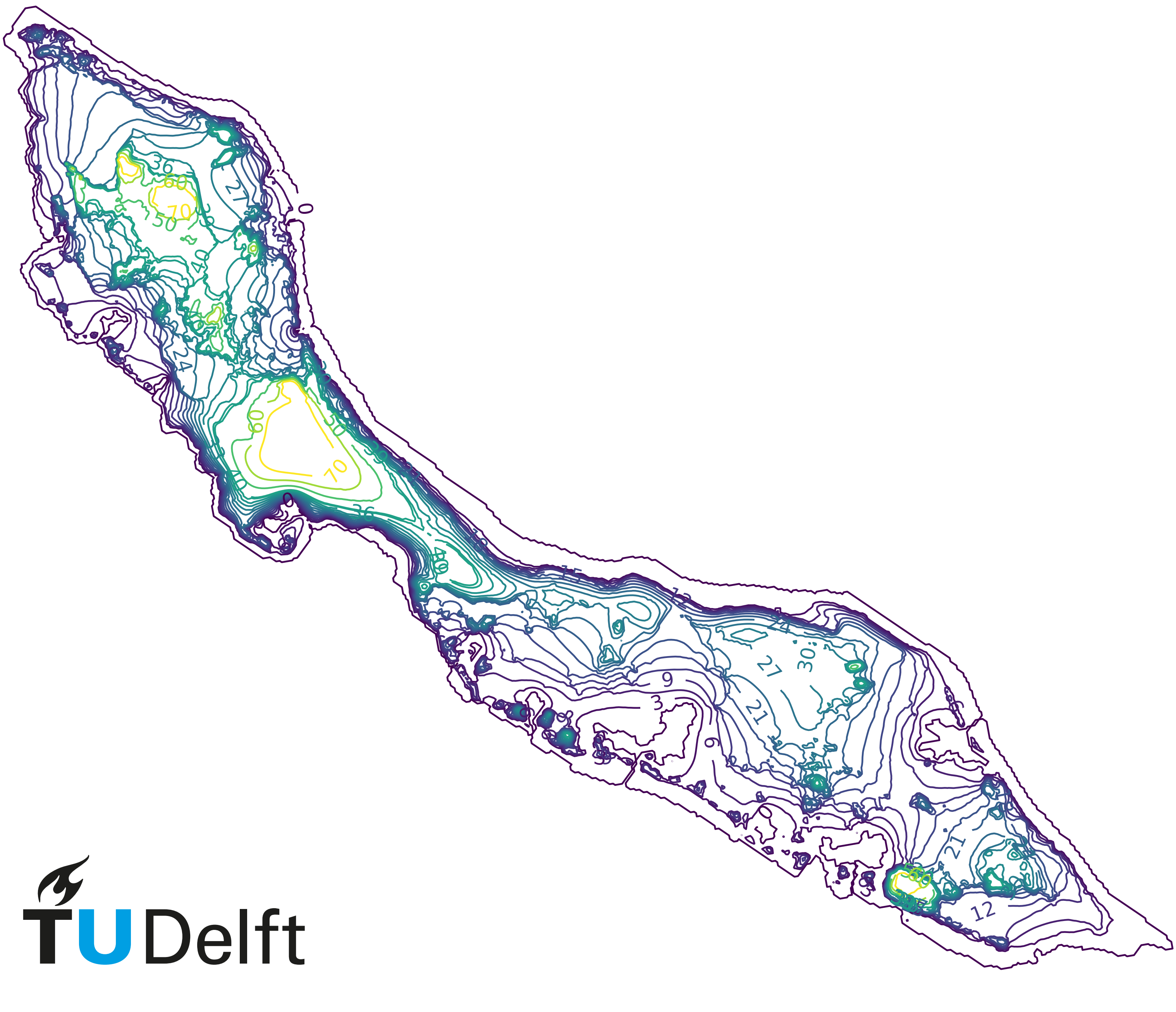

TU Delft

Nutrient Transport through Submarine Groundwater Discharge on Curaçao

Numerical simulation to estimate the effect of leakage from onsite sewage disposal systems

by

Anne Versleijen

to obtain the degree of Master of Science
at the Delft University of Technology,
to be defended publicly on Thursday October 17, 2024 at 13:00 h.

Student number:	4542983	
Project duration:	March 10, 2024 - October 17, 2024	
Thesis committee:	Dr. B. M. van Breukelen,	TU Delft
	Dr. A. Störiko	TU Delft
	M. R. J. Wit	TU Delft, PhD-candidate
Faculty:	Civil Engineering and Geosciences	Delft

An electronic version of this thesis is available at `http://repository.tudelft.nl/`.

TU Delft

Preface

Eight years ago, I started studying in Delft, and I never thought I would become an Environmental Engineer. During my first three years in Delft, I studied Clinical Technology and after successfully finishing this bachelor's programme, I decided take a completely different path and started the bachelor Civil Engineering. I have always been drawn to socially relevant technology, but healthcare did not turn out to be the right direction for me. During the bachelor Civil Engineering, there was also a lot of room to apply technology to societal issues. My interest in water-related problems grew over the years, leading me to choose the Master's program in Environmental Engineering, with the track specialisation Water Resources Engineering. Here, I discovered my affinity for hydrology and its modelling, although water quality issues always kept my interest. This thesis addresses multiple aspects of Water Management, and I was able to further improve my modelling skills. I am eager to apply the knowledge and skills I have developed over the years in my future work.

First of all, I want to thank Boris van Breukelen for his enthusiasm about the project and for proposing interesting research topics within the project. I also want to thank Anna Störiko, I appreciated your critical insights and feedback throughout the project. Your input not only helped me improve my report but also provided me with essential skills for future reporting in my career. Thank you, Mike Wit, for your support throughout my thesis. Your availability for quick questions was greatly appreciated, and your insights into Curaçao and concepts regarding the modelling of groundwater flows and nutrient fluxes were helpful.

In addition, I want to thank my friends and family for being there and making the eight years of studying in Delft unforgettable. I really enjoyed my time here, and these fun times would not have been possible without you. I also want to thank my family and friends who supported me during the thesis, from proofreading to coffee breaks and shared struggles during the thesis period. A special thanks to Karien; you were always there for me to help and talk to. When I felt uncertain and stressed about my work, you reassured me that everything would be fine and that I didn't need to worry. Your enthusiasm for research and talking about it helped me to finish this thesis.

Anne Versleijen
Delft, Friday 11th October, 2024

Summary

Both globally and locally on the island of Curaçao, coral reef degradation is a pressing issue. Coral reefs are of high value, creating fishing and tourism opportunities, and protecting the coastal areas from flooding. However, these ecosystems are threatened by climate change and pollution due to human activities. The latter mostly occurs through pollution of groundwater, elevating the groundwater concentration of nutrients such as Nitrogen (N) and Phosphorus (P). A possible route of this polluted groundwater towards the coastal areas is through submarine groundwater discharge (SGD). In Curaçao, coral reef degradation has reached a level of 50% reef reduction, with expected further degradation. One of the main groundwater polluting factors in Curaçao is the leakage of N and P from onsite sewage disposal systems (OSDS). Limited data is available on these leakage processes, and how the increased nutrient concentrations reach the sea through SGD. With the reef degradation furthering, it is of high importance to gain insight into this pollution process.

The goal of this thesis was to determine the behaviour of nutrient fluxes towards the sea and the bays through SGD on Curaçao. This was done by creating a numerical model in MODFLOW6, which first determined the groundwater head distribution and flow field on Curaçao based on a variable-density model. In this model, simplifications were done and fractured flow was ignored. This flow field was then used in a nutrient transport model to get an insight into the behaviour and fluxes of theoretical nutrient tracers with different reaction characteristics, by performing a spatial and numerical analysis. In addition, the nutrient model was used to simulate the current state of the nutrient levels of N and P in the groundwater resulting from leakage from OSDS, and their progression towards the coastal area. The N and P leakage was based on the average daily excretion of N and P by humans. Furthermore, it was assumed that no removal occurred in the OSDS and it fully leached into the groundwater. N was modelled as conservative transport and with decay with a half-life time of 3 years because of the unknown behaviour of N on Curaçao. P was assumed to sorb to the aquifer material, with retardation factors ranging from 17 to 401. The current state and three future scenarios were performed, consisting of a pollution increase due to population growth, a pollution stop and constant pollution similar to the current state.

The variable-density groundwater flow model succeeded in simulating the distribution of the groundwater heads and the flow pattern, especially on the east side of Curaçao. The flow was greatest along the bays and coastal areas on the east side of the island, as expected due to the presence of weathered Curaçao Lava Formation and limestone in these regions, both with a relatively high hydraulic conductivity. Based on the distribution of the population, which is mainly located on the east side, and the better model performance, it was chosen to focus on the east side for the nutrient simulations.

The spatial tracer analysis showed the Schottegat Bay being vulnerable to nutrient pollution, with a large drainage area, comprising many populated areas. This was confirmed by the simulation of the current state of N and P groundwater concentration as a result of leaking OSDS. The scenario simulations highlighted the immediate and delayed impacts of population growth and stopped pollution on nutrient fluxes. While N-fluxes responded quickly to changes in input, P, due to its sorptive behaviour, showed a delayed response. Although the SGD is equally distributed between the bays and the sea, the nutrient fluxes are relatively higher towards the bays for the current situation (83% for N and 61% for P). In both current and future states, N-concentrations were higher than P-concentrations, due to a higher N-input rate and the sorptive behaviour of P. If leakage from OSDS stops, N as decaying is almost completely flushed out within 25 years. For N with conservative behaviour, the N flux will be reduced by 75% in 2050. For P, it will take much longer to flush out, as after 30 years the outflow is still increasing. If current pollution increases due to population growth, the N-flux increases by 13% and 12% for respectively the conservative and decay simulations. In 2050, or quickly after, the flux will reach a new constant level. Contrarily, the P-flux will continue to increase for the foreseeable future, decreasing the N:P mass ratio.

The model results provided first insights into nutrient fluxes, current pollution, and future scenarios. However, the results are subject to uncertainties because fractured flow and dual-porosity were not included, requiring careful consideration of the results. In addition, future research should refine parameters like hydraulic conductivity, decay constants, and mass loadings, and include an uncertainty analysis. Despite these limitations, the model offered valuable insights into nutrient behaviour and eventually the model could be employed in more realistic simulations, allowing assessment of the future of groundwater pollution and its effect on Curaçao's coral reefs.

Contents

List of Figures

List of Tables

1 Introduction

1.1. Background

1.1.1. Coral reef health on Curacao

Curaçao is an island in the southern part of the Caribbean Sea, which belongs to the Kingdom of the Netherlands. The island is surrounded by coral reefs. These enhance tourism and create opportunities to recreate and fish [1], which generate direct economic value for Curaçao [2]. In addition to the economic benefits, coral reefs also protect the coast from storms and flooding [3]. Over the past decades, the coral reefs of Curaçao have been faced with significant threats. Runoff, pollution, tourism overuse, destructive fishing, and climate change all contribute to coral reef degradation. Over the past 40 years, the coral reefs in the Caribbean have already decreased by 50%, and projections indicate a further decrease, leading to a total loss of 60% within the next 30 years [2].

Eutrophication of seawater represents a significant threat to coral reefs. Elevated levels of dissolved inorganic nitrogen (N) and phosphorus (P) promote phytoplankton blooms that obstruct light from reaching corals [4]. Additionally, these nutrients can stimulate excessive growth of algae, leading to competition with or overgrowth of corals [2]. These circumstances harden the conditions for coral reefs to stay intact. Increased population, industry, agriculture, and onsite sewage disposal system leakage all increase the amount of nutrients and contaminants in seawater [2]. This currently forms a serious threat to coral reef preservation.

Dissolved nutrients and contaminants mainly reach the coral reefs through water flow from the island to the sea. Pollution changes the quality of this water, which subsequently reaches the sea and harms coral reefs. Little information and data is available on the process of polluted water flow on Curaçao. With the pressing issue of coral reef degradation, further analysis of this flow and its subsequent nutrient transport is of high relevance.

1.1.2. Groundwater nutrient flow

Nutrients flow from the island to the sea and coral reefs in two ways; surface and subsurface flow. The first occurs during extreme rainfall in the rainy season when surface contaminants flow overland to the sea. The second, referred to as submarine groundwater discharge (SGD), persists throughout the year [5]. SGD has a relatively high concentration of nutrients, which contributes to 70% of the nutrient discharge of coastal areas globally, even though the volume of SGD is low relative to surface discharge [6]. Due to its relative importance, this study thus focuses on groundwater pollution and the resulting seawater eutrophication through SGD.

Elevated nutrient levels can cause groundwater pollution [7] and are mostly caused by human factors [8]. One mechanism through which human waste contributes to groundwater pollution is the use of septic tank systems and cesspits on Curaçao [9]. Although septic tanks can remove part of the nutrients from wastewater, inadequate maintenance and monitoring results in functionality loss, resulting in nutrient-rich wastewater [10]. Cesspits do not have a treatment functionality and are only used as storage [11]. Leaking of septic tank systems and cesspits, collectively referred to as Onsite Sewage Disposal Systems (OSDS) in the remainder of this work, contributes to elevated nutrient levels in groundwater, resulting in water quality issues in coastal areas [12]. Not all nutrients reach the coast, as reactions in the aquifer material attenuate the nutrient concentration in the groundwater. Depending on the characteristics of the nutrient, sorption and degradation can occur. However, a significant amount of nutrients will enter the sea [9], resulting in potential further coral reef degradation.

Both N and P reaching the sea play a large role in phytoplankton blooms and algae growth, making them key substances of concern. Not only their absolute increased concentrations influence excessive plankton and algae growth. Their relative ratio, the N:P ratio, also regulates the ecosystem production and biological diversity [13]. Changes in this ratio due to different levels of N and P enrichment in groundwater, transported via SGD to coastal waters [14], can shift this regulation.

1.1.3. Modelling of groundwater flow

SGD is a process occurring slowly, diffusely, and is less dependent on the rainy season [15, 16], which is affected by oceanographic processes [17]. Because Curaçao is surrounded by sea, both fresh and saltwater must be considered, as salt water can flow into the aquifer near the coast. Okuhata *et al.* [18] studied the difference between fresh- and saltwater groundwater modelling and found a reasonable head distribution for a freshwater-only model, but the calibrated hydraulic conductivities were unrealistic. In case of nutrient fluxes, hydraulic conductivity has a major role and therefore these models are unsuitable for the simulation of the transport of nutrients.

The main aquifer of Curaçao consists of fractured volcanic basalt. Research on SGD in volcanic islands showed that the high permeability, partly due to fractures and preferential flow paths, leads to SGD dominated by freshwater. This type of SGD contains dissolved species that are not directly recycled from the sea. In contrast, saline SGD consists of recycled nutrients from degraded sediment organic matter and of external nutrient sources entrained from the mix of fresh and saline water [19, 20]. In rocky coastal areas, re-circulation of nutrients and inflowing salt water have a reduced effect. However, given the importance of nutrient fluxes and not only calculating groundwater heads, it is relevant to use a density-based model.

1.2. Research goals and thesis outline

The main goal of the thesis is to determine the behaviour of nutrients flowing towards the sea and bays through submarine groundwater discharge on Curaçao. To assess this both theoretically and through practical application, the goal was divided into two subgoals:

1. Determine the spatio-temporal behaviour of various theoretical tracers (Cl^-, NO_3^-, PO_4^{3-}) with different reaction characteristics and related fluxes through submarine groundwater discharge.
2. Assess the current state and progression of nutrient fluxes from OSDS leakage towards the sea in Curaçao, and evaluate the impact of potential future scenarios on pollutant concentrations.

These two subgoals were explored by using a model of groundwater, SGD, and nutrient flow on Curaçao. As a starting point for the model, the study-site characteristics of Curaçao are explored in Chapter 2, including demographic information, the climate on Curaçao and the geology. Next, three subsequent models are created in MODFLOW6 to reach the final nutrient flow model. A freshwater-only assumption is initially made to calculate the groundwater heads for a constant-density model. These can be used as initial heads for the variable-density model, to incorporate the more realistic density-dependent flows due to the presence of saltwater. In this flow model, the present fractures in the bedrock are not included, and therefore dual porosity was not considered. The groundwater heads and flows of the variable-density model are then used for the nutrient transport model, incorporating not only transport through groundwater flow but also other behaviours such as nutrient sorption and decay. With this model, both the tracer simulations as well as the current state and future scenario simulations are performed. The research structure with the different model components is shown in the overview in Figure 1.1. The governing modelling equations, MODFLOW implementation, tracer simulations, and the simulation of current and future scenarios such as stopped pollution input or increased urban development, are all described in Chapter 3. In Chapter 4, first the results of the groundwater model are presented, comprising of simulated heads and flow fields, along with the performance of the model. For the different tracer and scenario simulations, the groundwater nutrient concentrations as well as nutrient mass flow to the bays and sea are presented, together with their implications. Chapter 5 contains recommendations to enhance the accuracy of the model and relevant model adjustments to perform in future work. Finishing with Chapter 6, where the key findings are described, with an emphasis on the necessary further critical assessment of model parameters and model simplifications before the results can be interpreted as valid.

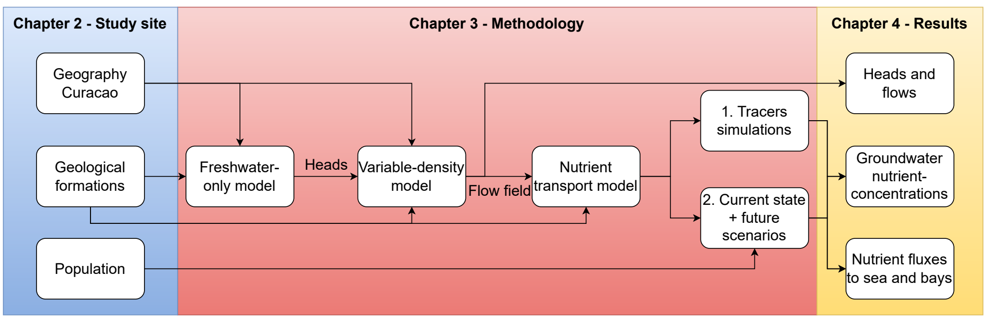

Figure 1.1: Schematic overview of the created models with their inputs and outcomes and in which chapter it is described in this report.

2

Study site

2.1. Curaçao: Geography, Population, and Sanitation

Curaçao is an island located in the southern part of the Caribbean Sea, about 65 km north of Venezuela. It consists of the main island "Curaçao" and a small, uninhabited island "Klein Curaçao". The main island has a surface area of 444 km^2. Willemstad is the capital city and is located on the east side of the island. On the northwest side, the highest elevated area can be found, named the Christoffelberg. The topographic elevation surface of the main island is given in the map in Figure 2.1.

Curaçao has a population of around 150,000 of which two-thirds lives in the city of Willemstad on the east side. The west side is less populated due to its more rural character. Regarding sanitation, 77.1% of households have cesspits, 3.1% use septic tanks, 18% are connected to the sewage system and the reaming is undefined [21]. Only 16% of wastewater on Curaçao is treated by water treatment plants, with a daily capacity of 5100 m^3 d^{-1}, while 84% remain untreated [22]. Part of this untreated wastewater is directly discharged into the sea, while it is also expected that a portion infiltrates in the groundwater and will reach the sea and bays through SGD as a result of the leaking OSDS.

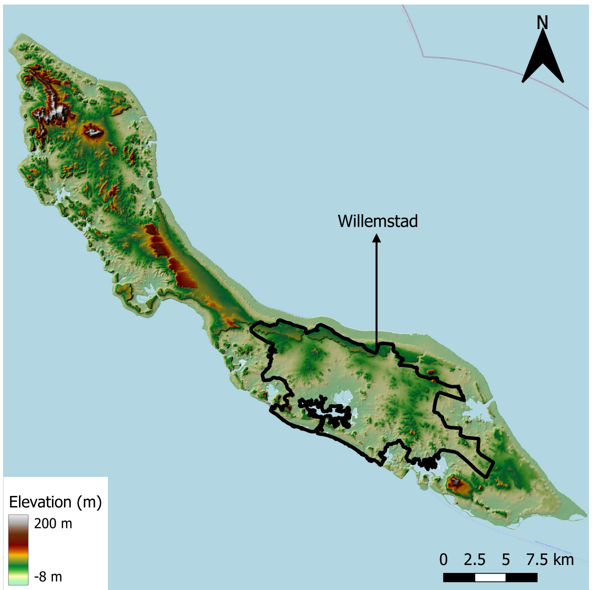

Figure 2.1: Topographic elevation surface of Curaçao, the contour of Willemstad is given in black.

2.2. Climate - Curaçao

Curaçao has a semi-arid climate, with rainfall varying throughout the year [23]. The average annual rainfall is 600 mm [24], mostly occurring in the rainy season from October to December with heavy rain showers [25]. Due to strong wind and a high average temperature of 27 °C, the evapotranspiration rate is high and estimated to be approximately 85-98% of the rainfall [23]. Due to this high rate, the topsoil is dry and therefore the recharge to the groundwater is low. This is estimated to be equal to 3.5% of the annual rainfall [26].

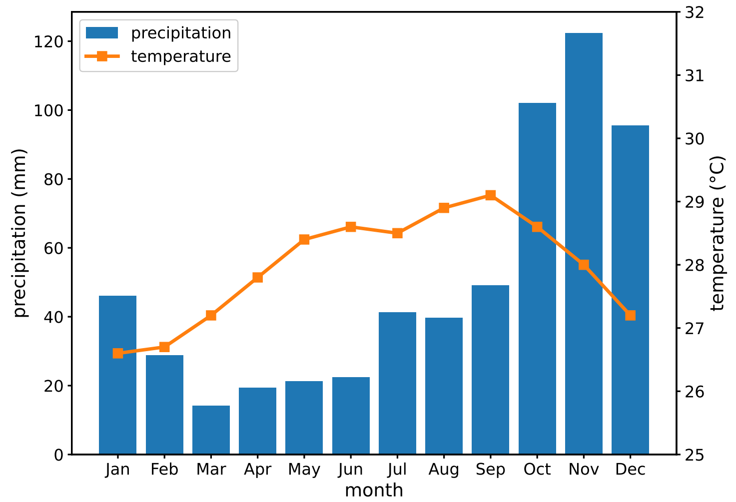

Figure 2.2: Average precipitation and temperature for Curaçao based on climatological data for the period 1981-2010 [24].

2.3. Geology

Curaçao consists of four different geological formations: Curaçao Lava Formation (CLF), Knip Group, Mid Curaçao Formation (MCF) and limestone formation. The distribution of these formations is given in Figure 2.3, with on the left the formations found in the first layers from the surface, and on the right, a simplified distribution based on literature is given for the deeper layers.

2.3.1. Curaçao Lava Formation

A large part of the island is of volcanic origin, called CLF, consisting mainly of thick piles of basalts. CLF is the oldest geological formation on Curaçao and was formed in the early Cretaceous [27]. The formation spans several kilometres in thickness with minimal variation in rock types [28]. It is the most important geological formation on Curaçao because it forms the main aquifer and covers 54% of the island. Despite the span and thickness of CLF, there is barely a distinction in rock types observable.

Due to former humid conditions on Curaçao, the top of the layer is weathered. The vertical extent of this weathered part varies between 6 m and 38 m below the surface [23]. This variation through the island affects the groundwater flow because the weathered part of CLF has a higher hydraulic conductivity than the lower part of the layer.

2.3.2. Knip Group

Following the formation of CLF, the Knip Group developed and is partially overlying it. It is assumed that the Knip Group was formed during the Senonian age. It includes pelagic silica-rich rocks, which originate from oceanic environments and are composed primarily of siliceous material from marine organisms. It also contains clastic sediments, derived from the breakdown of rocks and transported to their deposition site by physical processes [29]. Due to rapid changes in the vertical direction, there are nine different formations found in the Knip Group. The thickness varies over the island, with a thickness of 2000 m in the northwest and decreasing in the direction of south and southeast to a thickness of 100 m.

2.3.3. Mid Curaçao Formation

The Knip Group is followed by MCF which was formed during the Danian stage. MCF consists of four different formations, which mainly include sandstones, siltstones, conglomerates and shales [29], and is contrary to the Knip Group not formed under the influence of the open sea [27]. The formation is located in the central part and on the north side of the southeast part of Curaçao and exceeds 1000 m in vertical direction [30].

2.3.4. Limestone formation

Coral debris accumulated and formed Neogene limestone overlying the former described formations [27]. Loose material was deposited and consolidation and lithification occurred due to submarine conditions as a result of sea level rise [31]. The limestone formation was formed through dissolution and recrystallization of carbonates. 27% of the top surface consists of this, and it is mainly found in the coastal areas surrounding the other geological formations [23]. Part of the limestone is uplifted resulting in the limestone terraces.

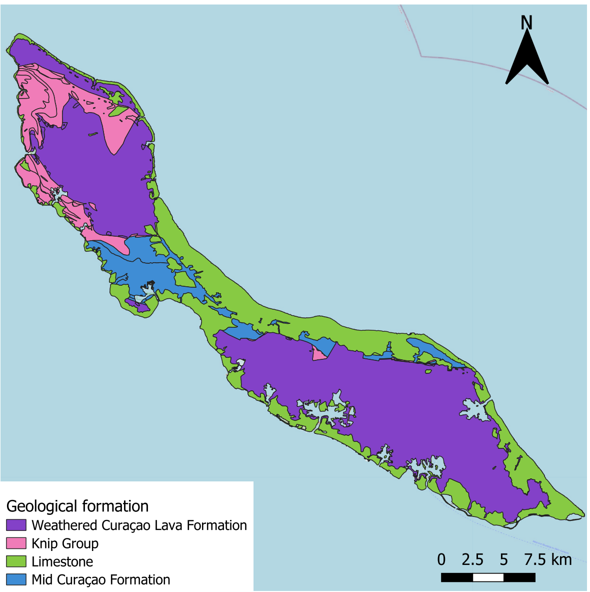

(a) Geological formation found at the surface adapted from [27].

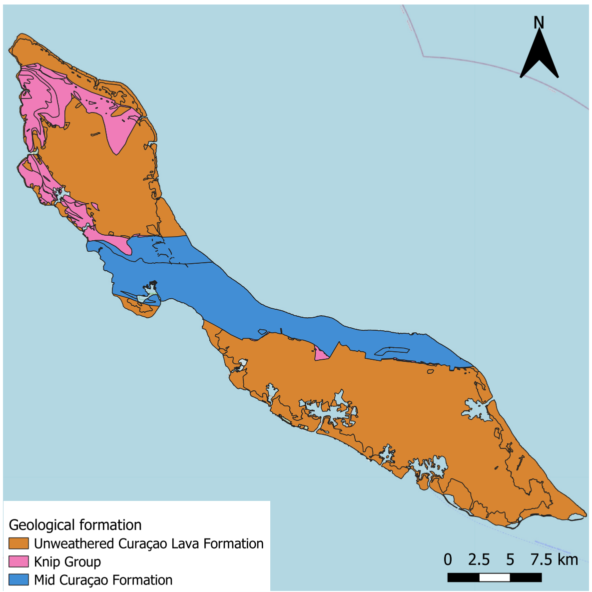

(b) Simplified overview of geological formation found in the deeper layers.

Figure 2.3: Geological formation distribution of Curaçao for the surficial and deeper layers.

3 Methodology

First, the equations necessary to calculate groundwater flow, solute transport and flow based on density differences are explained. Second, the implementation of the study area is described in which the freshwater, variable-density model and nutrient transport model are presented, and their interaction, and dependency on each other's outcomes are explained. Lastly, in the third section, a description of the simulations, which were used to obtain an understanding of the behaviour of nutrients flowing through SGD on Curaçao, is given. In this work, the complex groundwater system of Curaçao was simplified, and fractured flow was not considered. This affects groundwater flow as the system is treated as a single-porosity model, potentially leading to deviations in flow and transport in areas with fractures. The models described in this chapter provide an initial result; however, further critical assessment is necessary before the results can be fully interpreted.

3.1. Governing equations

3.1.1. Freshwater flow

Groundwater movement with a constant density can be described in a three-dimensional direction with Darcy's Law as [32]:

$$\mathbf{q} = -\mathbf{K}\nabla h = -\begin{pmatrix} K_{xx} & 0 & 0 \\ 0 & K_{yy} & 0 \\ 0 & 0 & K_{zz} \end{pmatrix} \nabla h, \tag{3.1}$$

where $\mathbf{q}$ is a vector of the specific discharge (m d^{-1}), $\mathbf{K}$ the hydraulic conductivity tensor (m d^{-1}), in which K_{xx}, K_{yy} and K_{zz} being the hydraulic conductivities along respectively the x-, y-, and z-directions, and ∇h the head gradient vector (-). The distribution of the hydraulic heads is obtained by combining Equation (3.1) with a small-volume water balance, resulting in [32]:

$$\frac{\partial}{\partial x}(K_{xx}\frac{\partial h}{\partial x}) + \frac{\partial}{\partial y}(K_{yy}\frac{\partial h}{\partial y}) + \frac{\partial}{\partial z}(K_{zz}\frac{\partial h}{\partial z}) + W = S_s\frac{\partial h}{\partial t}, \tag{3.2}$$

with the hydraulic head h (m), and W representing the in or outflow of water into/from the system, being positive for inflow and negative for outflow (d^{-1}); this term represents, for example, precipitation, pumping or flow into the boundary. S_s is the specific storage of the material (m^{-1}) and t is time (d). This equation, together with boundary conditions (fixed head or fixed flux) and initial conditions for the heads, describes transient groundwater flow.

3.1.2. Solute transport

The movement of dissolved solutes in groundwater can be described by the accumulation of solute mass, which is equal to the difference between mass entering and mass leaving a specified volume of aquifer [33, 34]. The equation representing this, with processes relevant to this research, is given as [35]:

$$\underbrace{-\nabla\cdot(\mathbf{q}C)}_{\text{Advection}}\underbrace{+\nabla\cdot(S_w\theta\mathbf{D}\nabla C)}_{\text{Dispersion}}\underbrace{-f_m\rho_b\frac{\partial(S_w\overline{C})}{\partial t}}_{\text{Sorption}}\underbrace{-\lambda_1\theta S_w C}_{\text{Decay}}\underbrace{+q_s^{'}C_s + M_s}_{\text{Input}} = \underbrace{-\frac{\partial(S_w\theta C)}{\partial t}}_{\text{Mass storage}}, \tag{3.3}$$

where f_m refers to the fraction of aquifer solid material available for sorptive exchange with the mobile phase under fully saturated conditions; ρ_b is the bulk density of the aquifer material (kg m^{-3}); S_w represents the saturated thickness fraction (-), which is the ratio of the volume of water to the volume of voids; $\overline{C}$ denotes the sorbed concentration of solute mass in the mobile domain (kg kg^{-1}); λ_1 is the first-order decay rate coefficient (d^{-1}); θ denotes the effective porosity of the mobile domain (-), referring to the volume of voids participating in transport per unit volume of aquifer; C is volumetric concentration of the solute (kg m^{-3}); $\mathbf{D}$ is the second-order tensor of hydrodynamic dispersion coefficients (m^2 d^{-1}); $q_s^{'}$ denotes the volumetric flow rate per unit volume of aquifer for mass sources and sinks (d^{-1}), C_s is the volumetric solute concentration of the source fluid (kg m^{-3}); and M_s represents the rate of solute mass loading per unit volume of aquifer (kg m^{-3} d^{-1}).

The movement of solutes in groundwater is primarily governed by advection and dispersion [36]. Advection is the transport of the solute by the bulk motion of water, and is dependent on the effective porosity and the specific discharge:

$$\mathbf{v} = \frac{\mathbf{q}}{\theta}, \tag{3.4}$$

with $\mathbf{v}$ as the velocity of groundwater (m d^{-1}). The spreading of a solute is described by hydrodynamic dispersion, which consists of mechanical dispersion and molecular diffusion [37]. Mechanical dispersion depends on the dispersivity parameters which depend on the observation scale. It describes transport both in the flow direction and perpendicular to the flow, requiring parameters for longitudinal dispersivity in the horizontal plane and the vertical direction, as well as horizontal and vertical transverse dispersivity, to describe the flow. Molecular diffusion is usually assumed to be negligible in practical cases [38].

Next to the flow of a solute, the mass of a solute in a cell can also change due to sorption or decay. With sorption, part of the mass is sorbed to the soil and (temporarily) removed from the groundwater. There are multiple ways to relate the sorbed concentration of sorbed mass ($\overline{C}$) to the concentration of the solute (C), in this work the linear isotherm approach was used. A linear isotherm states that for all solute concentrations, a proportional amount will be sorbed. This is a common way to state equilibrium for the dissolved and sorbed solute and it assumes a proportional relation between the concentration of the sorbed mass and the dissolved solute concentration, given by:

$$\overline{C} = K_d C \tag{3.5}$$

with K_d the distribution coefficient (m^3 kg^{-1}). In addition, it was assumed that sorption was reversible and no degradation occurred. The flow of the solute is then slowed down relative to the water flow by the retardation factor, R, described as:

$$R = 1 + \frac{\rho_b}{\theta} K_d, \tag{3.6}$$

The degradation of a solute is described by first-order decay and the solute is removed from the system. The first-order decay constant can be determined by the half-life time of a solute:

$$\lambda_1 = \frac{ln(2)}{T_{\frac{1}{2}}}, \tag{3.7}$$

with $T_{\frac{1}{2}}$ the half-life time constant (d).

The input of a solute is possible as a water inflow with a certain concentration, for example, contaminated water which infiltrates into the subsurface, or a solute mass can directly be inserted.

These processes together define the mass storage of a solute in a specified volume, which is described by the mass storage term in Equation (3.3). This depends on the water saturation and the fraction in the soil available for flow, defined as the effective porosity.

3.1.3. Variable-density flow

When density-dependent flow is considered, Equation (3.1) changes into [39]:

$$\mathbf{q} = -\mathbf{K}\left(\nabla h + (\frac{\rho}{\rho_0} - 1)\nabla h + (h - z)\nabla \frac{\rho}{\rho_0}\right), \tag{3.8}$$

where ρ_0 represents the density of the reference fluid, in this case freshwater, ρ the density of the water, and z the elevation (m).

The density of the water is dependent on the concentration of salt, which can be calculated with solute mass accumulation in Equation (3.3). Therefore, when considering the variable-density flow, also solute transport should be considered. If the salt concentration is determined, the following equation can be used to calculate the density [40]:

$$\rho = \rho_0 + \frac{\partial \rho}{\partial C}(C - C_0) = \rho_0 + \frac{\rho_{salt} - \rho_0}{C_{salt} - C_0}(C - C_0), \tag{3.9}$$

with ρ_{salt} the density of salt water (kg m^{-3}), C_{salt} the concentration of salt water (kg m^{-3}), C_0 the concentration of the reference fluid (kg m^{-3}) and C the concentration (kg m^{-3}).

3.2. Model implementation in MODFLOW

To solve these equations for a complex system, numerical methods should be used. In this work, MODFLOW 6 was used, which is an open software to create groundwater flow and transport models [41]. MODFLOW uses a control volume finite difference (CVFD) method to solve the equations for a groundwater system. With different packages, which are functionalities of the programme representing different processes, a user can construct a model as desired. MODFLOW was chosen because, besides its wide use in other research, it has a Python package named FloPy to create, run and post-process MODFLOW models [42]. Python can handle and load different file formats, regardless of their size. In addition, it is easy to modify the data, repeat simulations with different input values, and the different steps taken to construct the model are reported which makes it easy to adjust or reproduce and share the model [42, 43].

In MODFLOW, a groundwater system can be modelled by setting up a simulation in which the time and solver settings are defined. A groundwater flow model (GWF) and a groundwater transport model (GWT) can be added to the simulation and connected through exchange or a flow model interface (FMI). The packages which represent the different inputs to solve Equation (3.2) and Equation (3.3), as well as the initial and boundary conditions for solving them numerically, are summarised in 3.1. The total structure of the models with the different packages is given in Appendix A.

Table 3.1: Different packages in MODFLOW which describe the processes and inputs used to solve the flow and solute equations for the groundwater system of Curaçao.

Model	Process	Package
GWF	Discretization	DIS
	Hydraulic conductivity	NPF
	Infiltration/recharge to groundwater	RCH
	Constant head boundary	CHD
	Initial heads	IC
	Concentration to density for variable-density flow	BUY
GWT	Discretization	DIS
	Mass storage, sorption, decay	MST
	Advection	ADV
	Dispersion	DSP
	Mass insertion into model	SRC
	Initial concentration	IC
	Constant concentration boundary	CNC
	Flow model interface	FMI

3.2.1. Spatial discretization and solving

To model the groundwater system of Curaçao, a 3D conceptual model of the geological formations was developed. The surface geological distribution, depicted in Figure 2.3a, was assumed to extend to 20 m below the surface. This was based on the average weathered depth of CLF [30]. The simplified distributions of the deeper layers, as shown in Figure 2.3b, were used to represent the layers below. A representation of this 3D conceptual model is shown in Figure 3.1.

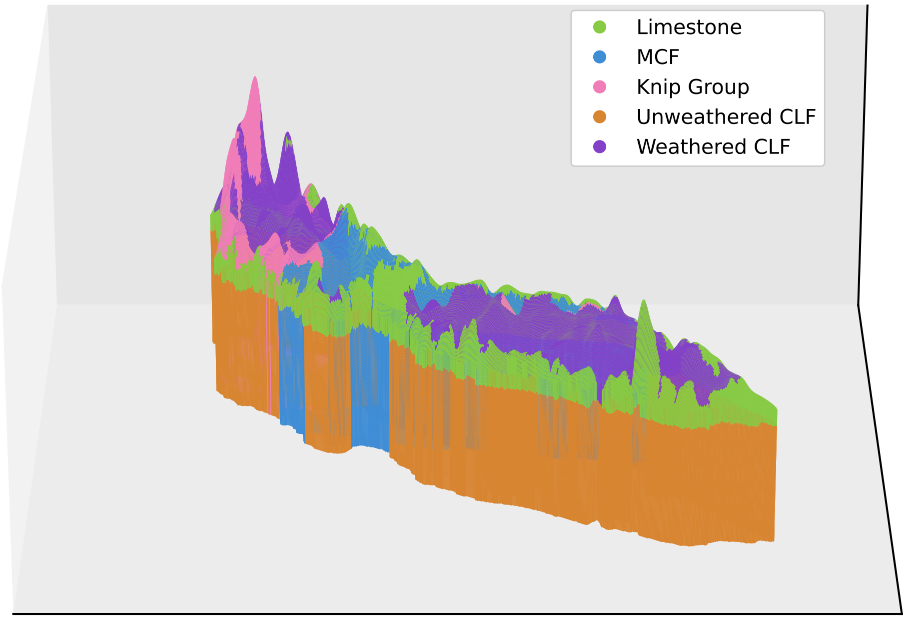

Figure 3.1: 3D conceptual model of the geological formations on Curaçao. CLF = Curaçao Lava formation, MCF = Mid Curaçao Formation.

Spatial discretization is required to solve a groundwater system numerically. The spatial discretization was done by defining the number and size of cells in the x-, y-, and z-direction which correspond in columns, rows, and layers, respectively. Curaçao and the surrounding sea were modelled with a grid of 625 by 175 cells with a cell dimension of 100 m by 100 m. The cell dimensions were based on a convergence analysis, elaborated in Appendix B. This analysis showed convergence of the groundwater heads for cell sizes of 100 m^2 and smaller. Because a further decrease in the cell size would increase computation time, a cell dimension of 100 m by 100 m was chosen.

In the vertical direction, 40 layers were used to represent the geology. More layers improve the accuracy of the variable-density model, but it also increases the computation time. Therefore 40 layers were chosen as a trade-off between accurate outputs for variable-density flow and computation times. The top of the cells of the first layer was defined as the height of the surface obtained from the Digital Elevation Model (DEM) of Curaçao [44]. Before that, the DEM was resampled to the model grid, giving one value for each cell based on the nearest neighbour method. The thickness of the first 10 layers was equal throughout the model and was set to 2 m to fit the first layer of the conceptual model in the model grid. 26 layers were used to divide the depth up to 120 m below sea level and had varying thicknesses. The remaining 4 layers divided the depth from -120 m to -180 m into four layers with a thickness of 20 m. The coarser discretization at the bottom layers was chosen because the flow in this deeper part was less relevant. The 3D conceptual geological model was converted into this discretization, to define the hydrogeological parameters per cell. A cross-section of the model grid in which the geological formation per cell is indicated is given in Figure 3.2, the cross-section is through the east-central part of the island (yellow line in Figure 3.3).

For the orientation of Curaçao, the coordinate system EPSG 32619 was used. The model extended from 472770 to 533865 in the x-direction and from 1324220 to 1374265 in the y-direction. An angular rotation of -35 degrees was added to align the model with the principal direction of the groundwater flow, which improves the computation of the numerical calculations. The full overview of the final discretization and orientation of the model grid is shown in Figure 3.3.

The bays and sea were excluded from the groundwater simulations. Because no elevation data was available for the bays and sea in the DEM, the DEM could be used for marking these cells as inactive. In MODFLOW 6 it is possible to exclude cells from the simulation by setting them to inactive using the IDOMAIN property. All cells with elevation data were marked as active (1), while all cells without data were marked as inactive (0). The active cells were buffered with one cell, and these cells were set to 2 in the IDOMAIN array representing the boundary of

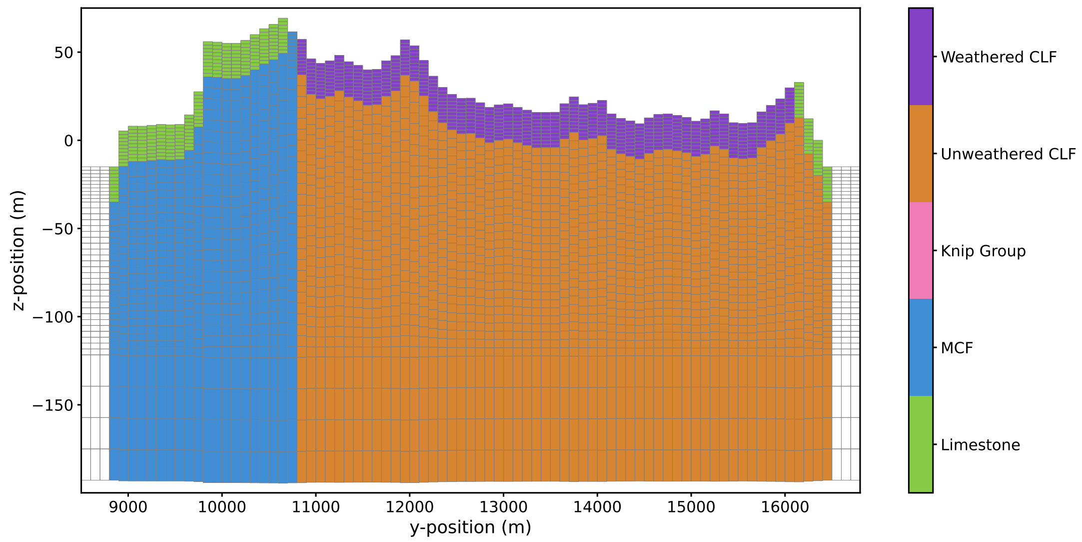

Figure 3.2: Vertical presentation of the conceptual model regarding the geological formations on Curaçao in a cross-section through the east-central part. CLF = Curaçao Lava formation, MCF = Mid Curaçao Formation.

the model, for which boundary conditions could be set (see Figure 3.3). Inconsistencies in resampling the DEM to the current grid size caused numerical instabilities near the coastline and the bays. Therefore, the IDOMAIN array was smoothed manually to prevent these inconsistencies. An example of the initial marking of active and inactive cells in the IDOMAIN along with the manually smoothed marking are depicted in Appendix C.

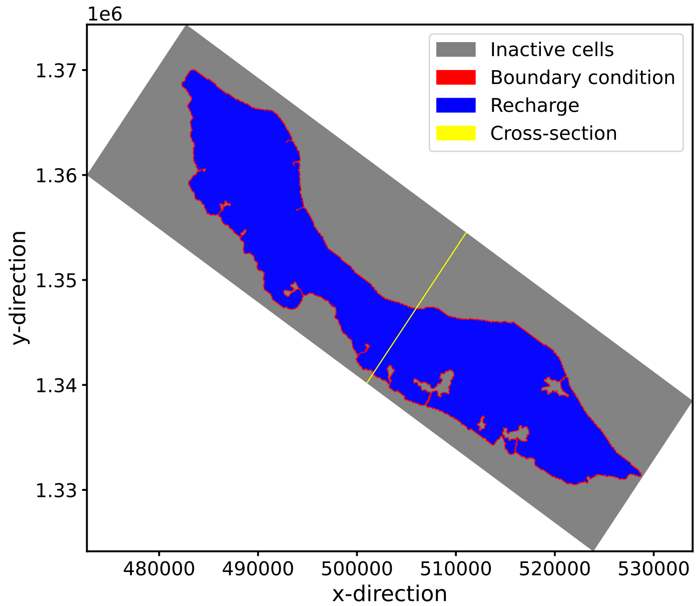

Figure 3.3: Overview of the model grid with active, inactive and boundary cells. The yellow line indicates the location of the cross-section in the east-central part of the island which is used throughout this work.

The 3D geological model was based on 2D information, and literature stating the depths of the different formations. This is a simplification and not the same as the actual situation. The thickness of the weathered part of CLF differs throughout the island but was assumed constant in the model. The thickness was set to the average weathering depth, resulting in over- and underestimating of the depth on locations. Because the conceptual model was used to assign hydrogeological parameters to cells, the values could be an over or underestimation of the parameter compared to the actual situation. For example, above Piscadera Bay (in the east-central part of the island), the weathered depth exceeds 20 m, and thus the weathered depth is underestimated. In contrast, on the eastern side of the island, the weathered depth is less deep, resulting in an overestimation of the thickness of the weathered CLF layer.

3.2.2. Freshwater model

First, a flow model was created which only considered fresh water. This model was used to calculate the steady-state heads resulting from constant-density flow. The hydrogeological parameters used in the model which differ per geological formation are all presented in Table 3.2, and all model parameters assumed as independent on the geological formation are presented in Table 3.3.

Hydraulic conductivity

Freshwater flow through an aquifer depends on its hydraulic conductivity (Equation (3.2)), a property of the geological formation. Hydraulic conductivity was assigned to the cells based on the conceptual geological model (Figure 3.2). The horizontal hydraulic conductivity per geological formation was initially based on pumping tests and literature data and manually iterated until reasonable heads were obtained. The full description of the determination of these values can be found in Appendix D. The hydraulic conductivity of the different layers is heterogeneous and anisotropic. Anisotropy is described as the ratio between the vertical and the horizontal hydraulic conductivity. And therefore an anisotropy value was added to the model (Table 3.3).

Infiltration and abstraction

For water inflow and outflow of the groundwater model, W in Equation (3.2), only rainwater infiltration was considered as recharge to the groundwater. Not all rainfall infiltrates, also a part flows as runoff over the surface and a great part evaporates. Determining the exact amount of infiltration was challenging due to limited available data. Therefore the recharge was estimated based on daily rainfall data and observed groundwater time series. The steady-state groundwater model was converted to a transient model, to compare the simulated heads to the groundwater time series. A description of this process and the results are given in Appendix E. In the scenario where the simulated groundwater heads resemble the observed groundwater heads most, the total recharge was converted to a percentage of the mean annual rainfall for 2021 and 2022, resulting in 7% of the average annual rainfall, equal to 48.65 mm per year. This was added to all the active cells, excluding the boundary cells. The 7% recharge is within the 7-15% range reported for semi-arid regions in the literature [45–47], but it is slightly higher compared to what Louws *et al.* [26] found for Curaçao.

Groundwater abstraction for domestic, agricultural and industrial use was ignored because of limited data. It was assumed that the inflow of water leaking from the OSDS was in the same order of magnitude as the domestic groundwater abstraction, and on approximately the same location and therefore both were excluded. According to Morgan *et al.* [48], 75% of abstracted water is returned as wastewater. The model could be enhanced if the ratio of groundwater extraction to water leakage is known, allowing for the inclusion of groundwater abstraction or nutrient flux in combination with water inflows. Nevertheless, this limitation is considered to have minimal impact on the overall outcomes. In contrast, the exclusion of agricultural and industrial groundwater abstraction affects the groundwater model because at these locations less leakage occurs and therefore the abstraction has a significant effect on the groundwater flows. This is important to assess in future work.

Boundary and initial conditions

There are multiple ways to define the boundary condition of a model. In previous studies on numerical simulations of coastal areas, the sea was both modelled as a constant head boundary (CHD) and a general head boundary (GHB) [49–52]. For a general head boundary, the inflow and outflow are based on the difference between the defined head and the model's simulated head and a specified conductance term. In contrast, a constant head boundary only defines a head allowing water to flow endlessly in and out the boundary to ensure the head at the boundary is maintained at the defined level. This could result in an overestimation of groundwater outflow, as the resistance of the seabed is ignored. Additionally, the seabed's properties can act as a filter or barrier for certain contaminants, resulting in an overestimation of the nutrient discharging in the sea. Given the uncertainty associated with determining the conductance, it was chosen to use the constant head boundary. It was applied to all cells indicated with a 2 in the IDOMAIN array, which represents the sea and bays coastline. The head of this boundary was set to 0 m, which reflected the average sea level height. For the initial conditions, the heads inside the aquifer were set equal to the surface elevation. In further research, the impact should be assessed by incorporating the sea and bays into the model.

3.2.3. Variable-density model

After the freshwater-only model, the variable-density model was created to solve the groundwater flow with the density-dependent flow equation (Equation (3.8)). For this, the solute transport equation was solved to calculate the salt concentration (Equation (3.3))

Effective porosity

The mass storage of a cell depends on the effective porosity, as shown in Equation (3.3). These values were based on literature because no site data were available. Again, as done for the hydraulic conductivity, the effective porosity per geological formation was assigned to the cells based on the conceptual geological model (Table 3.2).

Advection and dispersion

Advection does not depend on extra parameters, because it is the transport based on the specific discharge. To solve the advection, the default numerical scheme "upstream weighting" was used. For dispersion, the coefficients for the dispersion tensor (Equation (3.2)) were required. The longitudinal dispersivity was based on previously performed research in basalt on a large scale, a value of 25 m was chosen for the longitudinal dispersivity for both the horizontal plane and the vertical direction [53]. The transverse dispersivity in the horizontal direction was assigned a fraction of 0.1 of the longitudinal dispersivity, and the transverse dispersivity in the vertical direction a fraction of 0.01 [54, 55]. Because molecular diffusion is negligible on a larger scale [38], the diffusion coefficient was set to 0.

Variable-density flow

The variable-density flow was calculated to define the concentration and density of both salt and freshwater (see Table 3.3). The concentration of saltwater was also used to set the constant concentration boundary for the bays and the sea, as it was assumed that SGD would not affect the salt concentration in the sea and bays.

In addition to potential salt inflow from the sea and bays, the infiltration defined in the flow model was assigned a concentration of 1.2 kg m^{-3}. This value was based on previously conducted electrical conductivity measurements of the groundwater on Curaçao. The median electrical conductivity value (1900 μS cm^{-1}) was converted to salinity [56], and resulted in the concentration of 1.2 kg m^{-3}.

Table 3.2: Hydrogeological parameters for the different geological formations on Curaçao, both literature values and values used in the model are given. In the footnotes of the table, the literature references can be found. CLF = Curaçao Lava Formation, MCF = Mid Curaçao Formation

Geological formation		Weathered CLF	Unweathered CLF	MCF		Knip Group		Limestone
Hydraulic conductivity, K (m d^{-1})	*Literature*	8.56 $\pm$ 15.85[a]	2 $\cdot 10^{-8}$ - 0.03[b]	0.31 $\pm$ 0.21[a]		0.63 $\pm$ 0.91[a]		0.1 - 10000[c]
	Model	0.88 to 9.5	1 $\cdot$ 10^{-2} to 1 $\cdot$ 10^{-4}	0.02		0.3		10
Effective Porosity, θ (-)	*Literature*	0.01-0.15[d]	0.01-0.15[d]	*Sandstone* *Siltstone*	0.04-0.30[e] 0.21-0.41[f]	*Sandstone* *Mudstone*	0.04-0.30[e] 0.14[e]	0.01 - 0.24[f]
	Model	0.05[d]	0.01[d]		0.20		0.14	0.12
Bulk density, ρ_{bulk} (kg m^{-3})	*Literature*	2670-2860[g]	2670-2860[g]	*Sandstone* *Siltstone*	2219[h] 2378[h]	*Sandstone* *Mudstone*	2219[h] 2270[h]	2290-2790[i]
	Model	2670[g]	2860[g]		2300		2240	2500

[a] Based on pumping tests performed by Abtmaier [30].
[b] Values for fresh, unweathered basalt [57, 58].
[c] [59–66]
[d] Effective porosity values for basalt [67–70]
[e] [71]
[f] [58, 72, 73]
[g] Bulk density range found for basalt [74], higher value of range for the deeper layers.
[h] [75]
[i] [76]

Table 3.3: Model parameters which are equal for all geological formations.

Parameter	Unit	Value	Reference
Recharge	mm	48.65	-
Salt concentration recharge	kg m^{-3}	1.2	
Anisotropy (K_v / K_h)	-	0.2	[57]
Longitudinal dispersivity (α_L)	m	25	[57, 58]
The ratio of horizontal transverse dispersivity to longitudinal dispersivity	-	0.1	[54, 55]
The ratio of vertical transverse dispersivity to longitudinal dispersivity	-	0.01	[54, 55]
Freshwater density (ρ_0)	kg m^{-3}	1000	
Saltwater density (ρ_{salt})	kg m^{-3}	1025	
Freshwater concentration (C_0)	kg m^{-3}	0	
Saltwater concentration (C_{salt})	kg m^{-3}	35	[77]
First order denitrification constant (λ_1)	d^{-1}	$6 \cdot 10^{-4}$ d^{-1}	
Distribution coefficient (K_d)	m^3 kg^{-1}	$1.4 \cdot 10^{-3}$	[78]

3.2.4. Nutrient transport

For the nutrient transport simulations, some different parameters were defined compared to the solute part of the variable-density model. The parameters for the mass storage, advection and dispersion term of Equation (3.3) were unchanged. However, different reaction characteristics were added to the simulations, like decay and sorption. An important difference between the nutrient transport model and the variable-density model is that it was assumed that the concentration of the nutrient does not affect the groundwater flow in the nutrient transport model.

Decay and sorption

Nitrate (NO_3^-) can move readily through groundwater and the subsoil, due to their low capacity of sorption [79]. However, NO_3^- can degrade as a result of denitrification, following the equation:

$$5C_{org} + 4NO_3^- + 2H_2O \rightarrow 2N_2 + 4HCO_3^- + CO_2, \tag{3.10}$$

where NO_3^- together with organic carbon reacts and changes to nitrogen, carbon dioxide and bicarbonate. Denitrification can occur in the presence of appropriate microbial populations and an electron donor such as organic carbon, when there is limited dissolved oxygen, and near-saturated conditions [79]. The first-order decay constant is based on the average half-life time of NO_3^- used in previous studies, (see Appendix D for elaboration), and it was converted to a first-order decay constant (Equation (3.7)).

For sorption, the sorb behaviour phosphate (PO_4^{3-}) in groundwater was simulated. This required the bulk density and a distribution coefficient. The bulk density and distribution coefficient used for the different geological formations can be found in Table 3.2. With these parameters, sorption was simulated. In this work, one value was used as the distribution coefficient for all the geological formations due to unavailable data. In future work, it is important to research this further, as it can differ in different geological formations and therefore affect the sorption process. With the bulk density and distribution coefficient, the retardation factor of the different geological layers could be calculated (Equation (3.6)). The resulting retardation factors are presented in Table 3.4.

Table 3.4: Retardation factors of the different geological formations. CLF = Curaçao Lava formation, MCF = Mid Curaçao Formation.

Geological formation	Retardation factor (-)
Weathered CLF	76
Unweathered CLF	401
MCF	17
Knip Group	23
Limestone	30

3.2.5. Solving

To solve the numerical scheme of the groundwater system, it is necessary to apply a solver formulation for the CVFD method. This work employs the Newton-Raphson formulation due to the unconfined conditions of the system. This approach effectively handles the non-linear equations that arise under these conditions. Moreover, it enables water to flow into dry cells while restricting outflow [80]. In this formulation, all cells with a simulated head lower than the cell bottom elevation remain active, unlike in previous versions of MODFLOW, where such cells were treated as inactive. The Newton-Raphson formulation ensures that flow, such as recharge or lateral flow, or mass entering a dry cell, is routed directly downward to the first non-dry cell. This algorithm is referred to as the Newton formulation, which has been consistently shown to be more reliable than the wet/dry method for determining the position of the water table [81, 82]. Using the implementation of the governing equations of Curaçao, the system can be solved with MODFLOW's numerical methods. Three different models were constructed.

The freshwater flow model was used to calculate the steady-state heads. These steady-state heads were used as initial condition for the variable-density model, which was done to improve the convergence of the model. For the initial salt concentration, it was assumed that in each cell the concentration was equal to the salinity of seawater 35 kg m^{-3} [77]. The simulation period was set to 4500 years, with time steps of 1 year. Although the time step of one year was large, this was chosen due to the computation time which increases with the number of time steps (see Appendix F). It was assumed that after 4500 years the steady-state situation was reached, as it is for a transport model not directly possible to set the solver to a steady-state solution.

Due to the scale of the model and its complexity, a transient model was not possible. The downside of this is that transient effects were not considered. An important transient effect is the difference in rainfall throughout the year due to the wet and dry seasons. Although SGD is generally less dependent on rainfall [15, 16], the fractured rock allows heavy rain showers to influence groundwater heads, leading to variations in flow velocities [83, 84].

The outputs of this simulation were the heads after 4500 years and the corresponding flows of the cells. To assess the performance of the model, the mean absolute error (MAE) and the root mean square error (RMSE) between observed and simulated heads were used.

$$\mathrm{MAE} = \frac{\sum_{i=1}^{n} |\mathrm{Obs_i} - \mathrm{Sim_i}|}{n} \tag{3.11}$$

$$\mathrm{RMSE} = \sqrt{\frac{\sum_{i=1}^{n} (\mathrm{Obs_i} - \mathrm{Sim_i})^2}{n}} \tag{3.12}$$

For the transport part of the variable-density model, two checks were done to evaluate the numerical errors which occur in solving the advection and dispersion equations. The Peclet number is defined as:

$$\mathrm{Pe} = \frac{\Delta l}{\alpha_L} \leq 4, \tag{3.13}$$

where Δl is the cell size in the horizontal plane (m), and α_L the longitudinal dispersivity (m). This equation evaluates if the numerical dispersion exceeds the longitudinal dispersion of the transport. The threshold of Pe can be defined in multiple ways, in this work it was assumed that it should be smaller than 4 [85].

The Courant number was used to check if the time step was valid for the transport process regarding the used cell size, and is computed by:

$$\mathrm{Co} = \frac{v \Delta t}{\Delta l} \tag{3.14}$$

with v the velocity in $x-$, $y-$, or $z-$direction (m d^{-1}), t the time (d) and l the cell size in horizontal or vertical direction (m). For accurate results, the Courant number should not exceed 1, which means transport driven by advection should not exceed more than one grid cell during one time step [85]. The Courant number was calculated for each grid cell in the steady-state solution.

The heads and flow budgets were used in a MODPATH particle tracking simulation and a ZoneBudget simulation, which are two additional softwares of MODFLOW to post-process the results. The particle tracking was used

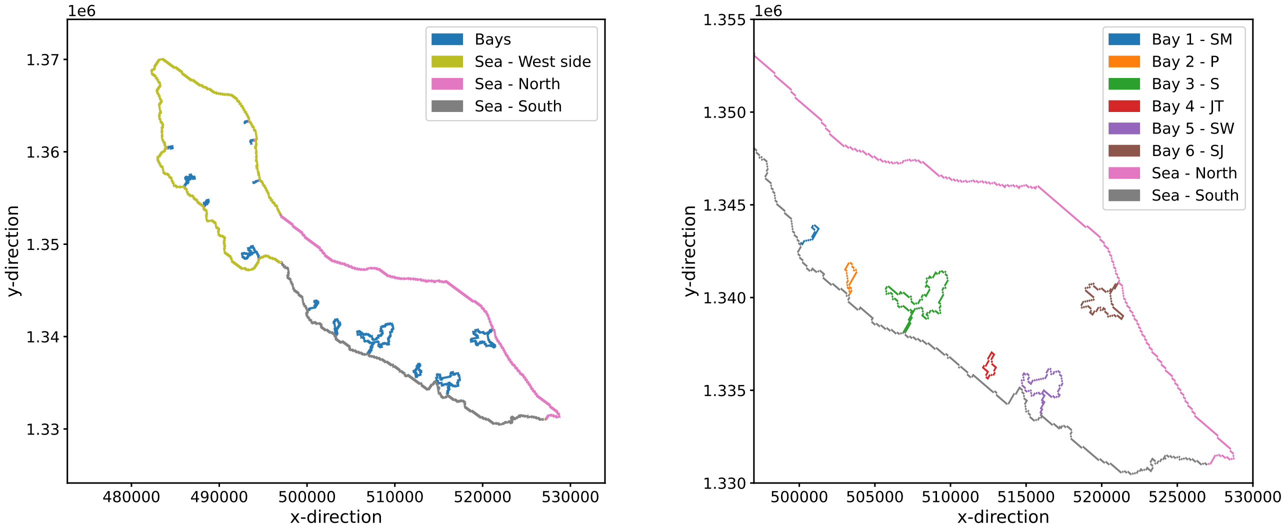

(a) Different zones used for the groundwater flow simulation.

(b) Different zones used for the nutrient simulations. Abbreviations for bays: SM = Sint Michiel, P = Piscadera, S = Schottegat, JT = Jan Thiel, SW = Spaanse Water, and SJ = Sint Joris.

Figure 3.4: Marking of zones for ZoneBudget simulation for both the groundwater flow model and the nutrient transport model.

to determine the capture zones by simulating backward tracking of particles released at the sea/bays boundary. With this result, the simulation period for the tracer simulations was determined. It assessed whether particles released across a large portion of the island would have travel times long enough to reach a boundary. In addition, since sorption was considered in the tracer simulations, the simulation period needed to be extended to account for this process.

ZoneBudget can be done for both a flow model and a solute transport model. The input for the model is the model grid and the water volume flows or solute mass flows of a cell. During the simulation, each water volume or mass component, like recharge, boundary flow or sorbed mass, is summed for the cells in a specified zone. ZoneBudget was used to determine the flow and flux towards the sea and the bays, providing insight into how much water and nutrients discharge into the sea and identifying which bays are vulnerable to pollution. Figure 3.4a shows the marking of these cells for the flow model, and Figure 3.4b for the nutrient simulations. The sea was divided into three zones for the flow model, and into two zones for the nutrient simulations. This was done to evaluate the two coastlines as separate. For the nutrient simulations, which only focused on the east side of the island, the different bays were considered as individual zones.

For the nutrient transport model, the initial concentration was set to 0 kg m^{-3}. The heads and flow budgets of the final time step from the variable-density model, which were assumed as the steady-state heads and flows, were used in the nutrient transport model, in this way, it was not needed to calculate the variable-density flow again and therefore it significantly reduced computational time. The output file containing the flows and heads was modified, retaining only the last time step and adjusting the time step to 1. Further details on this process can be found in Appendix G. The number of periods and the period length were dependent on the simulation. The time step was set to 0.5 years after the Courant number was assessed for the variable-density model. Lowering the time step reduces the cells which exceed the Courant number. The outputs of the nutrient transport model were concentrations and mass budget files. For this transport model, also a ZoneBudget simulation was done.

3.3. Simulations

In this section, the different types of simulations are described. First, the tracer simulations to obtain subgoal 1, which aims to determine the spatio-temporal behaviour of different tracers, are described. Second, the simulation to determine the current state of the pollution from leaking OSDS is described. And third, three future scenarios are described, investigating the effect of changes in population or pollution measures.

3.3.1. Tracer simulations

To determine the different behaviour of nutrients of Curaçao, three tracers with different characteristics were simulated. First, a conservative tracer was simulated, second a tracer with degradation and third a tracer with sorption. These three tracers represented respectively chloride (Cl^-), NO_3^- and PO_4^{3-}. In these simulations, a mass was inserted at different locations. It was chosen to focus on only the east side of the island due to the better flow model performance and the urban development on this side. These locations were determined by adding a raster, and at each corner of the raster cell, a mass with a rate of 1 kg d^{-1} was released within the active model domain. The locations are given in Figure 3.5.

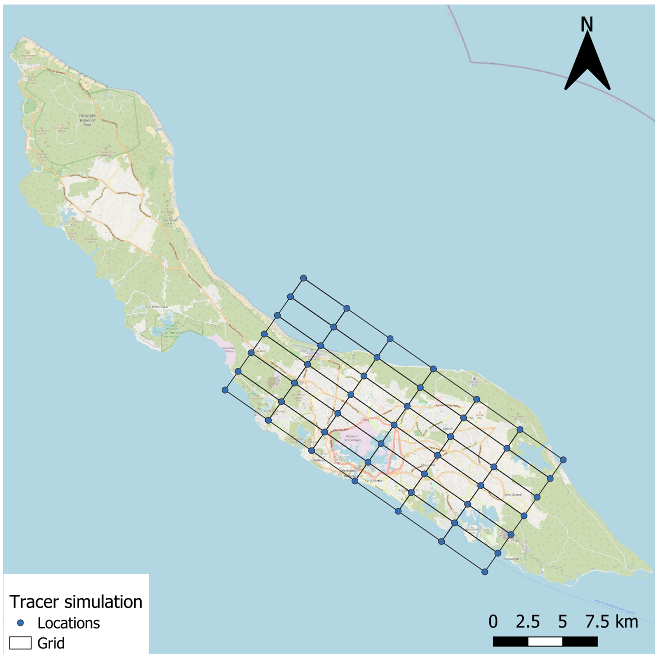

Figure 3.5: Locations of mass insertion for tracer simulations

The simulations were done for 250 years with time steps of 0.5 years. This 250-year period was chosen because, after 100 years, most particles would have reached the bays or the sea, and the time frame was extended to account for sorption effects. For each simulation, the concentration in a cell was multiplied by the saturated thickness and the average over the depth interval was determined. Also, a ZoneBudget analysis was performed to determine the mass fluxes into the different zones over time.

3.3.2. Current state simulation

To determine the current state of the nutrients N and P in the groundwater as a result of leaking OSDS, a simulation was done using the population and average N and P-input per day. Population data was available for the period 1900-2021, and therefore 2021 was taken as the current situation. For some years, data was missing, and the population in these years was determined by linear interpolation. The population has grown over the years (see Figure 3.6), resulting in increased N- and P-loadings. The outcomes are depending on the moment a mass is released, due to the time-dependency of decay and sorption, and therefore population growth over time is important.

The spatial distribution of the population was based on the current population density per neighbourhood, as shown in the map in Figure 3.7. The model assumes that the population density proportions across different zones remained constant throughout the simulation. However, in reality, the expansion of Willemstad has occurred over the years. It is expected that the population was concentrated in a smaller area of the island compared to the present.

To determine the leakage from OSDS, an estimation of the daily excretion of N and P per person was made. For N, a mass rate of 13.3 g d^{-1} (range 9.0 - 21.7 g d^{-1}) per person was assumed as loading, and for P 3.28 g d^{-1} per person was used [88]. Not all households on Curaçao depend on OSDS, 16% of the wastewater is treated. Therefore the mass input into the system was multiplied with a fraction of 0.84.

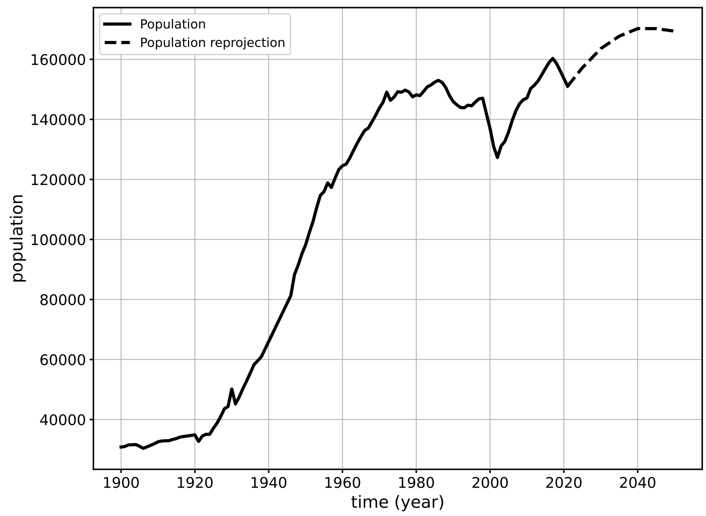

Figure 3.6: Population of Curaçao for the years 1900 - 2021 and a population projection based on a constant fertility projection [86, 87].

The amount of mass added to the model per cell can be expressed as:

$$L_{cell} = \frac{P_{\%}}{A} * P_{year} * \Delta r * \Delta c * f_{dcs} * L_p, \tag{3.15}$$

where L_{cell} is the loading of the nutrient per cell (kg d^{-1}), $P_{\%}$ a percentage of the total population for that neighbourhood (-), A is the area of the neighbourhood (m^2), P_{year} represents the population for a given year (-) [87], Δr and Δc are the distance between respectively the rows and columns of the model grid (m), f_{dcs} is the fraction of population which is not connected to a centralised sewer system (-) and L_{person} (kg d^{-1}) is the amount of the nutrient which one person excretes per day.

For N it was assumed that it all converted to NO_3^- when it entered the groundwater and for P it was assumed that it converted to PO_4^{3-}. In the literature, there are different approaches for simulating nitrate in groundwater. Karlović *et al.* [89] researched the transport of NO_3^- through groundwater in Croatia in which they assumed NO_3^- to be conservative. Contrary, NO_3^- is also often simulated using first-order decay [90–93]. For Curaçao, little is known about the denitrification process, and therefore the transport of N was modelled twice; with conservative behaviour and with decay.

In this work, it was assumed that the total amount of daily excretion fully leached to the groundwater, and no treatment occurred. Septic tanks do have a treatment function, This overestimates the amount of N and P.

For the conservative simulation of N, a removal in ODSD and during soil infiltration was considered, multiplying the mass input with 0.7 to account for a reduction of 30% [94]. For the decay simulation of N and P, it was assumed that the total amount of nutrients leached to the groundwater and that there was no treatment. Consequently, the vertical positioning of OSDS and the corresponding leakage were not considered. The model assumed that all nutrient mass reached the groundwater, while in reality, some might not and already decay or sorb before the groundwater table is reached. The effect of neglecting treatment was viewed as less critical, as the majority of OSDS are cesspits without having a treatment capability. Moreover, the regulations and maintenance are lacking and septic tanks will lose the treatment function [95]. If cesspits are replaced by septic tanks in the future, nutrient removal should be incorporated into the simulations.

The average concentration over a depth of 50 m of both N and P for the current situation (2021) was determined. 50 m was chosen because for some locations, the groundwater table is 30 m below the surface and if the average well depth of 20 m was chosen, valuable information would be lost. The nutrients did not reach the deeper layers below 50 m, and therefore this depth was neglected in averaging the concentrations. Furthermore, the mass fluxes of N and P into the bays and sea, and their ratio (N:P mass ratio) were determined.

To assess the accuracy of the model, the simulated current concentrations were compared to NO_3^- and PO_4^{3-} groundwater measurements done by PhD student Mike Wit on Curaçao. Because N and P were used as input, the concentrations were converted to respectively NO_3^- and PO_4^{3-} concentrations by considering their relative mass ratio. For this comparison, it was assumed that all N was converted to NO_3^-, and all P was converted to

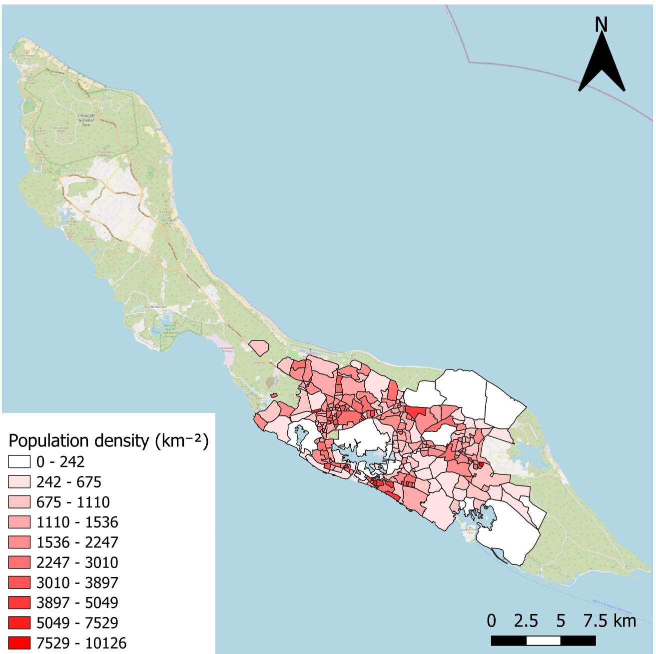

Figure 3.7: Population density in the different neighbourhoods per km^2 which were considered in the simulation.

PO_4^{3-}. This should be evaluated if this is correct for Curaçao. McCray *et al.* [96] state approximately 75% of N dissolves as NO_3^- and for P this range from 76% to 95% to be converted to PO_4^{3-}. For the conversion of N to NO_3^-,

$$\frac{\text{mass } NO_3^{-1}}{\text{mass N}} = \frac{62}{14.01} \approx 4.43, \tag{3.16}$$

was used, and for P to PO_4^{3-},

$$\frac{\text{mass } PO_4^{-1}}{\text{mass P}} = \frac{94.97}{30.97} \approx 3.07, \tag{3.17}$$

was used. The converted concentrations on the sample locations were averaged over the depth of the sample well, and compared to the measured concentration in the well.

3.3.3. Future scenarios

After the current state was simulated, the concentration in 2021 was used as input for the three future scenarios as the initial concentration. The three scenarios represented 1) population growth, 2) stopped pollution from OSDS, and 3) a no-change scenario to investigate the effect of changing inputs.

For the population growth, a population growth reprojection based on constant fertility was used [86]. The population calculated based on the reprojection is given in Figure 3.6 by the dashed line, the exact growth percentages per year can be found in Appendix H. In the stopped pollution scenario, the mass input was set to 0 kg d^{-1}. This reflects the situation if all OSDS are replaced by a centralized sewer system, and no leakage of N and P to the groundwater occurs. The no-change scenario used the known population of 2021 and nothing was changed to the model inputs. All three scenarios were simulated for the period 2021 to 2050, based on the available data of the population growth projections.

As for the current state situation, the average groundwater nutrient concentration at the end of the simulation period was obtained, and a ZoneBudget analysis was done to obtain the mass fluxes over time and to compute the N:P mass ratio over time.

4 Results

In this chapter, the results and implications of the different simulations are given. First, groundwater heads and flows across the island are described, followed by an assessment of the performance of the model. Next, the resulting flow field was used to simulate the spatio-temporal behaviour of tracers with different reaction characteristics. Lastly, a first model result of the current state of nutrient fluxes in the groundwater due to the leakage from OSDS and three potential future scenarios are given.

4.1. Groundwater flow

4.1.1. Behaviour groundwater

First, an estimate of the groundwater heads was made based on a constant-density model, the results can be found in Appendix I. The heads were the highest on the west and central part of the island. Regarding the flow, water was only flowing out towards the sea and bays, and the inflow was only due to the infiltration of rainfall. Using these groundwater heads as initial conditions for the transient variable-density model, the groundwater heads based on differences in density as a result of saltwater intrusion were calculated. In Appendix J, the evaluation of the heads and water outflow to bays and sea over time can be found. It can be observed that after 4500 years, the steady-state situation was approximately achieved. Using the variable-density groundwater model, the head distribution and corresponding flows of Curaçao were simulated. The surrounding sea and bays influenced groundwater levels, resulting in the integration of fresh and saltwater densities in the model. Although data on the spatial distribution of the geological layers in the vertical direction was limited, requiring a simplification of the 3D geological model, and the lack of hydrogeological data, a groundwater flow model was created successfully.

The map view in Figure 4.1 shows the groundwater heads simulated with the variable-density model. The heads simulated with this model were slightly higher compared to the freshwater-only model, especially at the west side of the island. The difference in heads between the two models is shown in Appendix I. The head distribution showed patterns as expected following the topography of Curaçao, areas with higher elevations also had higher heads. Also considering the different geological formations, the heads and flows showed an expected behaviour. Lower hydraulic conductivity resulted in a lower specific discharge and therefore water accumulated, resulting in higher groundwater heads. This can be observed on the west and central part of the island where MCF and Knip Group were modelled in the first 20 m from the surface. Contrarily, in areas with a higher hydraulic conductivity, the water flowed more easily. This was observable near the coast in the limestone formation, where the heads were lower due to the higher hydraulic conductivity resulting in less accumulation of water.

In the southeast of the island, the simulation showed elevated groundwater levels. This could be due to the simplification of the conceptual geological model. Limestone was modelled with a thickness of 20 m, whereas in reality, it exceeds this thickness due to the presence of the limestone mountain (Tafelberg). Below this limestone, an unweathered CLF layer with a low permeability was modelled. The hydraulic conductivity of the limestone is higher, and water will not accumulate as in the model. A more accurate 3D geological model would improve the outcomes.

The map in Figure 4.2 shows the average specific discharge over depth. The specific discharge was highest in the coastal area and around the bays. On the east side of the island, weathered CLF and limestone formations were found on the upper layers with both having a relatively high hydraulic conductivity. However, some of these areas had low average specific discharge, for example, on the northeast side of the island. This is due to the large distance between the surface and the groundwater level. Due to the water flowing deeper, it travelled through the deeper unweathered CLF or MCF layers, with a low hydraulic conductivity. This phenomenon can be observed in the cross-section in Figure 4.3, the distance to the groundwater table was larger in the higher elevated areas.

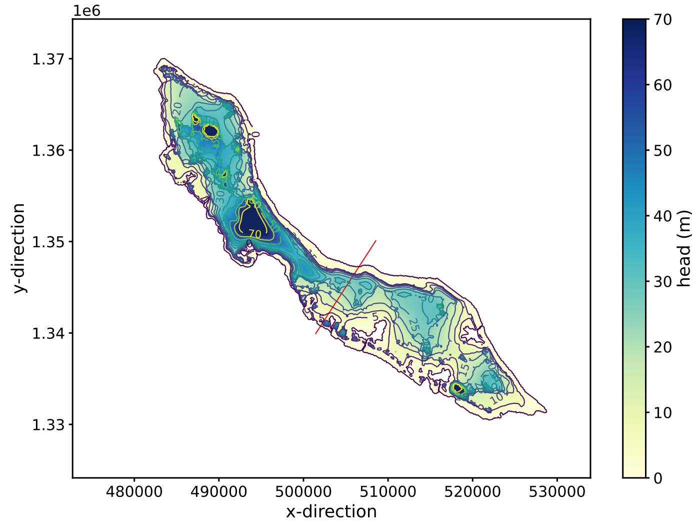

Figure 4.1: Simulated groundwater heads on Curaçao, the contour lines show different levels of the groundwater heads. The red line indicates the location of the cross-section.

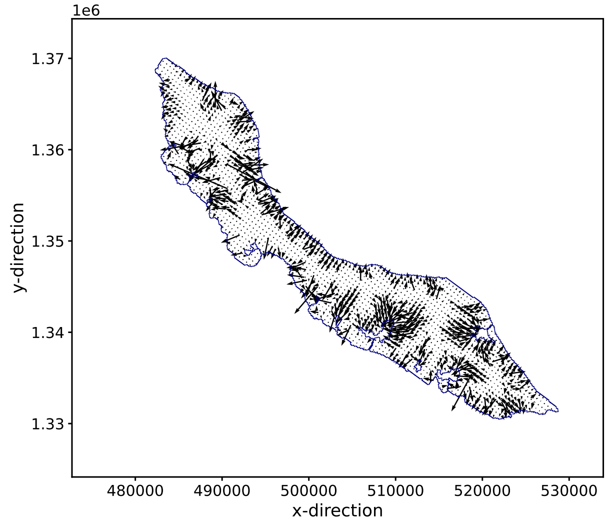

Figure 4.2: Specific discharge averaged over depth, showing the resulting flow field. Vectors indicate flow direction, with their length representing the magnitude of the specific discharge.

The initial salt concentration in the aquifer was 35 kg m^{-3}, it can be observed that these concentrations have been decreased as a result of the flushing of salt by the recharge. Looking at the flow directions in the cross-section in Figure 4.3, it can be observed that the salt concentration in the groundwater affects the groundwater near the bays and sea coastline. Groundwater also flows into the aquifer from the sea and bays, contrary to the simulated flows with the freshwater-only model.

On a daily basis in the final steady-state situation, the total water outflow (SGD) from the aquifer into the bays and sea was 58,720 m^3 d^{-1}, with 47% flowing into the bays and 53% into the sea. Because the steady-state situation was simulated, the total inflow should equal the total amount of outflow. The amount of recharge to the groundwater based on infiltration from rainfall was equal to 56,750 m^3 d^{-1}, which is 97% of the total water outflow. The remaining 3% consisted of water inflow from the bays and sea, which was subsequently recirculated back into the bay or sea. The sea coastline has a length of 134.5 km, while the bay coastlines have a total length of 56.1 km, resulting in SGD of 231 m^3 d^{-1} km^{-1} and 494 m^3 d^{-1} km^{-1} respectively. Although the sea coastline is longer, a similar quantity of water flows towards the bays and the sea. This could also be related to the higher specific discharge near the bays compared to the specific discharge near the sea coastline, observable in the map in Figure 4.2.

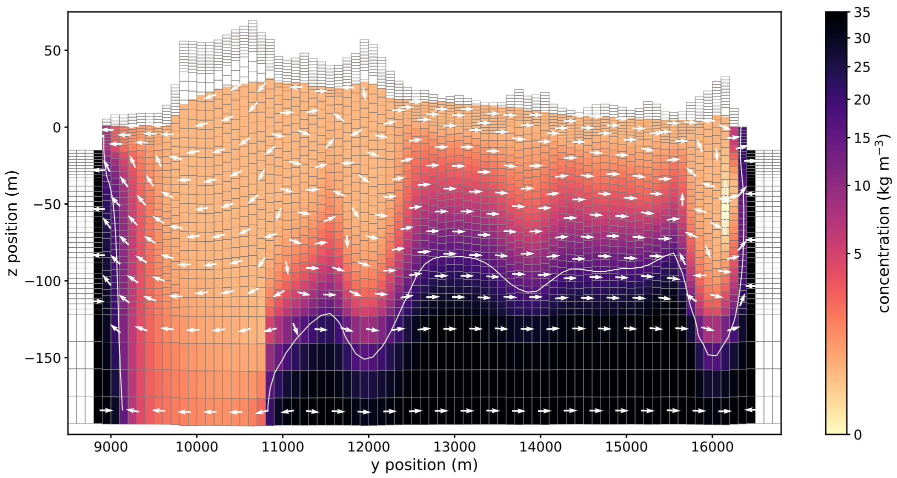

Figure 4.3: Cross-section showing the salt concentration simulated with the variable-density model, using a colour scale. The vectors indicate flow direction, and the concentration is displayed up to the groundwater table. The white line marks the fresh-saline groundwater interface, defined by a salt concentration of 17 kg m^{-3}.

The sea and bays were modelled using a constant head boundary across all layers. While the use of constant head boundaries is often used in previous studies [50, 80], it may lead to an overestimation of discharge, as unlimited water can be discharged to maintain the specified constant head. In reality, the seabed could provide resistance, limiting the outflow and resulting in lower SGD. Therefore, it is recommended to assess the effect of the boundary definition and future research should evaluate the effect of including the seabed and the bay bed.

The flow paths resulting from a backward particle tracking simulation of 100 years are shown in the map in Figure 4.4. The flow paths ending at the bays were reaching further inland than those ending at the sea boundary, so it took longer for particles to reach the sea boundary. Based on this particle-tracking simulation, a simulation period of 100 years seemed reasonable for a conservative tracer. When considering sorption, the flow of the tracer is retarded, with the degree of retardation depending on the geological type and its associated bulk density. The retardation factors ranged from 17.1 to 401.4, reflecting the delay in solute transport velocity relative to water. Consequently, the tracer simulations were conducted over a 250-year period to account for this effect.

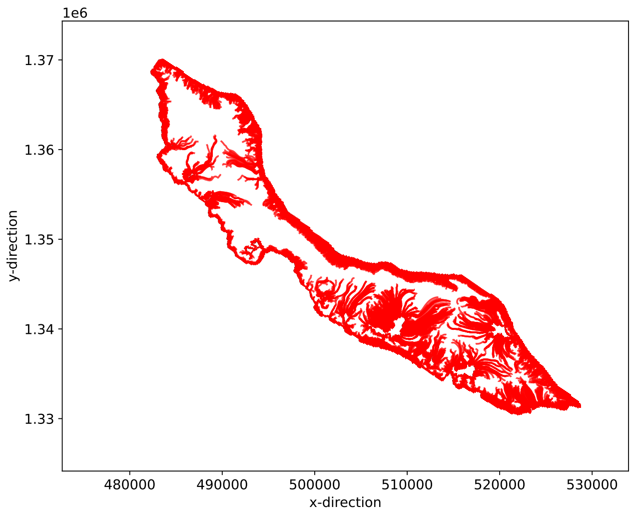

Figure 4.4: Backward tracing simulation of particles released at the coastline. The lines represent the travelled distance in 100 years.

4.1.2. Validation and numerical stability

The numerical stability of the variable-density model was assessed with the Courant and Peclet numbers. The Courant number was evaluated in the $x-$, $y-$ and $z-$direction. Cells exceeding the threshold of 1 were defined as unstable. In the map shown in Figure 4.5, the number of cells exceeding this threshold in the z-direction is displayed. 5.9% of the total cells in the active model domain were marked as unstable for the variable-density model. The Peclet number of the full model was equal to 4, which was within the defined restriction.

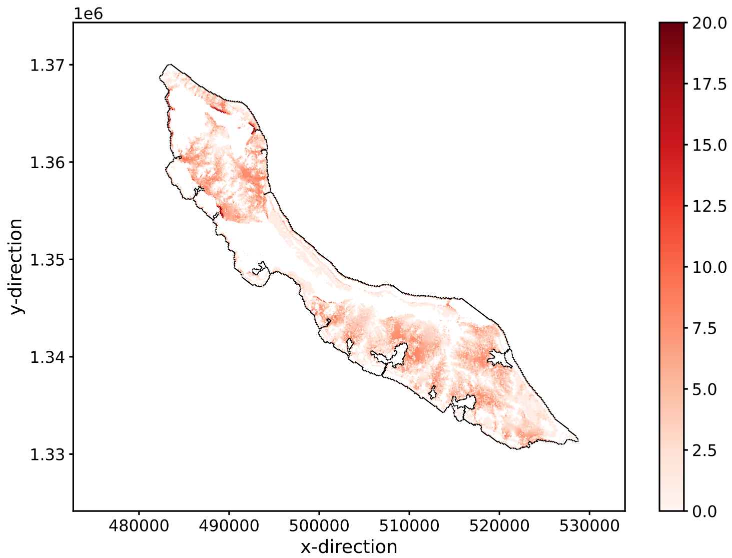

Figure 4.5: Cells which exceed the Courant threshold of 1 are indicated, and the colour scale indicates the number of cells in the z-direction which exceeded the threshold.

The simulated groundwater heads were compared to the observed groundwater heads in 129 different locations, given in Figure 4.6. The RMSE between observed and simulated heads was 15.29 m and the MAE was 9.48 m (Figure 4.6a). The heads were both under and overestimated, with the largest errors in the west-central part of the island in the geological formation MCF (Figure 4.6b). Within a distance of 1500 m, a head difference of 50 m was observed, while the model showed a more gradual change in heads. Due to this, the RMSE was large in this area. In general, the groundwater heads were overestimated on the west side of the island, this was due to the complex geological formations present. In the model, MCF and Knip Group had a constant hydraulic conductivity, and lowering this value would result in underestimating the groundwater heads in other locations. The best way to improve this would be to add a hydraulic conductivity which differs spatially.

In the evaluation, there was a distinction made between locations on the west side and the east side of the island, indicated in the graph in Figure 4.6 with respectively diamonds and circles. As can be observed, the model performed better on the east side. When only evaluating the model performance for this side, the RMSE between observed and simulated heads decreased to 6.12 m. The simulated heads were modelled for the annual average situation, while the observations were done at different moments in time and are momentary observations and therefore not represent the steady-state heads. The groundwater levels per location have an average difference of 0.88 m. Therefore, some difference was expected between the fluctuating observed heads and steady-state simulated heads. Considering this, and the lack of data for model creation and validation, the RMSE was assumed reasonable

The evaluation of the variable-density flow model validity and stability was used to make choices for the nutrient transport model to increase its performance. Due to the better model performance on the east side of the island, in combination with the relevance of pollution in the urban area on the east side, it was chosen to focus on that side for the nutrient transport simulations. In addition, an adjustment was made to increase the numerical stability of the model. The Courant number depends on the time step and the dimensions of the cells in the model grid (Equation (3.14)). For the nutrient transport model, it was possible to simulate with a different time step, while the grid cell size had to be the same as the variable-density model. To increase the numerical stability of the model for these simulations, it was chosen to adjust the time step in the tracer simulations to 0.5 years instead of 1 year, reducing the percentage of unstable cells to 2.9%. Although a smaller time step would improve the stability, the run time of the model would increase and therefore 0.5 years was used. In future research, the time step could be decreased to assess the effect on the results.

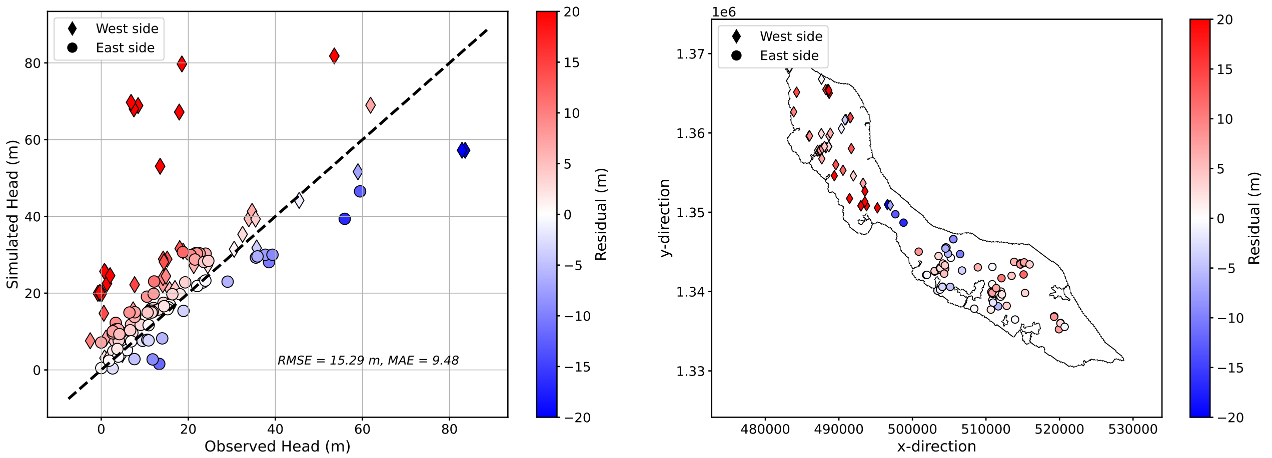

(a) Simulated versus observed heads, resulting in a Root Mean Square Error of 15.29 m and a Mean Absolute Error of 9.48 m.

(b) Map with residuals between simulated and observed heads.

Figure 4.6: Comparison of observed and simulated heads to assess the model performance. The diamonds indicate the west side, and the dots the east side. The colour scale indicates the difference between simulated and observed.

4.2. Tracer simulations

The spatio-temporal behaviour of different tracers was simulated by releasing a mass of 1 kg per day at each of the locations described in Section 3.3.1. Of the 49 locations in the grid, 32 were located in the active model domain. Three simulations were done, one with a conservative tracer (Cl), one with a tracer with decay (NO_3^-) and one with a tracer with sorption (PO_4^{3-}). First, a spatial analysis of the conservative tracer is given. Second, the numerical analysis of the nutrient fluxes of all three tracers is given.

4.2.1. Spatial analysis

To get a conceptual idea of the behaviour of a tracer in the groundwater of Curaçao, a spatial analysis was done. The average concentration over the depth after 250 years for the conservative tracer is given in the map in Figure 4.7 together with the averaged transport flow velocity and directions. These vectors differ from the specific discharge (q) in Figure 4.2 because now the flow velocities (v) are shown which are dependent on the effective porosity of the geological layers. The concentration maps of the tracers with decay and sorption can be found in Appendix K. In Figure 4.8 the locations were grouped based on their drainage area and in Figure 4.9 the population density per neighbourhood is overlaid with these drainage areas. These drainage areas were manually determined based on the flow directions towards a bay or sea boundary.

It can be observed that in the central part, the tracers were flowing towards Schottegat Bay (bay 3). This was expected based on the flow field with most flow vectors directed towards this bay. The drainage area of this bay is large and therefore a large fraction of tracers will flow towards this bay. When looking at the population density, this area also comprised densely populated areas. Based on this, Schottegat Bay was indicated as vulnerable to pollution originating from OSDS. Contrarily, the large drainage area of Spaanse Water Bay (bay 5) and Sint Joris Bay (bay 6), consisted of fewer populated areas and was therefore less vulnerable.

Along the north coast, especially for three tracer locations, the plume was less spread compared to other locations. Here, the surface was elevated and the water level did not rise into the limestone formation, because this was only modelled for the first 20 m from the surface. The groundwater level reached only in MCF, which has a low hydraulic conductivity, and therefore the tracers flowed through the SGD with a low flow velocity. The weathered CLF and limestone formations have a higher hydraulic conductivity, and therefore if the groundwater level reached these formations, the groundwater could flow more easily. For the weathered CLF, depth is a critical factor, because the degree of weathering decreases with depth, leading to higher hydraulic conductivity in the shallower regions closer to the surface.

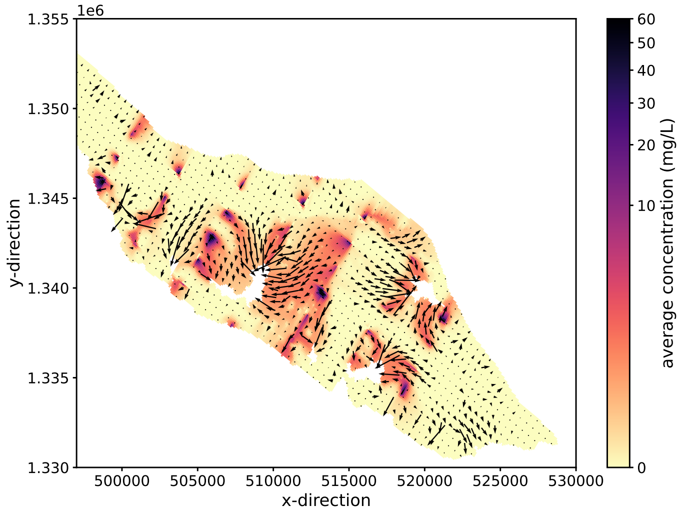

Figure 4.7: Averaged concentration over depth after 250 years for the conservative tracer (Cl^-) with the vectors indicating the average flow velocity. For the colour scale, a power-law normalisation is used with gamma = 0.3.

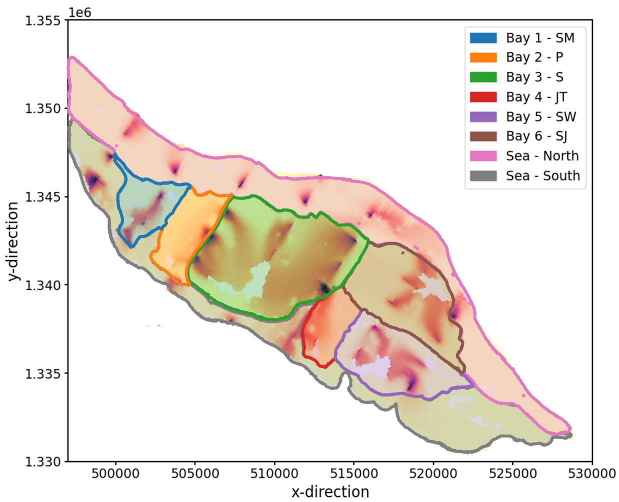

Figure 4.8: Drainage areas of the different bays and sea highlighted. Abbreviations for bays: SM = Sint Michiel, P = Piscadera, S = Schottegat, JT = Jan Thiel, SW = Spaanse Water, and SJ = Sint Joris.

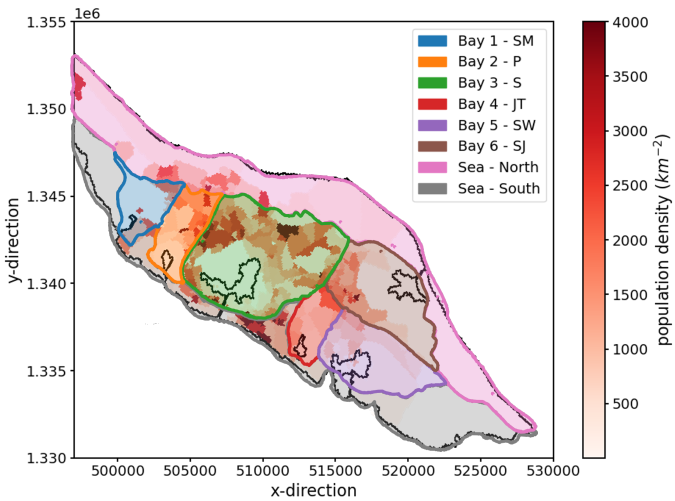

Figure 4.9: Population density per neighbourhood, and drainage areas as overlay. Abbreviations for bays: SM = Sint Michiel, P = Piscadera, S = Schottegat, JT = Jan Thiel, SW = Spaanse Water, and SJ = Sint Joris.

4.2.2. Nutrient fluxes

Next to the evaluation of the concentration, a ZoneBudget simulation was executed to determine the nutrient fluxes towards the bays and sea. In Figure 4.10, the mass fluxes into the drainage areas as a percentage of the total mass flux into the aquifer per day over time, are given. It can be seen that the reaction characteristics of the tracer influence the behaviour of the nutrient flux through the subsurface, and therefore the order of most capturing zones changes.

For the conservative tracer, the flux out of the system increased the most during the first 100 years. After 250 years, the mass flux is near a steady state for almost all drainage areas. Except for Schottegat Bay (bay 3) and the northern sea coast, here fluxes were still increasing at the end of the simulation. Schottegat Bay was capturing most of the mass, this is due to the drainage area and therefore the longer distances for the nutrients to travel. 82.3% of the mass inflow per day was flowing out after 250 years (Table 4.1). The outflow to all bays and the sea did not add up to 100% because not all of the fluxes were at a steady state at the end of the simulation.

Similarly, for the tracers with decay, the steady-state situation was already reached, although this happened for all fluxes within 20 years. The simulation shows a different pattern compared to the conservative tracer, the order of most capturing zones was changed, with Sint Joris bay (bay 6) receiving the largest mass flux of tracers susceptible to decay. Only a small amount of the tracers added to the system reached the bays or sea, and most of the tracers decayed over time in the groundwater, as only 15.8% reached the boundary in the steady-state situation (Table 4.1). For this tracer, the travel distance was important, and therefore how far the pollution source was located from a bay or sea coast. Together with the flow velocity, the flux depended on this. For example, Jan Thiel Bay (bay 4) did not receive much mass due to the lower flow velocity and the greater distance from the tracer locations to the bay. The mass flowing out to Jan Thiel Bay in the conservative case, was degraded before it reached the bay in the decay simulation. The half-life time of the tracer was set to 3 years, enabling only the tracers which flowed fast to reach either the bays or the sea. The slower tracers were degraded before they could reach the bays or sea coastline.

The tracer with sorption did not reach a steady-state outflow after 250 years, contrarily to the other tracers. Due to the retardation factors of the different geological formations, ranging from 17 to 401, it takes much longer for the tracers to reach the bays and sea. This is further evidenced by the observation that, when summed, 15.8% of the nutrient was discharged, in contrast to 82.3% for the conservative tracer. The flux towards the sea was relatively higher compared to the other tracers, especially during the first half of the simulation period. This is partly related to the tracer locations, as some of the locations were very close to the sea coastline. Regarding the outflux into the northern part of the sea, this outflow is seen to quickly increase after simulation initialisation, due to one of the tracer locations near the sea. For the south sea coast, limestone was located near the coast with the retardation factor of 30, which was lower compared to the retardation factor of CLF (76 for the weathered part, 401 for the unweathered part). The relatively low retardation factor resulted in less sorption near the sea compared to locations in the central part of the island comprised of CLF formation.

While Schottegat Bay received most of the mass for the conservative tracer, this could not be observed for the decay and sorption tracer. Due to the large drainage area of the bay, the large travelled tracer distance allowed more sorption and decay.

Table 4.1: Outflow of the tracer simulations after 250 years as a percentage of total mass inflow per tracer summed for the bays and both sea coasts for the east side of the island.

	Conservative	**Decay**	**Sorption**
Total bays	62.6%	11.5 %	10.2%
Total sea	19.7%	4.3%	5.6%
Total	82.3%	15.8%	15.8%

A notable result is the discrepancy between the distribution of mass fluxes and water volume flowing to the bays and sea. The volume outflow of water was equally distributed over the bays and the sea (47% and 53% resp.). Also when only considering the eastern part of the island, a similar distribution was observed (51% and 49%). Conversely, when analysing nutrient flow for the three tracers on the east part of the island, the mass flow was much more focused on the bays (see Table 4.1). This is partly due to the effective porosity which affected the flow velocity. While the limestone formation located near the sea coastline has a high hydraulic conductivity, it also has a high effective porosity, causing a lower flow velocity compared to the weathered CLF formation located near the bays. In addition, the difference was attributed to the location of tracer releases; no mass was released in the most eastern part of the island, even though water flowed into the sea.

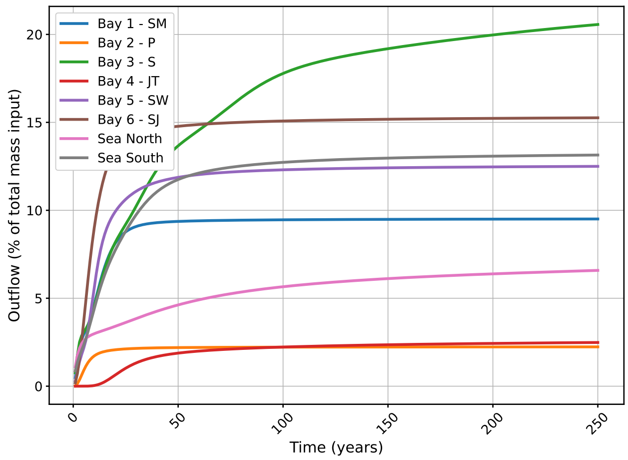

(a) Conservative tracer (Cl^-).

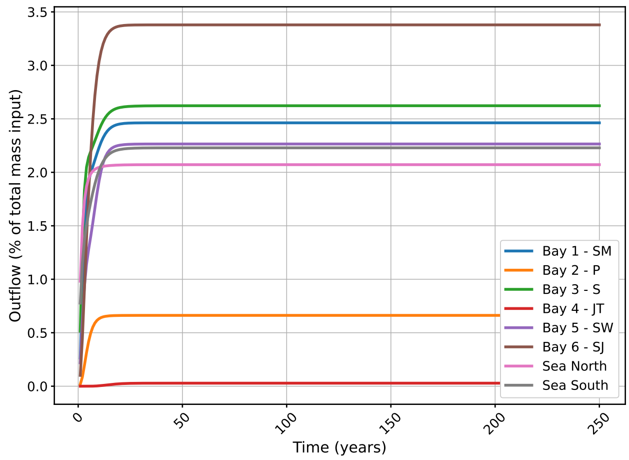

(b) Tracer with decay (NO_3^-).

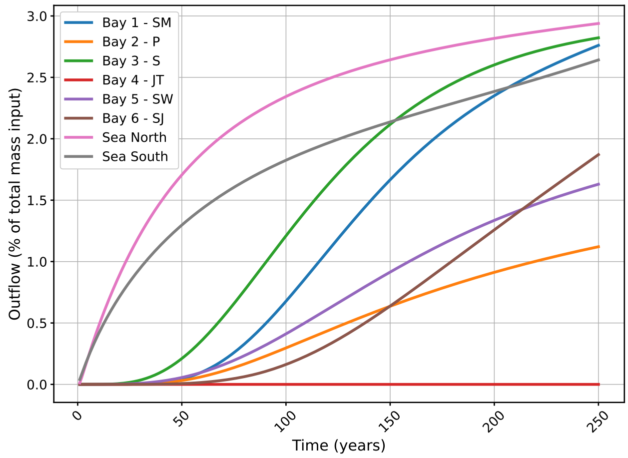

(c) Tracer with sorption (PO_4^{3-}).

Figure 4.10: Mass flowing into bays/coast per day as a percentage of the total mass inflow into the mainland. Abbreviations for bays: SM = Sint Michiel, P = Piscadera, S = Schottegat, JT = Jan Thiel, SW = Spaanse Water, and SJ = Sint Joris.

4.3. Scenario simulations

First, the current state of the nutrient fluxes from OSDS leakage towards the sea and bays in Curaçao was simulated. Second, three scenarios were done to evaluate the impact of potential scenarios such as stopped pollution or increased urban development on future pollutant concentrations. These simulations are a first model result and should be treated carefully. The results are obtained with a simplified model, and further refining of the model and critical assessment of the model parameters and their uncertainty is therefore required.

4.3.1. Current state scenario

The simulation of N and P-leakage from OSDS started in 1900 and was simulated until 2021, which was assumed as the current situation. For these 122 years, the leakage as a function of the population was simulated. The average concentrations for the current test cases, including N as conservative, N with decay, and P with sorptive characteristics, are shown in Figure 4.11, Figure 4.12 and Figure 4.13 respectively. The average concentration for conservative N was the highest, followed by N with decay and then P. The ratio of the total mass of conservative nitrogen to decaying nitrogen to phosphorus in the groundwater is approximately 55:11:1.

This is partly due to the higher daily mass input in the conservative and decay simulations of N compared to P, with a ratio of 2.8:4:1. However, decay and sorption significantly reduced the groundwater concentrations. A more progressed spread for N compared to P was observable, which is in line with the effect seen for the tracers. The conservative and decaying tracer, illustrative for N-behaviour, spread more quickly, whereas the sorbed tracer, illustrative for P-behaviour, spread slowly due to the retardation caused by sorption. In addition, the sorption of P by the aquifer material occurred already near the source while the effect of the decay of N was observable further from the source. This is because the half-life time of N was 3 years and therefore it was not directly observable the

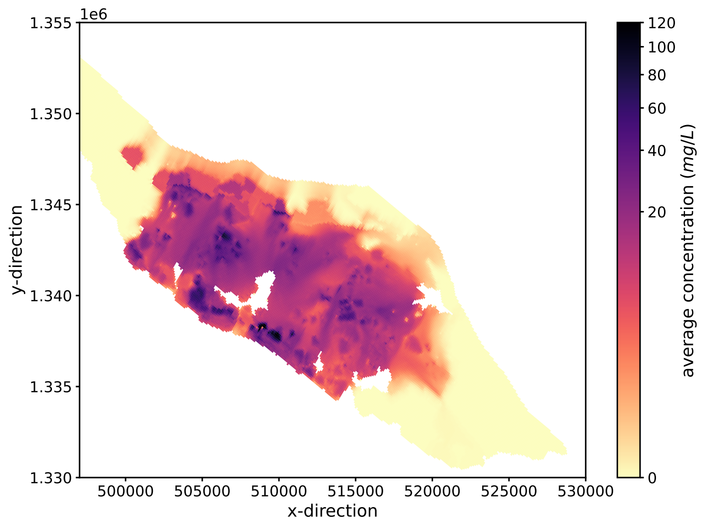

Figure 4.11: Average concentration of N for the current state, modelled as conservative transport. The concentration is averaged over the first 50 m below the surface. For the colour scale, a power-law normalisation is used with gamma = 0.3.

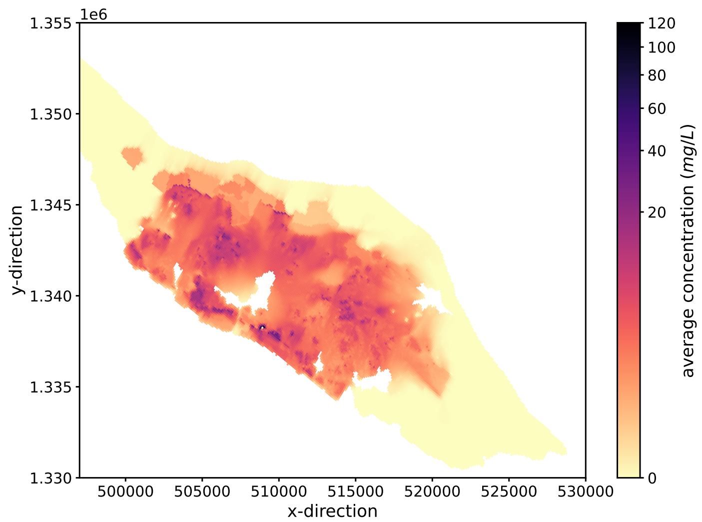

Figure 4.12: Average concentration of N for the current state, modelled with decay. The concentration is averaged over the first 50 m below the surface. For the colour scale, a power-law normalisation is used with gamma = 0.3.

moment the nutrient reached the groundwater. Consequently, the concentration of N was relatively higher near the source compared to the concentration of P. In addition, with sorption, relatively more P-mass was removed from the groundwater, compared to the decay of N.

The simulated concentrations were compared to groundwater measurements of NO_3^- and PO_4^{3-}. It was assumed that N and P were fully converted to respectively NO_3^- and PO_4^{3-}. For the comparison, the well depth at the measurement location was used to compute the average simulated concentration. The simulation of N with decay showed simulated concentrations in the same order of magnitude as the measurements, whereas the simulation with N as a conservative nutrient and P overestimated the concentrations compared to the measured values (Figure 4.14 and Figure 4.15). The median values of the simulations of conservative NO_3^-, decaying NO_3^- and PO_4^{3-} were respectively 211, 46, and 1.5 mg L^{-1}, while the median observed concentrations were were 47 mg L^{-1} for NO_3^- and 0.13 mg L^{-1} for PO_4^{3-}.

The results show an improved estimation of the N-concentrations for the test case that modelled N with decay, aligning more closely with the measured concentrations. However, despite being in the same order of magnitude, discrepancies between the measured and modelled N-concentrations can still be observed for the decay test case when the N-concentrations are evaluated on specific locations (Figure 4.16b). The model both overes-

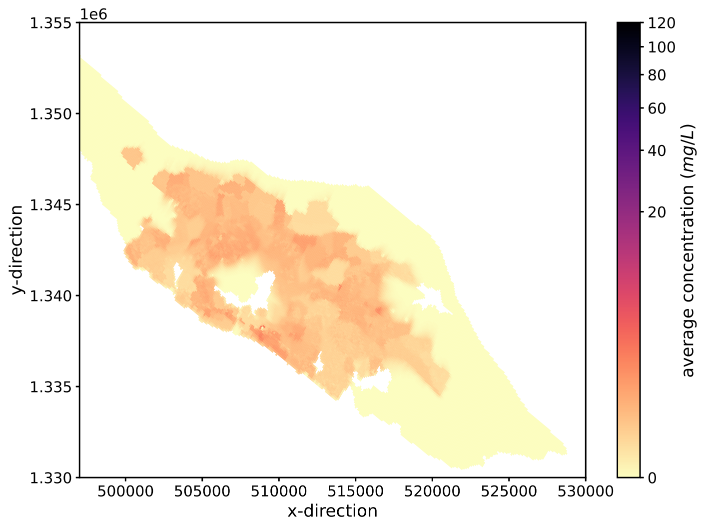

Figure 4.13: Average concentration of P for the current state. The concentration is averaged over the first 50 m below the surface. For the colour scale, a power-law normalisation is used with gamma = 0.3.

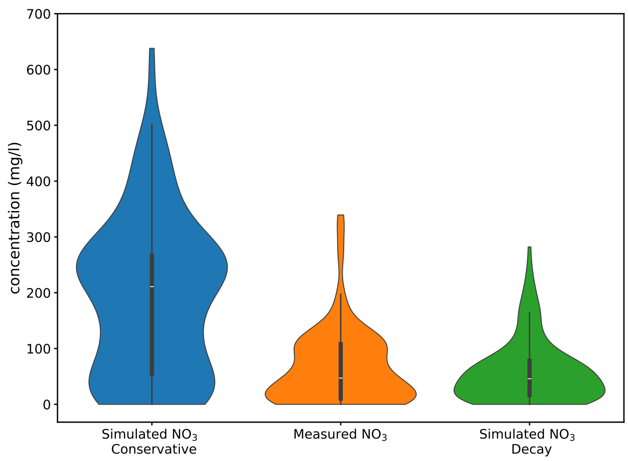

Figure 4.14: Violin plot of measured NO_3^- and simulated NO_3^- concentrations, both with conservative transport and with decay for the current situation on the east side of the island

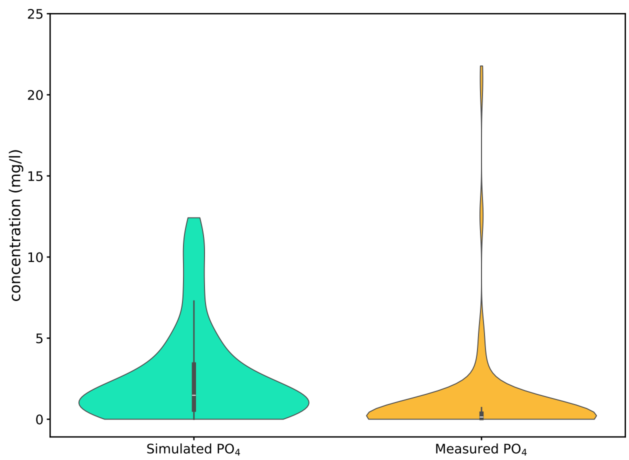

Figure 4.15: Violin plot of measured and simulated PO_4^{3-} concentrations for the current situation on the east side of the island.

timated and underestimated the concentrations, which resulted in approximately the same range of values. As can be seen for the conservative simulation of N and the simulation of P, the model significantly overestimated the concentrations (Figure 4.16a and Figure 4.16c).

An overestimated mass input can explain an overestimation of groundwater nutrients, as a lower daily nutrient loading would result in lower concentrations. Overestimation of input could be due to overestimated N and P-excretion by humans, insufficient modelled removal in the OSDS, and the assumption that all leaked N and P reach the groundwater. In literature, different fractions of N and P in wastewater are reported to reach the groundwater. While Valiela *et al.* [97] reported a 40% N-removal in septic tanks and Harris [94] indicated 10%, Lowe *et al.* [95] reported little to no N-removal. Moreover, these studies focus on septic tanks, whereas on Curaçao, most OSDS are cesspits, which have minimal removal capacity. Additionally, poor maintenance further decreases their effectiveness. Also, N and P-removal could occur during soil infiltration, ranging from 5 to 40% and 85% to 95% for N and P, respectively [94, 98]. The soil infiltration depends on the distance between the OSDS and the groundwater level, so it is recommended to research this distance and reduce the mass input if required.

Besides this, the concentrations in the test case of the conservative N could be overestimated due to the conservative reaction characteristics. If decay occurs, the concentrations decrease due to the degradation of N. Regarding P, the overestimation could also be due to too little sorption. If more sorption occurs, the concentra-

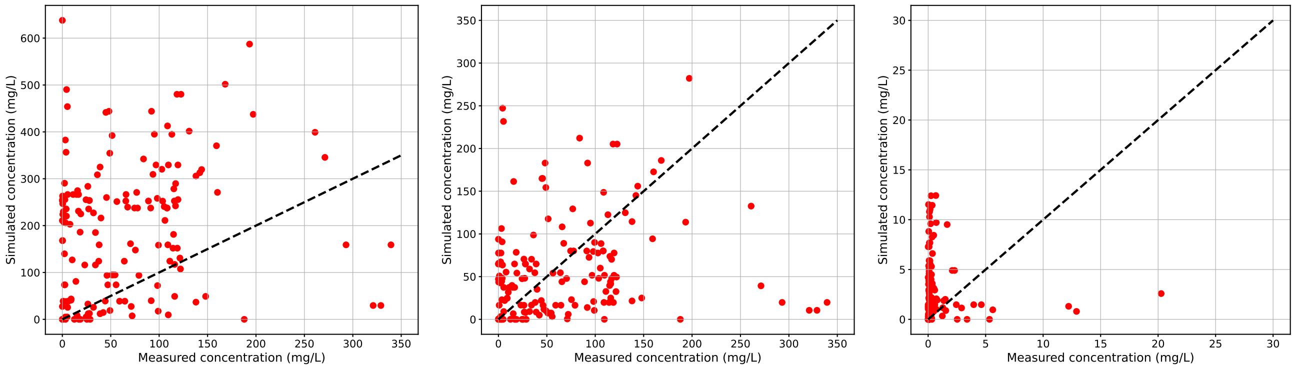

(a) NO_3^- as conservative. **(b)** NO_3^- with decay. **(c)** PO_4^{3-}

Figure 4.16: Simulated concentration averaged over the well depth for the three test cases of the current scenario compared to groundwater measurements of NO_3^- and PO_4^{3-} measured on that location.

tions will decrease and become closer to the measurements.

Due to these uncertainties, it is recommended to first conduct a critical assessment of the input values before refining the reaction characteristics. A sensitivity analysis should then be performed to improve and assess the accuracy of N and P-fluxes on Curaçao, including the evaluation of reaction parameters, such as decay and sorption constants.

For the current situation, also the mass fluxes towards the bays and sea coastlines were evaluated. The mass of N and P flowing into a bay or sea per day is given in the graphs in Figure 4.17. Because the size of the different bays and the sea differ, the mass flux was also calculated per kilometre coastline. This is given in Appendix M.

It can again be observed that different reaction characteristics affect the mass fluxes over time. For both test cases of N, the mass flux trends closely followed that of the population growth. At the steep rise of population density starting in 1925, an increase in N-outflow followed quickly. With the stagnation of population growth in 1970, the conservative N-tracer continued to increase for a few decades, where the decaying N-tracer outflow plateaued almost instantly. This is due to the longer travel time from the input location to the outflow zone. For the conservative tracer, the increased input with a long travel time to the bays and coast was still on its way when population growth stopped in 1970, causing a further increase of outflow. For the decaying N-tracer, the input with longer travel times will never reach an outflow area due to the decay characteristics, resulting in a faster response after a stop in population growth.

In contrast to N, the population growth trend was less observable in the mass flux of P. The increase in outflow due to the significant population growth that began in 1925 was delayed, with a more pronounced rise observed from 1940. The stagnation of the population increase was not observable in the mass fluxes, as the mass flux kept increasing. This is related to the sorption of P, which delayed the outflow of the nutrient relative to the water flow. Most of the drainage zones consist of weathered and unweathered CLF, with a retardation of 76 and 401 respectively. As a result, most fluxes passed through from the upper layers, since the retardation factor of 401 prevented outflow unless P was inserted near a bay. The outflow along the southern coast was highest for P due to the lower retardation factor of limestone (30) compared to CLF. As some of the fluxes here occurred within the first 20 m from the surface, P travelled through the limestone. None of the P-fluxes reached a steady state, and the outflow continued to increase until 2021.

Similar to the tracer simulations, a higher mass flux towards the bays compared to the sea was observed (see Table 4.2). This is partly due to the previously discussed different effective porosity values for the geological formations around the bay and coastal area, and partly due to the highly populated areas around the bays. For P, the flow towards the bays is relatively smaller compared to N. Furthermore, it can be observed that mass flux was highest for the conservative simulation of N, as N-input was larger than P-input and the absence of sorption and decay effects increased the nutrient quantity that reaches the outflow zones.

For both simulation cases of N, the proportion of outflow to the different bays and the sea was similar, however the absolute values differ by a factor of approximately 5. The highest outflow is towards Schottegat Bay (bay 3), followed by the southern coast, which has an outflow 2.5 times lower. For P, the outflows into Schottegat Bay and the southern sea coastline are roughly equal. When analysing the outflow per kilometre coastline of the

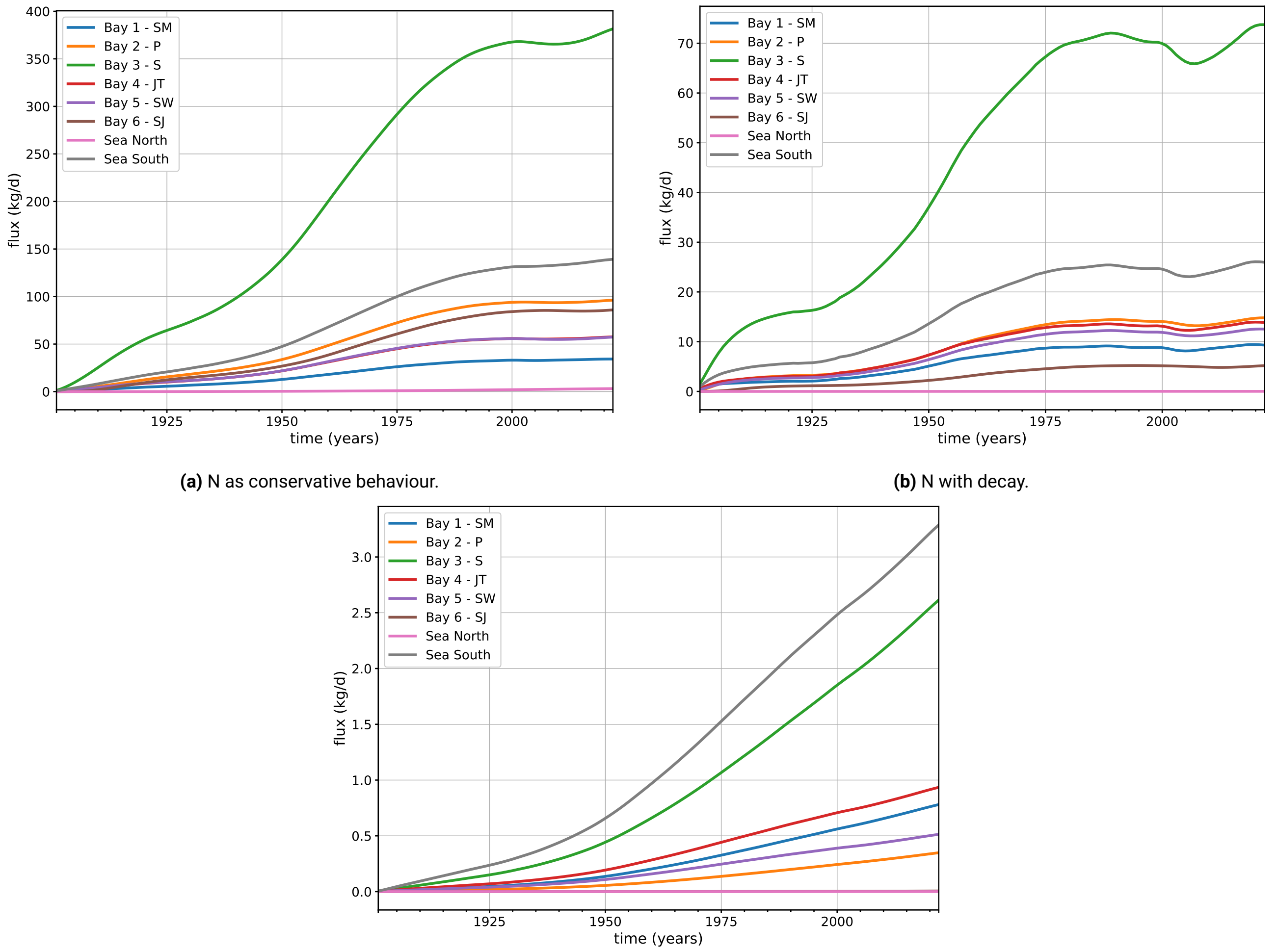

(a) N as conservative behaviour.

(b) N with decay.

(c) P with sorption.

Figure 4.17: Mass flowing into bays/sea coast per day during 1900 till 2021. Abbreviations for bays: SM = Sint Michiel, P = Piscadera, S = Schottegat, JT = Jan Thiel, SW = Spaanse Water, and SJ = Sint Joris.

bays and sea, Schottegat Bay remained significant for N, while for P the highest outflows were into Sint Michiel Bay (bay 1) and Jan Thiel Bay (bay 4). For both N and P, the significance of the mass flux towards the southern coast decreased, as it was one of the lowest when adjusted for coastline length. Little to no outflow to the northern coastline was observed for both N and P. This is due to the location of the populated areas, which are situated in elevated areas, resulting in a large distance between surface and groundwater levels. Consequently, flow occurred through the deeper MCF layers, which have a very low flow velocity.

These concentration results are a first test result and a critical assessment of the model parameters and their uncertainty is required. As can be seen in the test cases of N, the decaying behaviour specifically has a large impact on the concentration and mass fluxes and should be investigated further. The same goes for the sorption characteristics of P, and the porosity parameters of the modelled sediment.

Table 4.2: Total mass rate into bays and sea for the current situation and their relative distribution.

	Bays		**Sea**	
	Mass rate (kg d^{-1})	*Proportion (%)*	*Mass rate (kg d-1)*	*Proportion (%)*
N - Conservative	712.9	83	142.4	17
N - Decay	129.4	83	26.0	17
P - Sorption	5.2	61	3.3	39

Since the historical expansion of Willemstad was not considered and the current population distribution was applied, the mass outfluxes between 1900 and 2021 could differ. In reality, the mass was concentrated over a smaller area, whereas in the model it was distributed more widely. This leads to a broader spread of peak fluxes, as the same mass input was added to a smaller area in reality, resulting in locally higher concentrations and fluxes. This effect is more pronounced for P in the current situation, as P reacts more slowly due to retardation. For example, if Willemstad had been concentrated around Schottegat Bay, the mass input would have been closer to the bay, leading to a higher expected outflow for the present situation compared to scenarios where areas farther from the bay are included.

4.3.2. Future scenarios

Three different scenarios were simulated to assess the effect of population growth and stopped pollution. The fluxes into the bays and sea are shown in the graph in Figure 4.18 from 2021 onwards. The concentration maps of N, both as conservative and with decay, and P for the three future scenarios at the end of the simulations are given in Appendix N.

Regarding the N-fluxes, a direct effect was observable when changing the inputs in the future scenarios. The population growth increased the mass flux directly, while when the pollution stopped, the mass flux directly decreased. In 2050 the flux into the bays was increased by 12%. This quick reaction is because part of the N-flux reached the bays and sea boundary quickly after it was inserted, and therefore changes in inputs showed a direct effect in the outflux. In the no-change scenario for N with decay, the flux remained the same, while for the conservative case, a small increase was observed and the outflux reached a new steady state in 2050. Therefore both future scenarios affected the outflow of N within 30 years, as they differ from the no-change scenario.

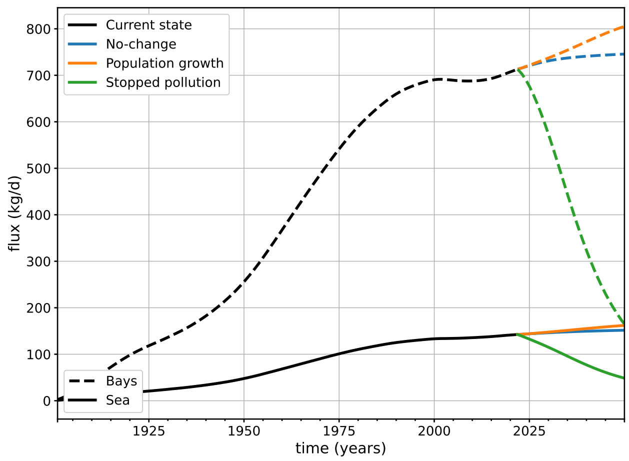

(a) N-flux conservative.

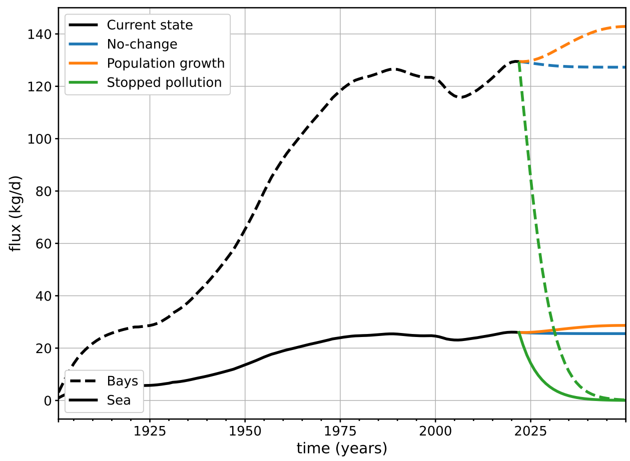

(b) N-flux decay.

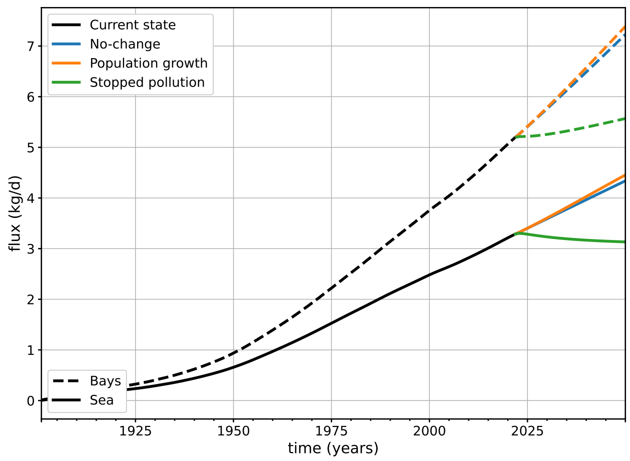

(c) P-flux.

Figure 4.18: Mass fluxes into sea (solid line) and bays (dashed line). In black the current state is given, blue is the scenario without any change, orange with population growth, and green is the scenario where pollution was stopped.

In the stopped pollution scenario, the N-outflux decreased by 75% for the conservative case of N, while for decaying N, the outflux decreased to 0 within 25 years. For the conservative case, the effect on the outflow towards the bays was larger compared to the sea (reduction of 77% and 66% respectively). These significant reductions indicate a large effect on N when the pollution stops, both when modelled as conservative and with decay.

For P, the change in flux depended on the scenario. For the population growth scenario, the mass flux was almost the same as for the no-change scenario, meaning the increase in population did not directly affect the P-flux into the bays and sea boundary. For P, it took longer to reach the boundary due to the ability to sorb, and consequently to see an effect on the mass flux. Towards the end of the simulation, the P-flux of the population growth scenario was increasing faster than the no-change scenario, but the outflux is only 2% larger in 2050 compared to the no-change scenario. This increase effect will probably increase for many years until the outflow is stable. When the influx of P was stopped in the stopped pollution scenario, the mass flux plateaued with a slight decline in the flux towards the sea. The outflux was reduced by 5% in 2050 for the sea while for the bays the outflow increased by 7%. For this scenario, there was a clear and immediate influence on the mass flux. However, when compared to the effect of pollution stop on N, a less drastic decrease in influx was observed.

When N is considered as conservative, the N:P mass ratio increased by 86% during the first 17 years, as can be observed in the graph in Figure 4.19. This is due to the delayed outflow of P by retardation. After 17 years, the N:P ratio started to decrease, as more P flowed out. For both the bays and the sea, the N:P mass ratio stayed above the Redfield ratio. This ratio was considered optimal to sustain phytoplankton growth [99], and therefore when above this ratio, the environment is called P-limited. The Redfield ratio shown in the figure, represents the mass ratio of N:P, which equals 7.23:1, differing from the commonly used molar ratio of 16:1.

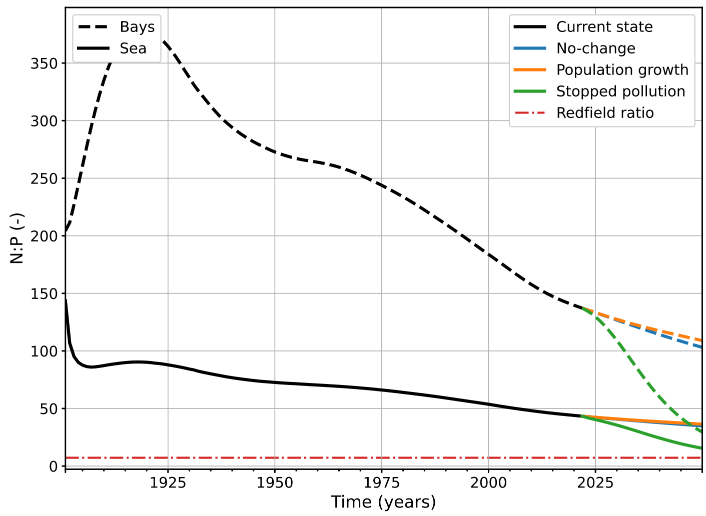

Figure 4.19: N:P mass ratio for N with a conservative behaviour. The bays are indicated with dashed line, and the sea with a solid line. The current state and the different scenarios; no-change, population growth, and stopped pollution are respectively shown in black, blue, orange, and green. The red line represents the Redfield mass ratio.

The N:P mass ratio for the current state for N with decay initially decreased during the first years of the simulation, plateaued for a period, and then decreased again, but more gradually. The stable period is longer for the N:P ratio in the sea compared to the bays. In the bays, the N:P mass ratio is higher compared to the sea. For both zones, the N:P ratio trends toward zero for the no-pollution scenario, due to the N-flux going to zero. The no-change and population growth scenarios both show a continuation of the N:P ratio decrease at a similar rate as the current state. Population growth causes a slightly less steep decline in the N:P ratio, especially observed when assessing outflow to the bays. In all three scenarios, the flux into the sea will change from P-limited to N-limited, as the N:P mass ratios are all lower than the Redfield ratio.

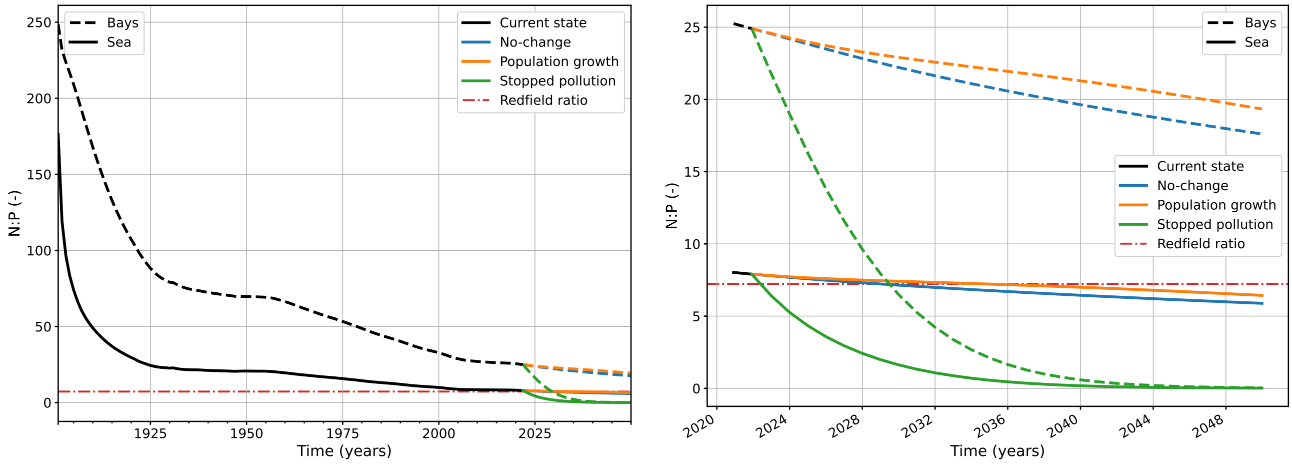

(a) N:P mass ratio from 1900 till 2050.

(b) N:P mass ratio zoomed in on the future scenarios.

Figure 4.20: N:P mass ratio for N with decay. The bays are indicated with a dashed line and the sea with a solid line. The current state and the different scenarios; no-change, population growth, and stopped pollution are respectively shown in black, blue, orange, and green. The red line represents the Redfield mass ratio.

These results represent a first model result, and further enhancements should be undertaken. A significant concern is the exclusion of fractures within the model. In reality, the aquifer consists of fractured rock that influences groundwater flow. When the aquifer is fractured, flow behaviour is governed by dual-porosity. The fractures contribute to the porosity, allowing flow, while the surrounding material primarily provides the water storage capacity [100]. This leads to the existence of both mobile and immobile domains within the aquifer.

This dual-porosity system affects the transport of nutrients through the groundwater and therefore the amount of N and P which flow out to the bays and sea. If part of the water with N reaches the boundaries much quicker, less of the nutrients are degraded, resulting in higher mass fluxes. This also holds for P, while the retardation will be the same, the outflow occurs quicker as the flow is quicker. The outflow peaks are expected to be higher, affecting the nutrient levels in the sea and bays. However, part of the nutrients will be stored in the matrix and take longer to flush out. In the case of the stopped pollution scenario simulated with fractured flow, it is expected that the initial flushing may occur more quickly, while the N stored in the rock material could prolong the duration of complete flushing from the system.

5 Recommendations

The results presented in this work are a first model result and should be interpreted with caution. To enhance accuracy, different adjustments should be made and the model parameters should be critically assessed. This chapter gives recommendations to further improve the model in future research, categorised into three sections; model structure and components, model parameters and validation data, and extension of model functionalities.

5.1. Model structure and components

The groundwater flow and the heads are an important part of this research because they affect the velocity of the nutrients, and also the height of the groundwater level and therefore the vertical position of the nutrients flow. A higher vertical position also results in a higher hydraulic conductivity due to the presence of the limestone formation, and the weathering of the CLF. Therefore it is recommended to first improve the flow model and after that, start with adjustments to the transport model. A first step in future work should be more elaborated research into the vertical distribution of the different layers. This will reduce the number of assumptions and a more realistic 3D geological model will be obtained.

Additionally, the current depth of the model is 180 m below the surface. This depth could be reduced, as flow is negligible in the deeper layers, preventing nutrients from reaching that depth. A depth of 50 m below sea level would be sufficient, as no nutrient fluxes are found below this level in the model. Reducing the model depth would decrease its size and, consequently, the running time of the simulations.

Another improvement regarding the flow model would be the implementation of fractures into the model. Although they are not exactly known, it could be done by randomising the location and adding it with the drainage package of MODFLOW, or locally adding areas with higher hydraulic conductivities or other porosity values. Important is to not overestimate the amount of fractures as it would result in an overestimation of outflows and nutrient fluxes. Therefore it is recommended to further research these fractures and their locations.

In this work, the recharge derived from rainfall was estimated based on a transient simulation of the freshwater-only model. This infiltration was higher than previously mentioned by Louws *et al.* [26]. In the determination of the recharge, no spatial differences in rainfall or land-use type were considered, similarly for the addition of the recharge to the island. The spatial differences and the land-use types affect the recharge of the groundwater and could result in local differences. For example, in urban areas, the recharge is expected to be lower compared to agricultural and natural areas where the surface is not paved allowing more infiltration.

5.2. Model parameters and validation data

The hydraulic conductivity of the weathered part of the CLF formation was defined with a decreasing gradient over the depth. This was chosen because of the wide range of values reported by Abtmaier [30]. Because the hydraulic conductivity has a major effect on the groundwater velocities, and thus on the mass fluxes, the flow velocity can differ when a better estimation of these values is done, impacting the results. The same holds for the effective porosity, these values were based on literature and were not site-specific. An overestimated porosity value is found the most common reason for overestimated travel times [101].

In this study, it was assumed that denitrification occurs with a first-order decay constant of 0.0006 d^{-1}. As mentioned before, there is a wide range of decay constants reported in the literature, with some research even reporting no decay for nitrate [89–93]. For Curaçao, it is unknown how much denitrification occurs. Therefore the transport of N was both modelled as conservative and with decay. Without decay, the N-concentrations are highly overestimated, suggesting the presence of decay. Anwar *et al.* [102] stated that groundwater systems near the coast have limited denitrification due to the lower content of organic carbon. For this reason, a better understanding of the denitrification process on Curaçao is required.

Similarly, no parameters for sorption specific to Curaçao were available. Consequently, the parameters were defined based on the literature. Linear sorption was assumed, and therefore no maximum sorb capacity was set. Retardation only affects the outflow of P, while in the case of the scenario simulations, the aquifer could reach saturation of P and the leaking P to behave as a conservative tracer and alter the concentrations and mass fluxes at the boundary.

In addition to the lack of input data, there was also limited calibration and validation data. The simulated groundwater heads were compared to measurements during the wet season. However, the model simulated more average groundwater heads due to its steady-state condition. Therefore, obtaining additional measurements under varying climatic conditions would help better judge the model's accuracy.

The nutrient concentrations for the current state were compared to observed NO_3^- and PO_4^{3-} levels. The NO_3^- concentrations indicate that the concentrations are in the correct order of magnitude for the simulation of N with decay, but the accuracy could be enhanced with more information about the reaction characteristics of N and P in the groundwater. This additional information would increase the precision of N and P-outflows to the bays and sea, and it could serve as a calibration method rather than relying solely on comparative analysis.

Improving the model results requires a thorough assessment of the model parameters, with uncertainty evaluated through a sensitivity analysis. A comprehensive sensitivity analysis would help identify the impact of various parameters, allowing for the prioritisation of the most influential ones for further evaluation.

5.3. Extension of model functionalities

The model has more functionalities and can obtain more results than shown in this work. More elaborate analyses could be performed using the current model, to increase its usability for assessing the pollution of SGD in Curaçao.

Other scenarios or local pollution measures can be simulated to assess their effects. For example, different pollution reductions could be simulated, instead of 100% pollution reduction. Based on the presented results, it can be concluded that the reduction of leakage would have significant effects on N-outflow, and therefore this should be further researched. Replacing cesspits and septic tanks with centralised sewer systems would reduce leakage and decrease the outflow of N within decades. For P, a significant amount would still flow out, and reduced pollution would not lead to a substantial reduction in outflow within the foreseeable future based on this model.

In future work, a 2D transect in the populated area could be selected for a transient simulation to investigate the effects of heavy rain on submarine groundwater discharge (SGD) and the corresponding nutrient fluxes. Boundary conditions and initial values for the 2D transect could be based on the outcomes of the variable-density model using heads, salt concentrations, and flows. This 2D model could be used for an initial estimation of the impact of fractured flow on nutrient travel times.

6 Conclusion

This thesis presents a variable-density flow model which was coupled to a nutrient transport model to understand the movement of nutrients through SGD on Curaçao. The work focused on the simulation of theoretical tracers and the simulation of nutrient leakage, particularly nitrogen (N) and phosphorus (P), from onsite sewage disposal systems (OSDS), addressing both test cases for the current state and potential future scenarios involving population growth and stopped pollution.

The groundwater flow model successfully simulated the distribution of heads and flow patterns on the island, particularly on the east side and therefore the nutrient transport simulations were focused on this region. First, theoretical tracer simulations were performed to get a first insight into the spatio-temporal behaviour of the mass fluxes on Curaçao and were used to determine the different drainage zones of the bays and the sea coastline. The mass fluxes mainly tend to flow towards the bays, 83% of the N-mass, for both the conservative case and the decaying case, discharged into the bays and for P 61% flowed towards the bays. With the obtained understanding, the current state of groundwater pollution as a result of leakage from OSDS was created. N-concentrations were higher than P-concentrations, due to both a higher N-input rate and the sorptive characteristics of P, having a larger effect on the groundwater concentrations. The simulation of N as conservative resulted in high groundwater concentrations and large mass outfluxes. When compared to NO_3 concentration measurements, the simulated concentrations were a factor of 4.5 larger (211 to 47 mg L^{-1}). The simulation of N with decay showed similar ranges of concentrations as the measurements, with approximately the same median concentration. However, the spatial distribution showed large deviations, due to over and underestimation of the concentrations, both in the same order of magnitude. The PO_4^{3-} concentration was overestimated with a factor of 11.5.

The scenario simulations, serving as a test case, provided an initial impression of the immediate and delayed impacts of population growth and stopped pollution on nutrient fluxes. While N-fluxes into the sea and bays responded quickly to changes in input, P, due to its sorptive behaviour, showed a less significant effect. In the case of a simulated stop of the OSDS pollution, the N-outflux showed a large reduction. In case of conservative transport of N, the total N-outflux is reduced by 75% within 30 years, and when N decays the total outflux into the sea and bays is reduced to 0 within 25 years. P was modelled to take longer to flush out, as it still showed an increase after 30 years for the bays. In the modelled case of persisting current pollution or increasing current pollution due to population growth, the N-flux will remain constant or reach a new constant flux level, while P-flux will continue to increase for the foreseeable future. If pollution is stopped, for example, by replacing the OSDS with a centralised sewer system, it is expected that despite uncertainties in model parameters, the reduction of N pollution would be significant after 30 years, whereas P outflow would likely remain elevated.

In this work, a model providing a first impression of the behaviour of nutrient fluxes, the current pollution state, and potential future scenarios was created. It is important to note that these results should be critically evaluated in future work by refining model parameters such as hydraulic conductivity, effective porosity, and decay constants, and performing an uncertainty analysis. In addition, fractured flow and dual-porosity systems were excluded, meaning the potential effects may differ from reality. Therefore, the results of the stopped pollution scenario should not be taken as definitive, but are subjected to uncertainty, and further research is needed.

The analysis showed several limitations, in terms of the geological model, simplification in water in and outflow, and uncertainty of the hydrogeological parameters. Improving the accuracy of the 3D geological model, more data on site-specific parameters, and transient water flow effects would enhance the reliability of future simulations. Despite these limitations, the model provided valuable insights into the behaviour of nutrients flowing through the aquifer of Curaçao. During this project, only some of the functionalities of the developed models were highlighted. In future work, different applications can be explored. From predicting the effects of specific and local anti-pollution measures to defining high-pollution coastal areas where the coral reefs are most threatened.

Reference list

[1] L. Brander and P. v. Beukering, “The total economic value of U.S. coral reefs : A review of the literature,” S. N. O. a. A. A. United States, Coral Reef Conservation Program (U.S.), and National Marine Protected Areas Center (U.S.), Eds., 2013. [Online]. Available: `https://repository.library.noaa.gov/view/noaa/8951`.

[2] A. Estep, S. Sandin, and M. Vermeij, “The state of curaçao’s coral reefs,” *The Waitt Institute*, 2017.

[3] F. Ferrario, M. W. Beck, C. D. Storlazzi, F. Micheli, C. C. Shepard, and L. Airoldi, “The effectiveness of coral reefs for coastal hazard risk reduction and adaptation,” *Nature Communications*, vol. 5, no. 1, p. 3794, May 2014. DOI: `10.1038/ncomms4794`.

[4] S. R. Carpenter, N. F. Caraco, D. L. Correll, R. W. Howarth, A. N. Sharpley, and V. H. Smith, “Nonpoint pollution of surface waters with phosphorus and nitrogen,” *Ecological applications*, vol. 8, no. 3, pp. 559–568, 1998.

[5] J. Den Haan *et al.*, “Nitrogen and phosphorus uptake rates of different species from a coral reef community after a nutrient pulse,” *Scientific Reports*, vol. 6, no. 1, p. 28 821, Jun. 2016. DOI: `10.1038/srep28821`.

[6] K. L. Knee, B. A. Layton, J. H. Street, A. B. Boehm, and A. Paytan, “Sources of Nutrients and Fecal Indicator Bacteria to Nearshore Waters on the North Shore of Kaua‘i (Hawai‘i, USA),” *Estuaries and Coasts*, vol. 31, no. 4, pp. 607–622, Sep. 2008. DOI: `10.1007/s12237-008-9055-6`.

[7] NOAA, *What is nutrient pollution?* Jun. 2024. [Online]. Available: `https://oceanservice.noaa.gov/facts/nutpollution.html` (visited on Jul. 13, 2024).

[8] United States Environmental Protection Agency (U.S. EPA), *Getting Up to Speed: Groundwater Contamination*, 2015. [Online]. Available: `https://www.epa.gov/sites/production/files/2015-08/documents/mgwcgwc1.pdf`.

[9] M. J. A. Vermeij, *Caribbean Research: A multidisciplinary approach*, 2019. (visited on Feb. 25, 2024).

[10] P. J. Withers, P. Jordan, L. May, H. P. Jarvie, and N. E. Deal, “Do septic tank systems pose a hidden threat to water quality?” *Frontiers in Ecology and the Environment*, vol. 12, no. 2, pp. 123–130, Mar. 2014, Publisher: John Wiley & Sons, Ltd. DOI: `10.1890/130131`.

[11] N. Al-Atawneh, N. Mahmoud, P. van der Steen, and P. N. L. Lens, “Characterisation of septage in partially sealed cesspit,” *Journal of Water, Sanitation and Hygiene for Development*, vol. 6, no. 4, pp. 631–639, Nov. 2016. DOI: `10.2166/washdev.2016.208`.

[12] K. Van Meter, P. Van Cappellen, and N. Basu, “Legacy nitrogen may prevent achievement of water quality goals in the Gulf of Mexico,” *Science*, vol. 360, no. 6387, pp. 427–430, 2018, Publisher: American Association for the Advancement of Science.

[13] Y.-J. Yun and K.-G. An, “Roles of N:P Ratios on Trophic Structures and Ecological Stream Health in Lotic Ecosystems,” *Water*, vol. 8, no. 1, 2016. DOI: `10.3390/w8010022`.

[14] R. C. Loehr, “Characteristics and comparative magnitude of non-point sources,” *Journal (Water Pollution Control Federation)*, pp. 1849–1872, 1974, Publisher: JSTOR.

[15] E. Luijendijk, T. Gleeson, and N. Moosdorf, “Fresh groundwater discharge insignificant for the world’s oceans but important for coastal ecosystems,” *Nature Communications*, vol. 11, no. 1, p. 1260, Mar. 2020. DOI: `10.1038/s41467-020-15064-8`.

[16] M. Taniguchi *et al.*, “Submarine Groundwater Discharge: Updates on Its Measurement Techniques, Geophysical Drivers, Magnitudes, and Effects,” *Frontiers in Environmental Science*, vol. 7, p. 141, Oct. 2019. DOI: `10.3389/fenvs.2019.00141`.

[17] H. A. Michael, A. E. Mulligan, and C. F. Harvey, “Seasonal oscillations in water exchange between aquifers and the coastal ocean,” *Nature*, vol. 436, no. 7054, pp. 1145–1148, Aug. 2005. DOI: `10.1038/nature03935`.

[18] B. K. Okuhata *et al.*, “A density-dependent multi-species model to assess groundwater flow and nutrient transport in the coastal Keauhou aquifer, Hawai‘i, USA,” *Hydrogeology Journal*, vol. 30, no. 1, pp. 231–250, Feb. 2022. DOI: `10.1007/s10040-021-02407-y`.

[19] I. R. Santos, W. C. Burnett, J. Chanton, N. Dimova, and R. N. Peterson, “Land or ocean?: Assessing the driving forces of submarine groundwater discharge at a coastal site in the Gulf of Mexico,” *Journal of Geophysical Research: Oceans*, vol. 114, no. C4, 2008JC005038, Apr. 2009. DOI: `10.1029/2008JC005038`.

[20] A. M. Wilson, “Fresh and saline groundwater discharge to the ocean: A regional perspective,” en, *Water Resources Research*, vol. 41, no. 2, 2004WR003399, Feb. 2005. DOI: `10.1029/2004WR003399`.

[21] Census, *Living accommodations Characteristics (Census 2011)*, 2011. [Online]. Available: `https://www.cbs.cw/living-accommodations-characteristics-census-2011` (visited on Apr. 9, 2024).

[22] D. Adshead *et al.*, “Evidence-based infrastructure: Curacao: National infrastructure systems modelling to support sustainable and resilient infrastructure development,” 2018, Publisher: United Nations Office for Project Services.

[23] A. De Vries, “The semi-arid environment of Curaçao: A geochemical soil survey,” *Netherlands Journal of Geosciences - Geologie en Mijnbouw*, vol. 79, no. 4, pp. 479–494, Dec. 2000. DOI: `10.1017/S0016774600021971`.

[24] M. D. Curaçao, *Climate Summary*. [Online]. Available: `https://www.meteo.cw/climate.php?Lang=Eng&St=TNCC&Sws=R11` (visited on Apr. 26, 2024).

[25] P. P. Schmutz, A. E. Potter, and E. Arnold Modlin, “Aruba, Bonaire, and Curaçao,” in *Landscapes and Landforms of the Lesser Antilles*, C. D. Allen, Ed., Cham: Springer International Publishing, 2017, pp. 293–317, ISBN: 978-3-319-55787-8. DOI: `10.1007/978-3-319-55787-8_18`.

[26] R. Louws, S. Vriend, and G. Frapporti, “The groundwater quality of Curacao. A hydrogeochemical investigation,” *H 2 O*, vol. 30, no. 26, pp. 788–791, 1997.

[27] D. J. Beets, *Guide to the field excursions on Curacao, Bonaire and Aruba, Netherlands Antilles* (GUA Papers of Geology; n.10-1977). Amsterdam: Stichting GUA, 1977.

[28] G. T. Klaver, *The Curaçao Lava Formation: An Ophiolithic Analogue of the Anomalous Thick Layer 2B of the Mid-Cretaceous Oceanic Plateaus in the Western Pacific and Central Caribbean*. Geologisch Instituut, 1987.

[29] J.-C. Hippolyte and P. Mann, "Neogene–Quaternary tectonic evolution of the Leeward Antilles islands (Aruba, Bonaire, Curaçao) from fault kinematic analysis," *Thematic Set on: Tectonics, basinal framework, and petroleum systems of eastern Venezuela, the Leeward Antilles, Trinidad and Tobago, and offshore areas*, vol. 28, no. 1, pp. 259–277, Jan. 2011. DOI: 10.1016/j.marpetgeo.2009.06.010.

[30] B. Abtmaier, "Ground water investigation of Curacao," *Unpublished report to the Department of Agriculture and Animal Husbandry, Island Government of Curacao, Netherlands Antilles*, 1979.

[31] M. Sambeek, H. Eggenkamp, and M. Vissers, "The groundwater quality of Aruba, Bonaire and Curaçao: A hydrogeochemical study," *Geologie en Mijnbouw*, vol. 79, pp. 459–466, Dec. 2000. DOI: 10.1017/S0016774600021958.

[32] C. D. Langevin, J. D. Hughes, E. R. Banta, R. G. Niswonger, S. Panday, and A. M. Provost, "Documentation for the MODFLOW 6 groundwater flow model," US Geological Survey, Tech. Rep., 2017.

[33] L. F. Konikow and D. Grove, "Derivation of equations describing solute transport in ground water," Report 77-19, 1977. DOI: 10.3133/wri7719.

[34] C. Zheng and G. D. Bennett, *Applied contaminant transport modeling*. Wiley-Interscience New York, 2002, vol. 2.

[35] C. D. Langevin, A. M. Provost, S. Panday, and J. D. Hughes, "Documentation for the MODFLOW 6 groundwater transport model," US Geological Survey, Tech. Rep., 2022.

[36] K. Spitz and J. Moreno, *A practical guide to groundwater and solute transport modeling*. New York: John Wiley, 1996, ISBN: 9780471136873.

[37] W. E. Wilson and J. E. Moore, *Glossary of hydrology*. American Geological Institute Alexandria, Virginia, 1998, ISBN: 0-922152-35-7.

[38] A. Bacani and K. Posavec, "Metode operacijskih istrazivanja u hidrogeologiji," *Sveucilišni udzbenik, Rudarsko-geološko-naftni fakultet, Sveučilište u Zagrebu*, p. 123, 2011.

[39] C. D. Langevin, S. Panday, and A. M. Provost, "Hydraulic-Head Formulation for Density-Dependent Flow and Transport," *Groundwater*, vol. 58, no. 3, pp. 349–362, May 2020. DOI: 10.1111/gwat.12967.

[40] G. P. Baxter and C. C. Wallace, "CHANGES IN VOLUME UPON SOLUTION IN WATER OF THE HALOGEN SALTS OF THE ALKALI METALS. II.," *Journal of the American Chemical Society*, vol. 38, no. 1, pp. 70–105, Jan. 1916. DOI: 10.1021/ja02258a010.

[41] C. D. Langevin, J. D. Hughes, E. R. Banta, A. M. Provost, R. G. Niswonger, and S. Panday, *MODFLOW 6 Modular Hydrologic Model*, 2017. [Online]. Available: https://doi.org/10.5066/F76Q1VQV.

[42] M. Bakker, "Python Scripting: The Return to Programming," *Groundwater*, vol. 52, no. 6, pp. 821–822, Nov. 2014, Publisher: John Wiley & Sons, Ltd. DOI: 10.1111/gwat.12269.

[43] M. Bakker *et al.*, "Scripting MODFLOW Model Development Using Python and FloPy," *Groundwater*, vol. 54, no. 5, pp. 733–739, Sep. 2016. DOI: 10.1111/gwat.12413.

[44] CARMABI, *Digital Elevation Model (DEM) for Curacao*, Unpublished dataset.

[45] A. K. Paswan, V. M. Tiwari, A. Agarwal, A. Asoka, R. Rangarajan, and S. Ahmed, "Long-term spatiotemporal variation in groundwater recharge in the highly irrigated semi-arid region of India: The intertwined relationship between climate variability and anthropogenic activities," *Groundwater for Sustainable Development*, vol. 25, p. 101 148, May 2024. DOI: 10.1016/j.gsd.2024.101148.

[46] J. P. Sorensen *et al.*, "Groundwater recharge is diffuse in semi-arid African drylands: Evidence from highly instrumented observatories," *Journal of Hydrology*, vol. 636, p. 131 227, Jun. 2024. DOI: 10.1016/j.jhydrol.2024.131227.

[47] B. Yadav *et al.*, "Estimation of groundwater recharge in semiarid regions under variable land use and rainfall conditions: A case study of Rajasthan, India," *PLOS Water*, vol. 2, no. 3, e0000061, Mar. 2023, Publisher: Public Library of Science. DOI: 10.1371/journal.pwat.0000061.

[48] D. S. Morgan, S. R. Hinkle, and R. J. Weick, "Evaluation of approaches for managing nitrate loading from on-site wastewater systems near La Pine, Oregon," Geological Survey (US), Tech. Rep. 2328-0328, 2007.

[49] C. Herrera and E. Custodio, "Groundwater flow in a relatively old oceanic volcanic island: The Betancuria area, Fuerteventura Island, Canary Islands, Spain," *Science of The Total Environment*, vol. 496, pp. 531–550, Oct. 2014. DOI: 10.1016/j.scitotenv.2014.07.063.

[50] S. Gopinath *et al.*, "Modeling saline water intrusion in Nagapattinam coastal aquifers, Tamilnadu, India," *Modeling Earth Systems and Environment*, vol. 2, no. 1, p. 2, Dec. 2015. DOI: 10.1007/s40808-015-0058-6.

[51] J. P. Masterson, J. P. Pope, M. N. Fienen, J. Monti Jr, M. R. Nardi, and J. S. Finkelstein, "Documentation of a groundwater flow model developed to assess groundwater availability in the northern Atlantic coastal plain aquifer system from Long Island, New York, to North Carolina," US Geological Survey, Tech. Rep. 2328-0328, 2016.

[52] C. Lu, P. Xin, L. Li, and J. Luo, "Seawater intrusion in response to sea-level rise in a coastal aquifer with a general-head inland boundary," *Journal of Hydrology*, vol. 522, pp. 135–140, Mar. 2015. DOI: 10.1016/j.jhydrol.2014.12.053.

[53] D. Schulze-Makuch, "Longitudinal dispersivity data and implications for scaling behavior," *Groundwater*, vol. 43, no. 3, pp. 443–456, 2005, ISSN: 1745-6584. DOI: 10.1111/j.1745-6584.2005.0051.x.

[54] J. Lin, J. B. Snodsmith, C. Zheng, and J. Wu, "A modeling study of seawater intrusion in Alabama Gulf Coast, USA," *Environmental Geology*, vol. 57, no. 1, pp. 119–130, Mar. 2009. DOI: 10.1007/s00254-008-1288-y.

[55] S. Patil and H. Chore, "Contaminant transport through porous media: An overview of experimental and numerical studies," *Advances in environmental research*, vol. 3, no. 1, pp. 45–69, 2014, Publisher: Techno-Press.

[56] A. F. Rusydi, "Correlation between conductivity and total dissolved solid in various type of water: A review," vol. 118, IOP publishing, 2018, p. 012 019, ISBN: 1755-1307.

[57] Y.-F. Chen *et al.*, "Variation in hydraulic conductivity of fractured rocks at a dam foundation during operation," *Journal of Rock Mechanics and Geotechnical Engineering*, vol. 13, no. 2, pp. 351–367, Apr. 2021. DOI: 10.1016/j.jrmge.2020.09.008.

[58] P. A. Domenico and F. W. Schwartz, *Physical and chemical hydrogeology*, 2nd. New York: John wiley & sons, 1997, ISBN: 978-0-471-59762-9.

[59] C. D. Hunt Jr, "Geohydrology of the island of Oahu, Hawaii," US Geological Survey, Tech. Rep., 1996.

[60] K. Rotzoll and C. H. Fletcher, "Assessment of groundwater inundation as a consequence of sea-level rise," *Nature Climate Change*, vol. 3, no. 5, pp. 477–481, 2013.

[61] D. S. Oki, *Numerical simulation of the effects of low-permeability valley-fill barriers and the redistribution of ground-water withdrawals in the Pearl Harbor area, Oahu, Hawaii*. US Department of the Interior, US Geological Survey, 2005.

[62] C. Turnadge and S. Lamontagne, "A MODFLOW-based approach to simulating wetland–groundwater interactions in the Lower Limestone Coast Prescribed Wells Area," *Goyder Institute for Water Research Technical Report Series*, no. 15/12, 2015.

[63] A. Romanazzi and M. Polemio, "Modelling of coastal karst aquifers for management support: A case study of Salento (Apulia, Italy)," *Italian journal of engineering geology and environment*, no. 1, pp. 65–83, Jun. 2013, Number: 1. DOI: 10.4408/IJEGE.2013-01.O-05.

[64] R. S. Crosbie, P. Davies, N. Harrington, and S. Lamontagne, "Ground truthing groundwater-recharge estimates derived from remotely sensed evapotranspiration: A case in South Australia," en, *Hydrogeology Journal*, vol. 23, no. 2, pp. 335–350, Mar. 2015. DOI: 10.1007/s10040-014-1200-7.

[65] D. K. S. Y. Klaas and M. A. Imteaz, "Investigating the impact of the properties of pilot points on calibration of groundwater models: Case study of a karst catchment in Rote Island, Indonesia," *Hydrogeology Journal*, vol. 25, no. 6, pp. 1703–1719, Sep. 2017. DOI: 10.1007/s10040-017-1590-4.

[66] S. Yoshimoto, T. Tsuchihara, S. Ishida, T. Masumoto, and M. Imaizumi, "Groundwater flow and transport and potential sources of groundwater nitrates in the Ryukyu Limestone as a mixed flow aquifer in Okinawa Island, Japan," *Paddy and Water Environment*, vol. 9, no. 4, pp. 367–384, Dec. 2011. DOI: 10.1007/s10333-011-0252-8.

[67] H. Sun, D. Zhong, and W. Zhan, "Reservoir characteristics in the Cretaceous volcanic rocks of Songliao Basin, China: A case of dynamics and evolution of the volcano-porosity and diagenesis," *Energy Exploration & Exploitation*, vol. 37, no. 2, pp. 607–625, Mar. 2019. DOI: 10.1177/0144598718812546.

[68] K. Moharir, C. Pande, and S. Patil, "Inverse modelling of aquifer parameters in basaltic rock with the help of pumping test method using MODFLOW software," *Geoscience Frontiers*, vol. 8, no. 6, pp. 1385–1395, Nov. 2017. DOI: 10.1016/j.gsf.2016.11.017.

[69] A. A. Douglas, J. L. Osiensky, and C. K. Keller, "Carbon-14 dating of ground water in the Palouse Basin of the Columbia River basalts," *Journal of Hydrology*, vol. 334, no. 3-4, pp. 502–512, 2007, Publisher: Elsevier.

[70] A. Navarre-Sitchler, S. L. Brantley, and G. Rother, "How Porosity Increases During Incipient Weathering of Crystalline Silicate Rocks," *Reviews in Mineralogy and Geochemistry*, vol. 80, no. 1, pp. 331–354, 2015. DOI: 10.2138/rmg.2015.80.10.

[71] A. Hassan, G. Elsaeed, M. Nagaty, and E. Abdelghani, "Groundwater Flow Modeling in a Nubian Sandstone Aquifer, South Western Desert, Egypt," *Journal of Scientific Research and Reports*, vol. 6, no. 4, pp. 243–254, Jan. 2015. DOI: 10.9734/JSRR/2015/15736.

[72] R. C. Heath, "Basic ground-water hydrology," English, Reston, VA, Report 2220, 1983, p. 91. [Online]. Available: https://pubs.usgs.gov/publication/wsp2220.

[73] D. B. McWhorter and D. K. Sunada, *Ground-water hydrology and hydraulics*. Water Resources Publication, 1977.

[74] R. Fisher *et al.*, "Site 231," vol. 24, Oct. 1974. DOI: 10.2973/dsdp.proc.24.102.1974.

[75] C. Nugraha, H. Shimada, T. Sasaoka, M. Ichinose, and I. Manege, "Waste rock characteristics at tropical coal mine area: A case study of PT. Kaltim Prima Coal, Indonesia," 2009.

[76] P. Stepien, Z. Rusin, and A. Bracka, "Analysis of the Pore Space of the Swietokrzyskie Region's Jurassic Devonian Limestones Based on Testing with the Use Mercury Intrusion Porosimetry and Differential Scanning Calorimetry," *IOP Conference Series: Materials Science and Engineering*, vol. 471, p. 032 072, Feb. 2019. DOI: 10.1088/1757-899X/471/3/032072.

[77] E. L. Lewis and R. G. Perkin, "Salinity: Its definition and calculation," *Journal of Geophysical Research: Oceans*, vol. 83, no. C1, pp. 466–478, Jan. 1978. DOI: 10.1029/JC083iC01p00466.

[78] W. D. Robertson, D. R. Van Stempvoort, and S. L. Schiff, "Review of phosphorus attenuation in groundwater plumes from 24 septic systems," *Science of The Total Environment*, vol. 692, pp. 640–652, Nov. 2019. DOI: 10.1016/j.scitotenv.2019.07.198.

[79] S. F. Korom, "Natural denitrification in the saturated zone: A review," *Water Resources Research*, vol. 28, no. 6, pp. 1657–1668, 1992. DOI: 10.1029/92WR00252.

[80] P. A. Herrera, C. Langevin, and G. Hammond, "Estimation of the Water Table Position in Unconfined Aquifers with MODFLOW," *Groundwater*, vol. 61, no. 5, pp. 648–662, Sep. 2023. DOI: 10.1111/gwat.13270.

[81] S. Painter, H. Başağaoğlu, and A. Liu, "Robust representation of dry cells in single-layer MODFLOW models," *Groundwater*, vol. 46, no. 6, pp. 873–881, 2008.

[82] E. Keating and G. Zyvoloski, "A stable and efficient numerical algorithm for unconfined aquifer analysis," *Groundwater*, vol. 47, no. 4, pp. 569–579, 2009.

[83] C. S. Heppner, J. R. Nimmo, G. J. Folmar, W. J. Gburek, and D. W. Risser, "Multiple-methods investigation of recharge at a humid-region fractured rock site, Pennsylvania, USA," *Hydrogeology Journal*, vol. 15, pp. 915–927, 2007, Publisher: Springer.

[84] R. W. Healy and P. G. Cook, "Using groundwater levels to estimate recharge," *Hydrogeology journal*, vol. 10, pp. 91–109, 2002.

[85] M. P. Anderson, W. W. Woessner, and R. J. Hunt, *Applied groundwater modeling: simulation of flow and advective transport*, Second edition. Amsterdam Boston Heidelberg London New York Oxford Paris San Diego San Francisco Singapore Sydney Tokyo: Elsevier, Academic Press, 2015, ISBN: 978-0-12-058103-0.

[86] M. ter Bals, "Curaçao Population Projections 2015-2050," 2015.

[87] CBS, *Population*, Page. [Online]. Available: https://www.cbs.cw/population (visited on Jun. 16, 2024).

[88] R. Crites and G. Tchobanoglous, *Small and decentralized wastewater management systems* (McGraw-Hill series in water resources and environmental engineering), eng. Boston: WCB/McGraw-Hill Boston, 1998, ISBN: 0-07-289087-8 978-0-07-289087-7 0-07-116784-6 978-0-07-116784-0.

[89] I. Karlović, K. Posavec, O. Larva, and T. Marković, "Numerical groundwater flow and nitrate transport assessment in alluvial aquifer of Varaždin region, NW Croatia," *Journal of Hydrology: Regional Studies*, vol. 41, p. 101 084, Jun. 2022. DOI: 10.1016/j.ejrh.2022.101084. (visited on Jul. 18, 2024).

[90] M. N. Almasri and J. J. Kaluarachchi, "Modeling nitrate contamination of groundwater in agricultural watersheds," *Journal of Hydrology*, vol. 343, no. 3-4, pp. 211–229, Sep. 2007. DOI: 10.1016/j.jhydrol.2007.06.016.

[91] A. Sieczka, F. Bujakowski, T. Falkowski, and E. Koda, "Morphogenesis of a Floodplain as a Criterion for Assessing the Susceptibility to Water Pollution in an Agriculturally Rich Valley of a Lowland River," *Water*, vol. 10, no. 4, p. 399, Mar. 2018. DOI: 10.3390/w10040399.

[92] R. Shakeri, H. R. Nassery, and T. Ebadi, "Numerical modeling of groundwater flow and nitrate transport using MODFLOW and MT3DMS in the Karaj alluvial aquifer, Iran," *Environmental Monitoring and Assessment*, vol. 195, no. 1, p. 242, Dec. 2022. DOI: 10.1007/s10661-022-10881-4.

[93] X. Wei, R. T. Bailey, R. M. Records, T. C. Wible, and M. Arabi, "Comprehensive simulation of nitrate transport in coupled surface-subsurface hydrologic systems using the linked SWAT-MODFLOW-RT3D model," *Environmental Modelling & Software*, vol. 122, p. 104 242, Dec. 2019. DOI: 10.1016/j.envsoft.2018.06.012.

[94] P. Harris, "Water quality impacts from on-site waste disposal systems to coastal areas through groundwater discharge," *Environmental Geology*, vol. 26, no. 4, pp. 262–268, 1995.

[95] K. S. Lowe *et al.*, *Influent Constituent Characteristics of the Modern Waste Stream from Single Sources*. IWA Publishing, Mar. 2010, doi: https://doi.org/10.2166/9781780403519, ISBN: 978-1-78040-351-9.

[96] J. E. McCray, S. L. Kirkland, R. L. Siegrist, and G. D. Thyne, "Model parameters for simulating fate and transport of on-site wastewater nutrients.," *Ground water*, vol. 43, no. 4, pp. 628–639, Aug. 2005. DOI: 10.1111/j.1745-6584.2005.0077.x.

[97] I. Valiela *et al.*, "Nitrogen loading from coastal watersheds to receiving estuaries: New method and application," *Ecological Applications*, vol. 7, no. 2, pp. 358–380, 1997. DOI: https://doi.org/10.1890/1051-0761(1997)007[0358:NLFCWT]2.0.CO;2.

[98] L. Sikora and R. Corey, "Fate of nitrogen and phosphorus in soils under septic tank waste disposal fields," *Transactions of the ASAE*, vol. 19, no. 5, pp. 866–0870, 1976.

[99] A. C. Redfield, "The biological control of chemical factors in the environment," *American scientist*, vol. 46, no. 3, 230A–221, 1958, ISSN: 0003-0996.

[100] J. Šimůnek, N. J. Jarvis, M. van Genuchten, and A. Gärdenäs, "Review and comparison of models for describing non-equilibrium and preferential flow and transport in the vadose zone," *Soil Hydrological Properties and Processes and their Variability in Space and Time*, vol. 272, no. 1, pp. 14–35, Mar. 2003. DOI: 10.1016/S0022-1694(02)00252-4.

[101] S. R. H. Worthington, "Diagnostic tests for conceptualizing transport in bedrock aquifers," *Journal of Hydrology*, vol. 529, pp. 365–372, Oct. 2015. DOI: 10.1016/j.jhydrol.2015.08.002.

[102] N. Anwar, C. Robinson, and D. A. Barry, "Influence of tides and waves on the fate of nutrients in a nearshore aquifer: Numerical simulations," *Advances in Water Resources*, vol. 73, pp. 203–213, Nov. 2014. DOI: 10.1016/j.advwatres.2014.08.015.

[103] N. Zhang, M. He, B. Zhang, F. Qiao, H. Sheng, and Q. Hu, "Pore Structure Characteristics and Permeability of Deep Sedimentary Rocks Determined by Mercury Intrusion Porosimetry," *Journal of Earth Science*, vol. 27, no. 4, pp. 670–676, Jul. 2016. DOI: 10.1007/s12583-016-0662-z.

[104] E. Kozlovsky, "Geology and the Environment. Vol. I, Water Management and the Geoenvironment," 1988, Publisher: UNESCO Paris, UNEP Nairobi.

[105] E. O. Frind, W. H. M. Duynisveld, O. Strebel, and J. Boettcher, "Modeling of multicomponent transport with microbial transformation in groundwater: The Fuhrberg Case," *Water Resources Research*, vol. 26, no. 8, pp. 1707–1719, 1990. DOI: 10.1029/WR026i008p01707.

[106] G. Uffink, "Determination of denitrification parameters in deep groundwater. A pilot study for several pumping stations in the Netherlands," Rijksinstituut voor Volksgezondheid en Milieu RIVM, Report, May 2004. [Online]. Available: https://rivm.openrepository.com/handle/10029/9058 (visited on Jul. 15, 2024).

[107] R. Eppinger and K. Walraevens, "Mobility and removal of nitrate in heterogeneous Eocene aquifers," eng, in *Groundwater Quality: Remediation and Protection*, Issue: 250 Number: 250, 1998, pp. 11–18. [Online]. Available: http://hdl.handle.net/1854/LU-279139 (visited on Jul. 23, 2024).

[108] K. Kovar and M. Herbert, *Groundwater Quality: Remediation and Protection : Proceedings of the GQ'98 Conference Held in Tübingen, Germany, from 21 to 25 September, 1998*. International Association of Hydrological Sciences, 1998, ISBN: 978-1-901502-55-8.

A
Model overview

In the overview, the different packages used for the different models are given. Also, the connections of the different models are shown. As can be seen, the simulated heads and flows were used as input for the nutrient transport model.

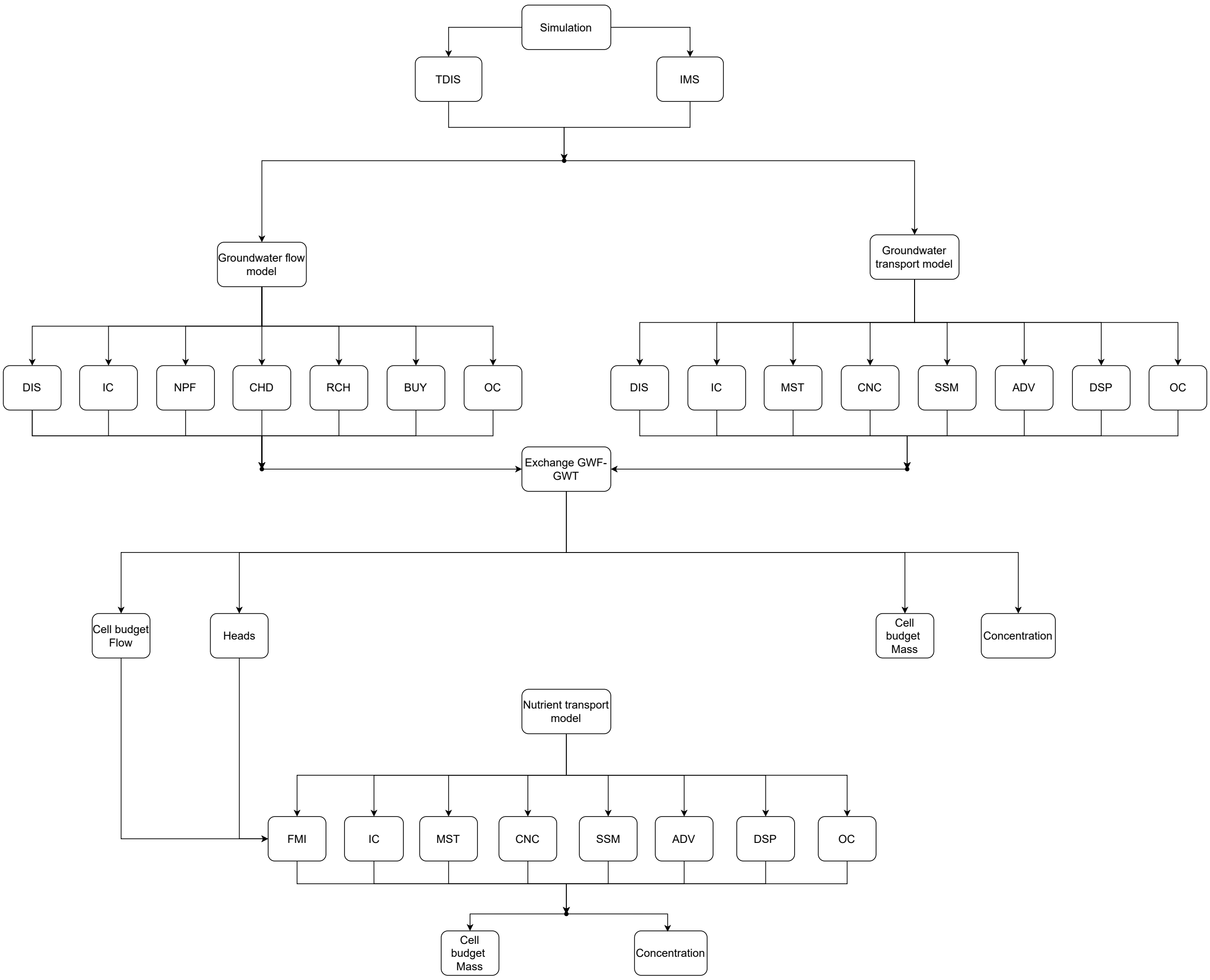

Figure A.1: Overview of the model structures in MODFLOW. All abbreviations are the packages named in Table 3.1.

B
Convergence analysis

The grid cell size of the model affects the outcome values, therefore a convergence analysis was performed to determine the optimal grid size. This optimum was based on the computation time and the convergence of the heads. In the convergence analysis, the freshwater-only flow model was used with varying cell dimensions. The groundwater head was calculated on four locations, two on the west side and two on the east side, for the different grid sizes. These groundwater heads were evaluated against the grid cell size, and the optimal grid cell size was chosen if the groundwater level plateaued. Therefore a grid cell size of 100 m by 100 m was chosen, as the heads converged and a smaller cell would increase the computation time significantly.

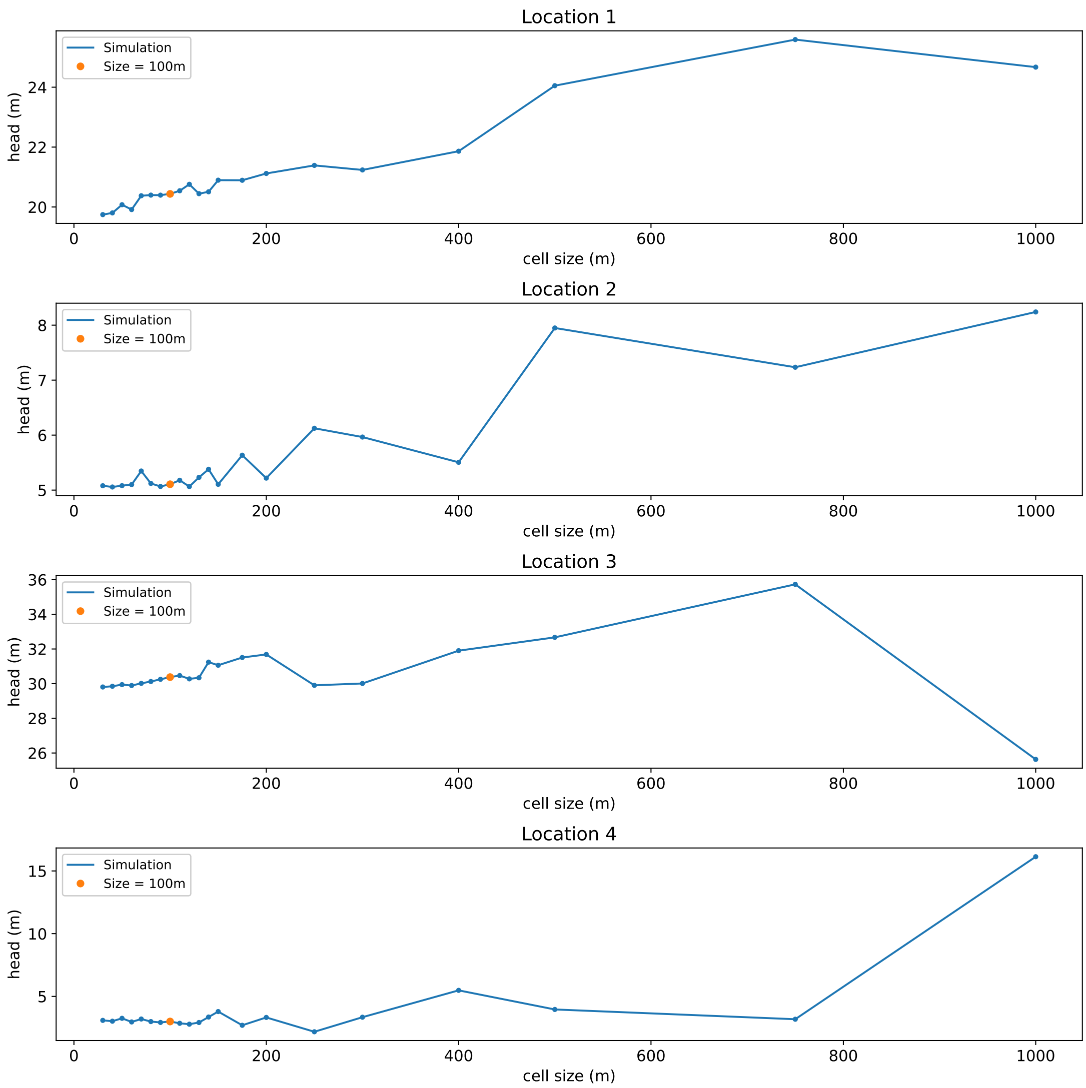

Figure B.1: Convergence analysis to determine the cell size of the model. The heads were evaluated on four locations, with in each graph the simulated added against the cell size.

C
IDOMAIN

Figure C.1 shows the IDOMAIN before smoothing and as can be seen the boundary cells show inconsistencies. These were smoothened manually and the results is given in Figure C.2.

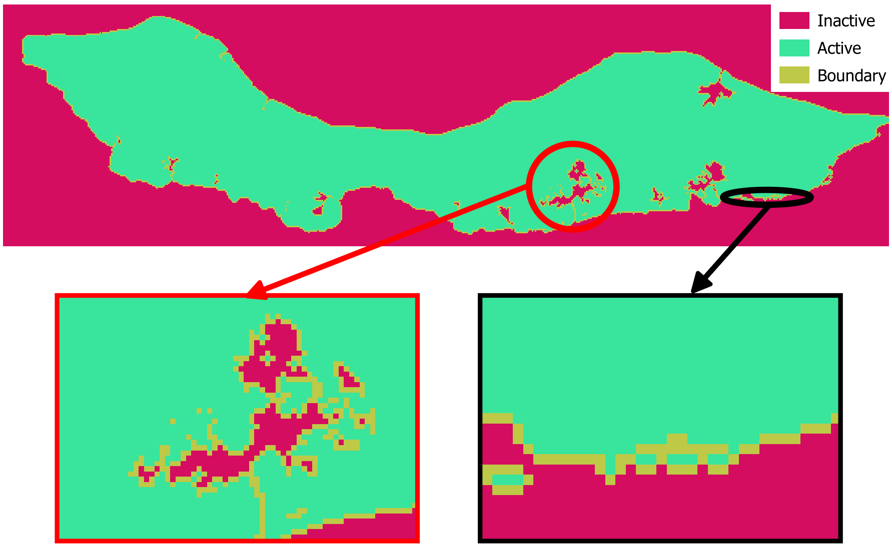

Figure C.1: IDOMAIN array before smoothing.

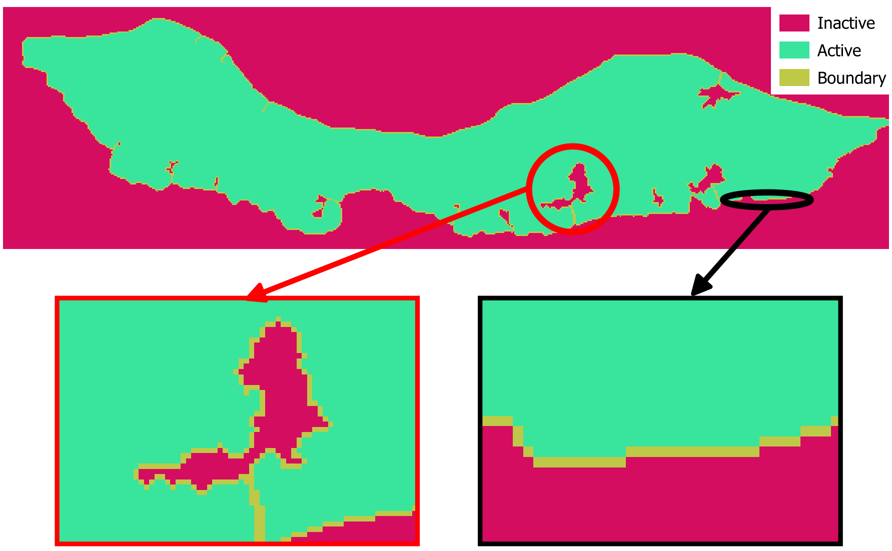

Figure C.2: IDOMAIN array after manual smoothing.

D Hydrogeological parameters

D.1. Hydraulic conductivity

For the hydraulic conductivity of CLF, MCF and the Knip Group, experimental data from pumping tests performed on Curaçao were available [30]. These pumping tests, performed in wells on different locations on the island, had reported outcomes in terms of 'transmissivity'. These were converted to hydraulic conductivity using a simple relation:

$$K = \frac{T}{D}, \tag{D.1}$$

where K (m d^{-1}), T (m^2 d^{-1}), and D (m) denoted the hydraulic conductivity, the transmissivity, and the well depth respectively.

The resulting hydraulic conductivities for each geological formation are shown in Figure D.1. The median values of these experiments were used as initial values for hydraulic conductivities. For limestone, there were no pump-test data available, and therefore it was based on literature. A wide range of values were found varying from 0.1 m d^{-1} to even 10 000 m d^{-1} [59–66].

After iteration, the hydraulic conductivities for MCF, Knip Group, and limestone were set at 0.02 m d^{-1}, 0.3 m d^{-1}, and 10 m d^{-1} respectively. As the hydraulic conductivity of CLF appeared highly dependent on its weathering, in turn related to the depth of the formation, it was decided to add the conductivity of the weathered part of the CLF as a gradient. The final used hydraulic conductivity for the top layer was set to the 75th percentile of the experimental measurements (9.5 m d^{-1}) and the less weathered bottom layer of the weathered CLF was assigned the 25th percentile (0.88 m d^{-1}). The eight layers in between were linearly interpolated. Because the unweathered part of the CLF is nearly impermeable, here a gradient in conductivity was added from the top layer (0.01 m d^{-1}) to the bottom layer ($1 \cdot 10^{-4}$ m d^{-1}).

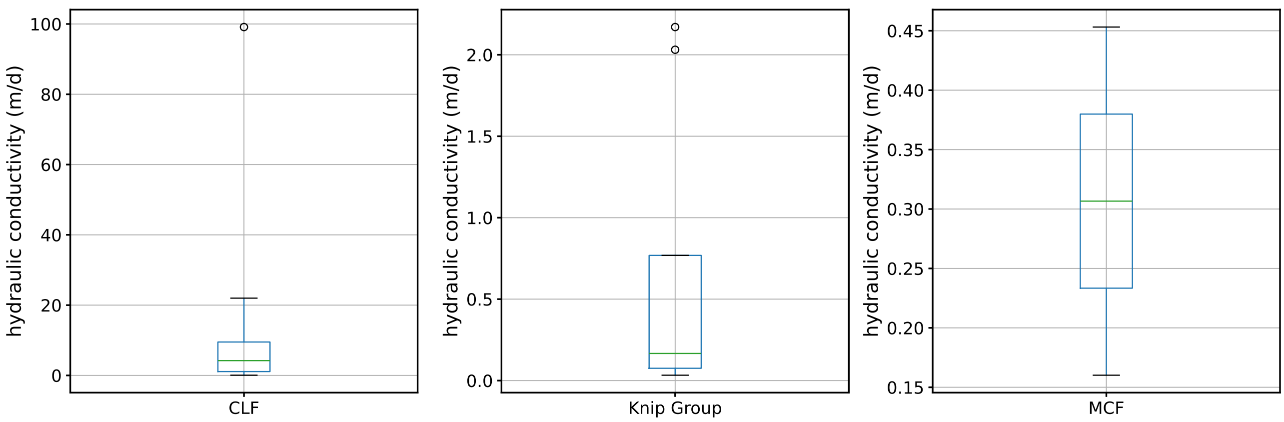

Figure D.1: Boxplot with pumping test data obtained from Abtmaier [30]. CLF = Curaçao Lava Formation and MCF = Mid Curaçao Formation.

Chen *et al.* [57] performed field tests and found for basalt layers, comparable geological formation to CLF, an anisotropy ratio ranging from 0.025 to 0.3. The upper, more weathered layers have a higher ratio compared to the lower, unweathered layers. For simplicity, a constant value of 0.2 was assumed for all the geological formations in the model.

Table D.1: Statistics of pumping test performed by Abtmaier [30]. CLF = Curaçao Lava Formation, MCF = Mid Curaçao Formation.

Geology	Count	Mean	Std	Min	25%	50%	75%	Max
CLF	41	8.56	15.85	0.056	0.88	4.21	9.51	99.13
Knip Group	8	0.63	0.91	0.033	0.075	0.17	0.77	2.17
MCF	2	0.31	0.21	0.16	0.23	0.31	0.38	0.45

D.2. Effective porosity

The effective porosity of CLF was based on different effective porosity values found for basalt, ranging from 1% to 15% [67–69]. Navarre-Sitchler *et al.* [70] found that the effective porosity of unweathered rocks is lower compared to the effective porosity of the weathered part of the basalt layer. For this reason, a value of 5% and 1% was used for respectively the weathered and unweathered part of CLF. Because the Knip Group consists of sand- and mudstones, the effective porosity value was based on these types. Zhang *et al.* [103] found an effective porosity for sand- and mudstone of 3.96% and 14.03% respectively, but Hassan *et al.* [71] stated a higher effective porosity of 21% to 30% for sandstone. Averaging these values, the effective porosity of the Knip Group was set to 14%. MCF mainly consists of sand- and siltstones and the effective porosity was based on effective porosity found for these individual geologies. The effective porosity of siltstone can range from 21% to 41% [58, 72, 73], resulting in the effective porosity of MCF of 20%. For limestone, an effective porosity of 12% was used, based on the average value of the range 1 to 24% [58, 72, 73]. These values are summarised in Table 3.2.

D.3. Decay parameters

The first-order decay constants are based on the half-life time of NO_3 and vary from 1 to 20 years (Table D.2). In this work, it was chosen to simulate N/NO_3 with decay. It is important to note that this was a test case and could differ in reality. When considering Kozlovsky [104] identified half-life time as an outlier, the average of the remaining reported half-life times is approximately 3 years. This corresponds to a first-order decay coefficient of $6 \cdot 10^{-4}$ d^{-1} (Equation (3.7)), as used in the current model.

Table D.2: Half-life time of NO_3 used in previous studies.

Source	Half-life time (years)
Frind *et al.* [105]	1 - 2.3
Kozlovsky [104]	20
Uffink [106]	1.4 - 7.5
Eppinger and Walraevens [107]	3.7
Kovar and Herbert [108]	3.7
Korom [79]	1.2 - 2.1

D.4. Sorption parameters

The bulk density of Knip Group is determined based on values for sand and mudstone, respectively 2210 and 2270 kg m^{-3} [75], and set to the average of these values; 2240 kg m^{-3}. For MCF, the average of sand and siltstone was used, respectively 2210 and 2380 kg m^{-3} and therefore set to 2300 kg m^{-3}. For basalt, a range between 2670 and 2860 kg m^{-3} was found, with deeper located basalt having a higher bulk density [74]. Therefore the bulk density of weathered basalt was set to 2670 kg m^{-3} and for unweathered basalt 2860 kg m^{-3} was used. For limestone a bulk density of 2500 kg m^{-3} was used [76]. Besides the bulk density, also the distribution coefficient was required. As little data was found, a K_d value of $1.3 \cdot 10^{-3}$ m^3 kg^{-1} was used for all the formations [78].

E

Recharge estimation

The recharge was estimated based on daily rainfall data and observed groundwater time series. The steady-state groundwater model was converted to a transient model with time steps of one day. Each day was defined as a stress period with a varying recharge value. Storage coefficients were also added as they are required in transient models, a specific yield was used for all geological formations. Five different scenarios with varying amounts of recharge, calculated from the rainfall, were created and the simulation period was set to 1 year. The recharge was determined by subtracting 7 mm of the daily rainfall, based on a average evaporation rate [23] in Curacao. If the daily rainfall exceeded this threshold, the threshold was subtracted and a percentage, which accounted for runoff, of the remaining rainfall was added to the model as recharge. These five scenarios are given in Table E.1. The recharge was estimated by comparing the groundwater heads at the four diver locations. In the scenario where the simulated groundwater heads resemble the observed groundwater heads most, the total recharge was converted to a percentage of the mean annual rainfall for the two-year period. The scenario with 15% of a rain event as infiltration was chosen as most resembling, this resulted in total infiltration per year of 7% of the average rainfall for the years 2021-2022.

Table E.1: Scenarios to determine the recharge based on rainfall.

Evaporation	Percentage of rain event (%)
7	5
7	10
7	15
7	20
7	25

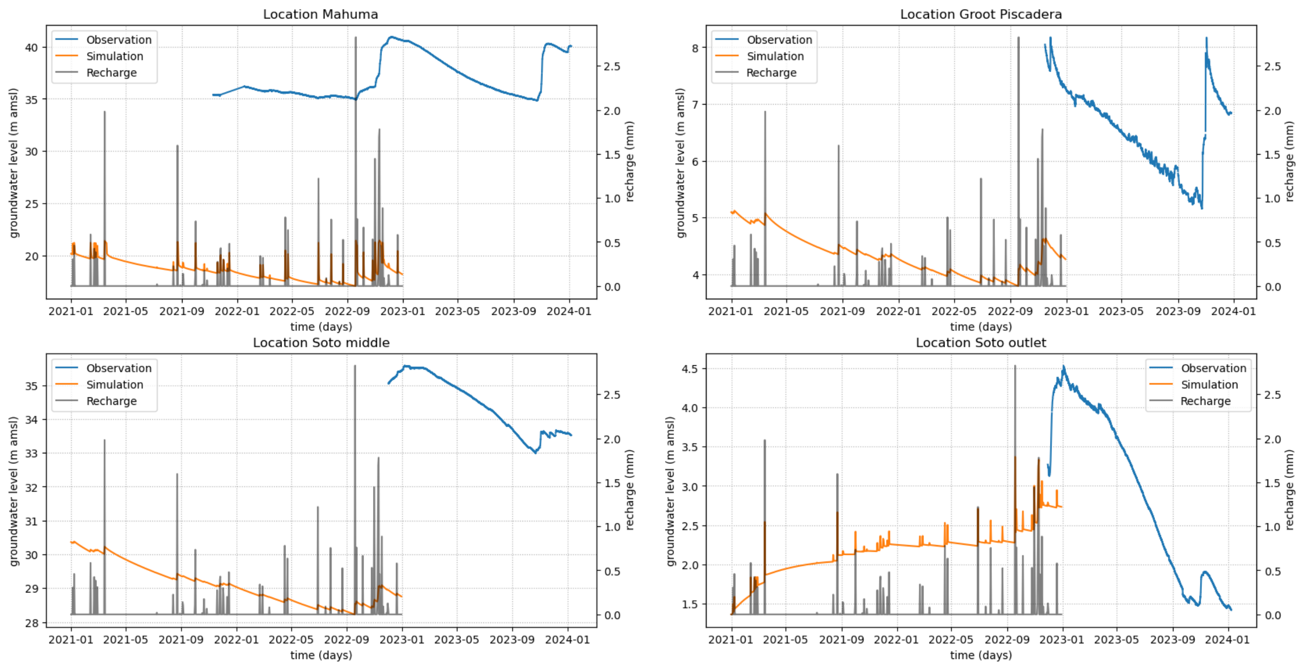

(a) 5% of rain event as recharge

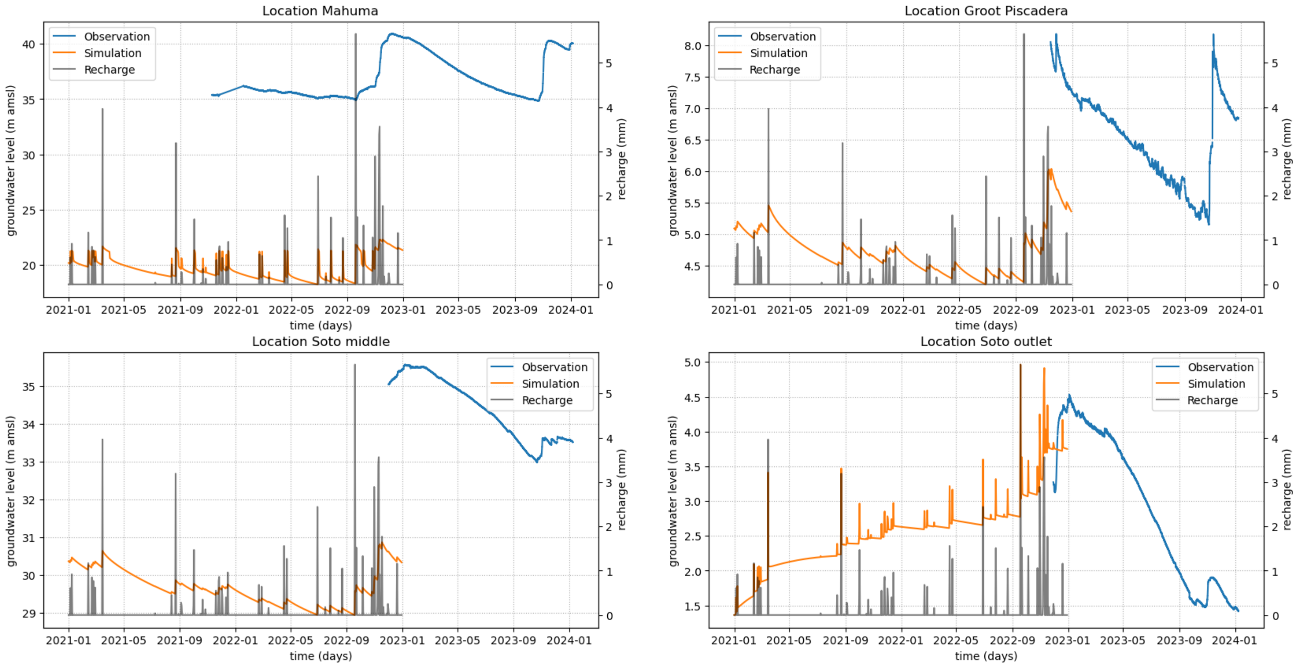

(b) 10% of rain event as recharge

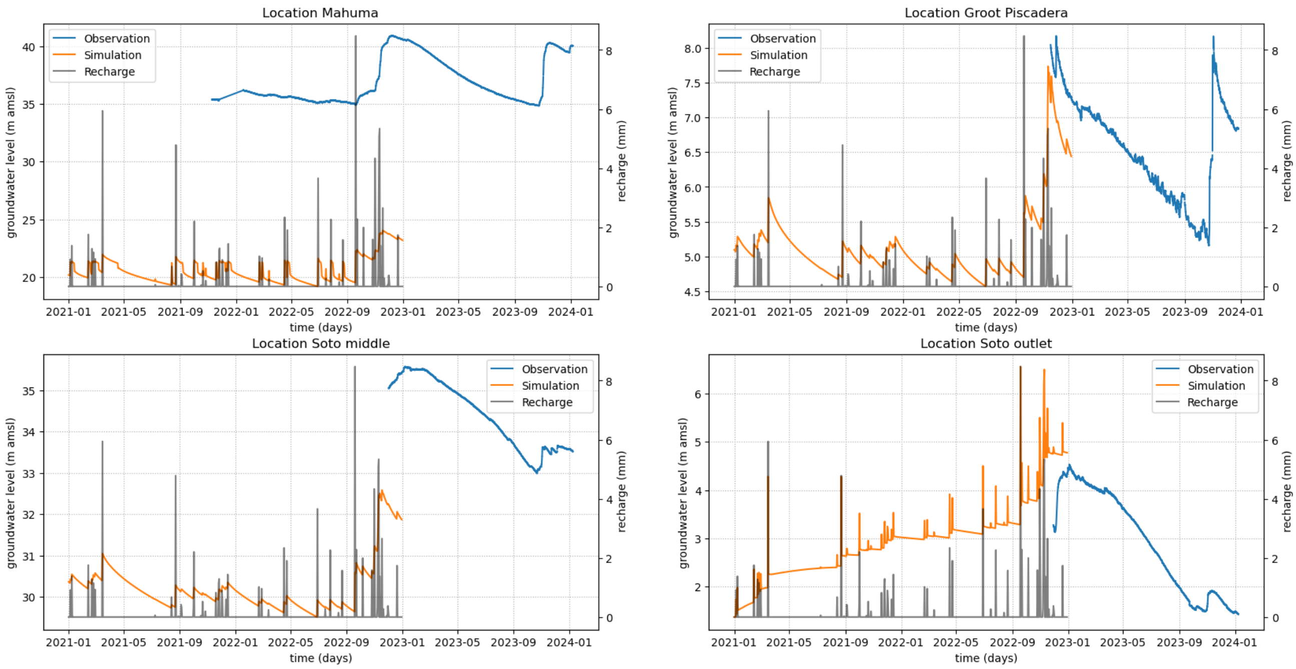

(c) 15% of rain event as recharge

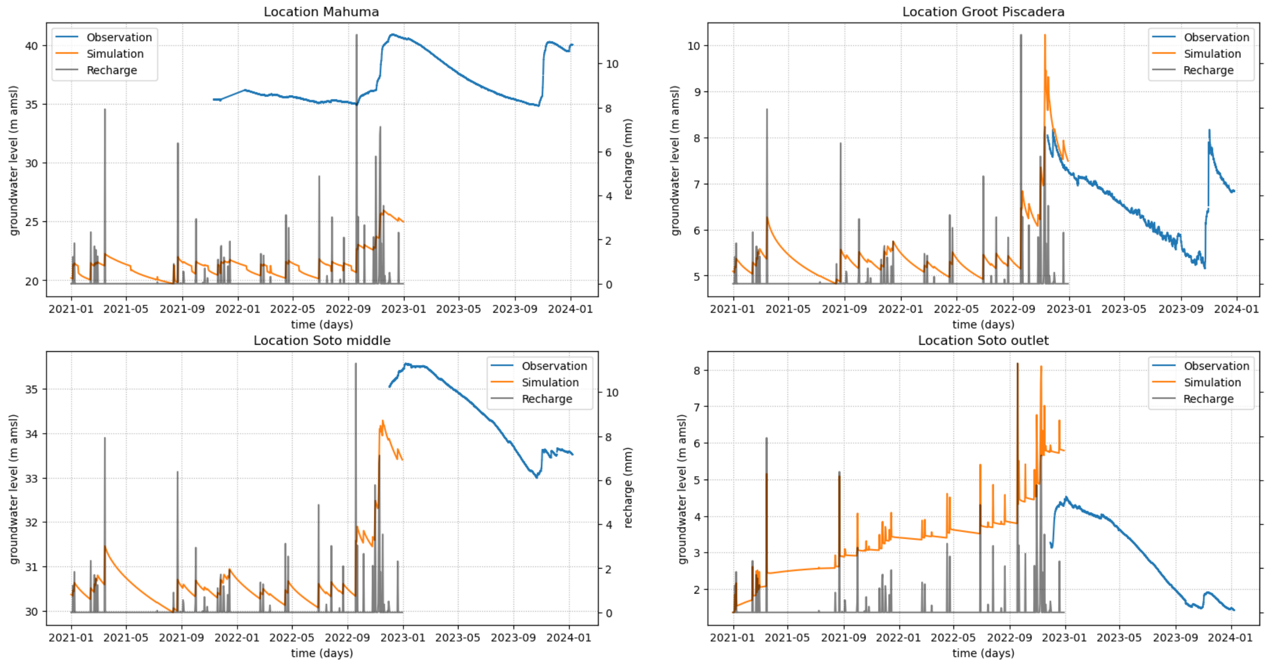

(d) 20% of rain event as recharge

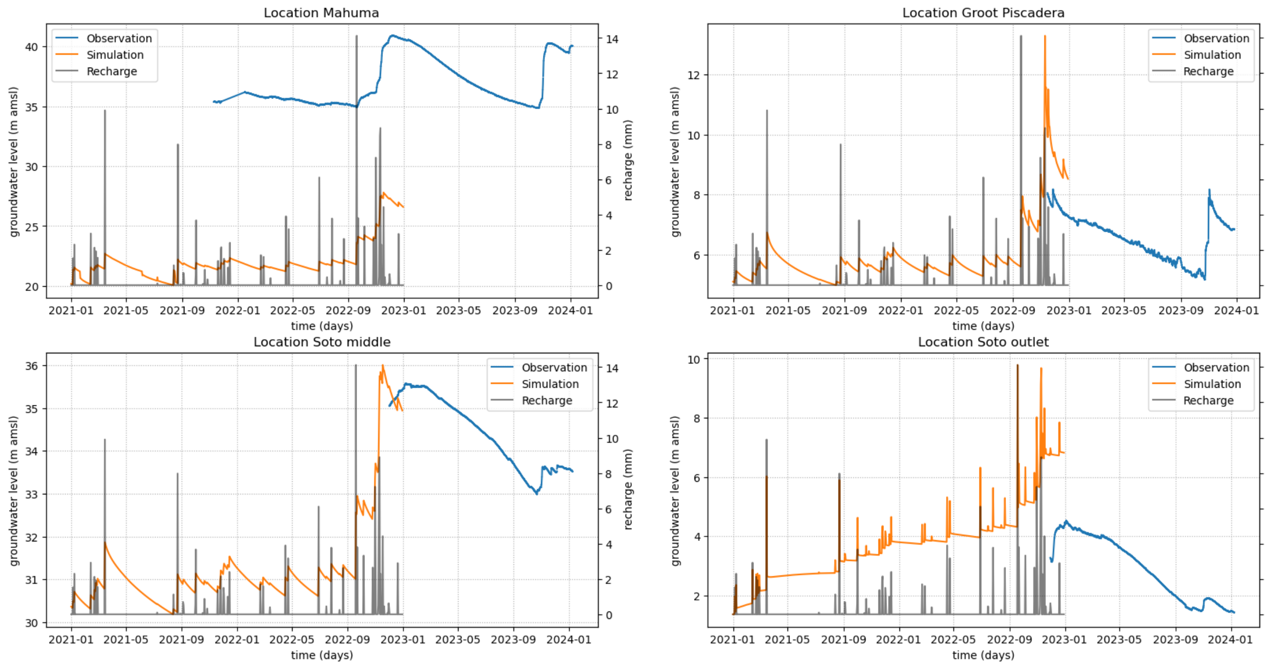

(e) 25% of rain event as recharge

Figure E.1: Transient simulations of groundwater heads along with the recharge and observed heads on four locations.

F
Running times MODFLOW model

Due to the great extent of the model grid, the running times of the variable-density model were very long. Because it was not possible to automatically calculate the steady-state situation for this model, the simulation period was set to 4500 years with time steps of 1 years. This resulted in a running time of 6 days. Smaller time steps would decrease the Courant number and therefore increase the numerical stability of the model. Due to the long simulation times, this was not possible in this work.

For the nutrient transport simulations, the time step was decreased to 0.5 years. Resulting in simulation time ranging from 30 minutes to 4 hours. This was dependent on the simulation period, a simulation of 30 years with time steps of 0.5 years was done in 30 minutes, whereas the tracer simulations with a simulation period of 250 years and time steps of 0.5 year, were done in 4 hours.

It is recommended to do future simulations and resimulation of the variable-density model on a server or a desktop with strong power.

G

Flow and heads for FMI

The flow field of the variable-density groundwater model was used to do the nutrient simulations. For these simulations, the FMI package was used, in which the budget and head files were added. By doing this, the variable-density model did not need to be re-calculated, which saved (a lot of) computation time. The FMI required a budget and head file with data of either one time step indicated with time step 1 and period 1, or data for all time steps calculated. When saving the flows for each time step, the file size would be too large to be saved on the hard disk ($\approx$ 500 GB). Therefore it was chosen to save the with a frequency of 100 years, to still be able to assess if the flows are approaching steady-state at the end. This resulted in problems loading the flow file to the FMI package, because the file contained the time step index of the end of the simulation, which was 4500 instead of 1 which was required by FMI. This had to be adjusted for all the different flow budget types. Also, the head file had to be changed to time step index 1, and removing all other heads if saved. This was done by copying the binary file and removing all the data except for the last time step. The index which indicated the time step number was changed from 4500 to 1. Now these budget and head files were used as input for the FMI package and represented the steady-state flow field. A Python script was created which could do this transformation of the files.

H Population growth

The population growth factor per year is given in the table below based on the projection considering constant fertility [86].

	2022-2024	2025-2029	2030-2034	2035-2039	2040-2044	2045-2049
Annual rate of change (%)	1.0	0.8	0.5	0.3	0.0	-0.1

Table H.1: Annual change of population based on constant fertility projection [86].

Simulated groundwater heads - Freshwater only model

Groundwater heads of Curaçao simulated with the freshwater-only model are given in Figure I.1. Figure I.2 show the difference between the simulated heads with the freshwater-only model and the variable-density model. A cross-section indicating the flow directions is given in Figure I.3.

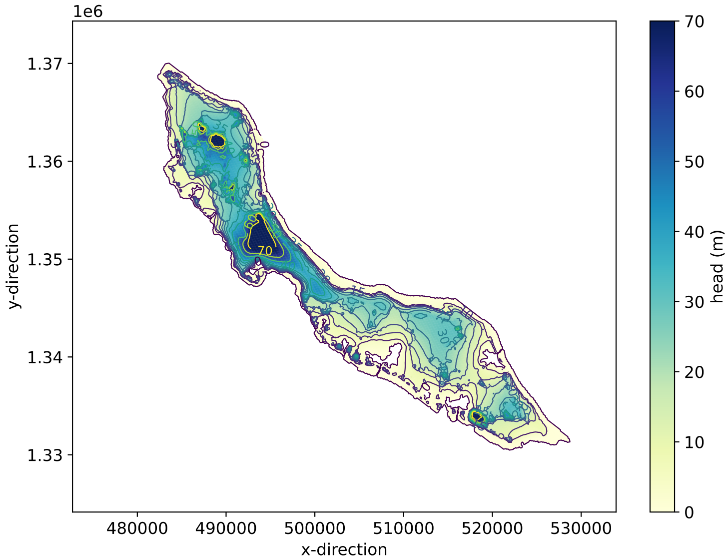

Figure I.1: Freshwater heads distribution with the contour lines indicating different groundwater head levels.

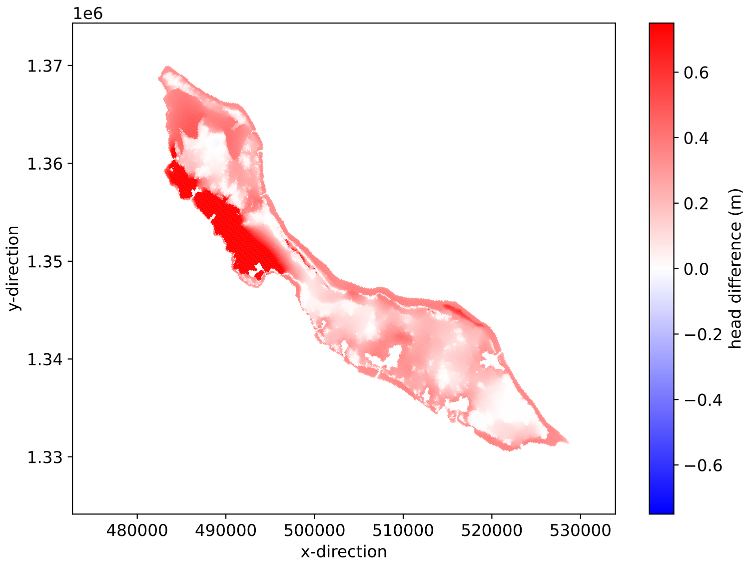

Figure I.2: Difference between simulated heads with the freshwater-only model and simulated heads with the variable-density model.

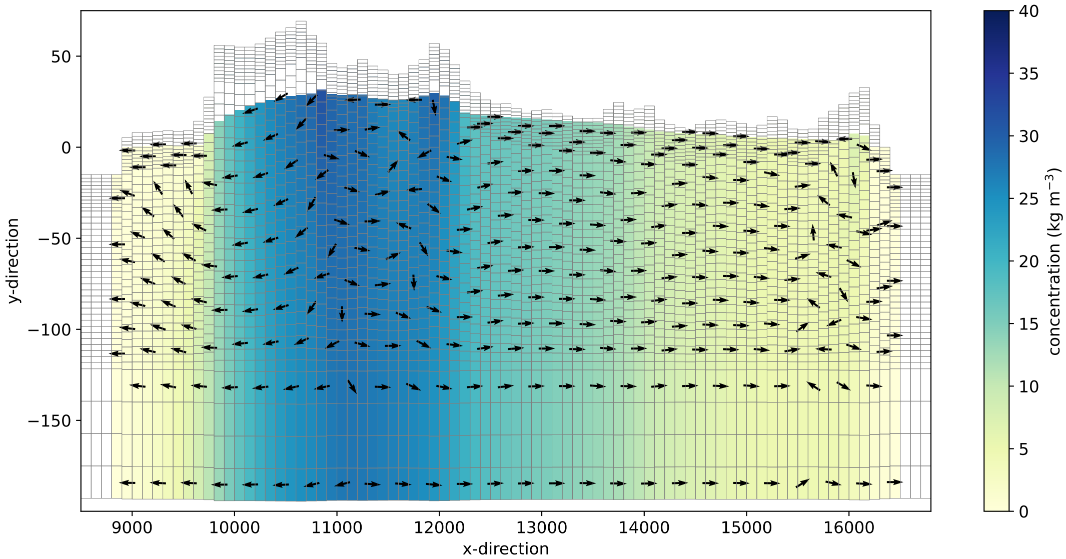

Figure I.3: Cross-section with the colour scale indicating the magnitude of the heads and the vectors indicating the flow directions and their magnitude.

J Steady-state situation check

In the graphs in Figure J.1, the heads over time are visualised at eight different locations. As can be seen, the heads are converging towards steady-state situation after 4500 years. For the locations near the bays and sea, the heads are already at a steady state from the start due to the close location to the constant head boundary condition. Figure J.2 shows the outflow and inflow into and from both the bays and sea against time. As can be seen, the outflows are reaching steady-state.

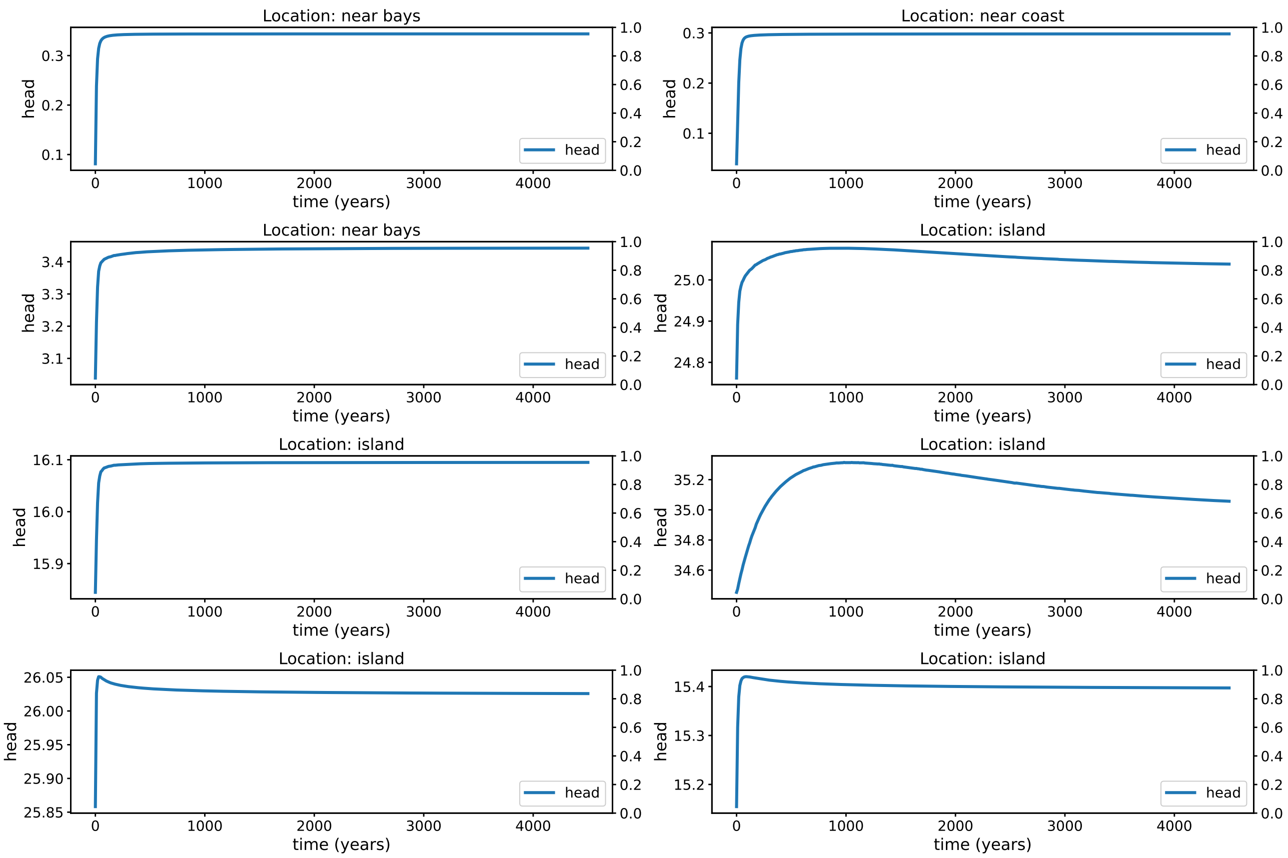

Figure J.1: Evaluation of the head convergence over time for eight different locations on Curaçao, representing different properties, like near a bay, near the sea coast and further inland.

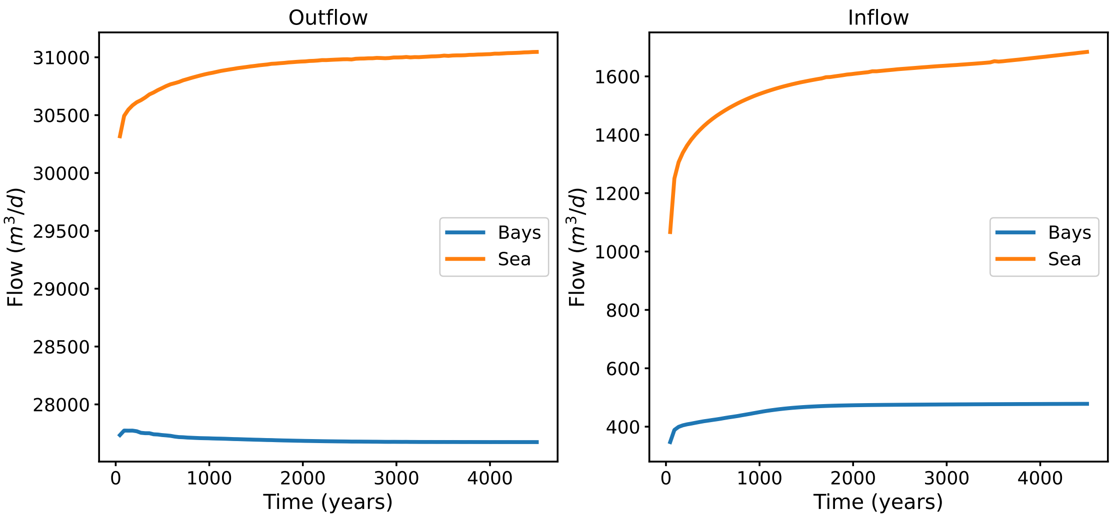

Figure J.2: Outflow to bays and sea and inflow from the bays and sea during the simulation of the variable-density model.

K
Spatial analysis - Tracer with decay and sorption

The results of the decay and sorption tracer:

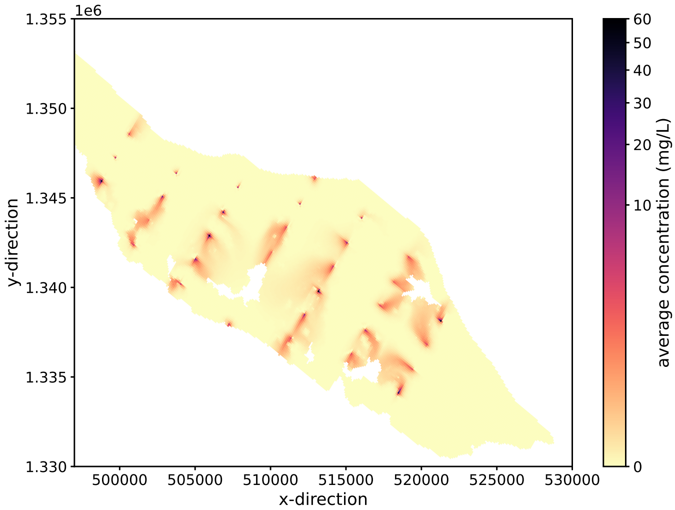

Figure K.1: Average groundwater concentration after 250 years for the tracer with decay (NO_3^-).

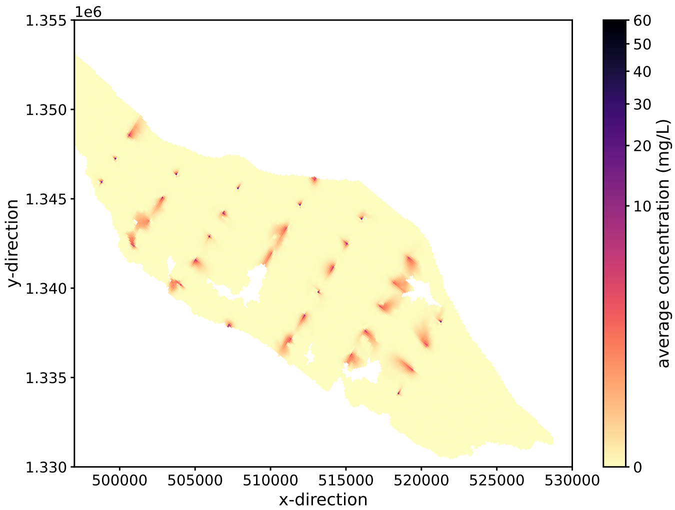

Figure K.2: Average groundwater concentration after 250 years for the tracer with sorption (PO_4^{3-}).

L
Groundwater concentration measurements

Observations of nitrate and phosphate concentrations are done by PhD student Mike Wit on Curaçao. The concentrations are given in the map in Figure L.1a. These were compared to the simulated N and P concentrations.

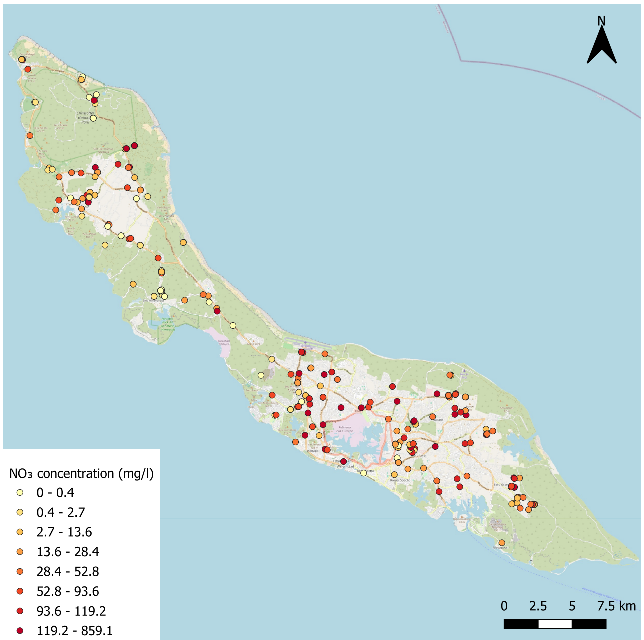

(a) Groundwater measurements of NO_3^- on Curacao.

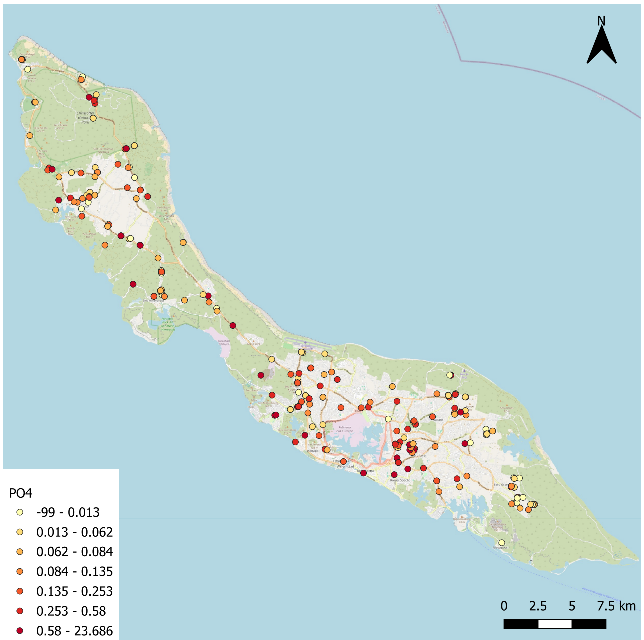

(b) Groundwater measurements of PO_4^{3-} on Curacao.

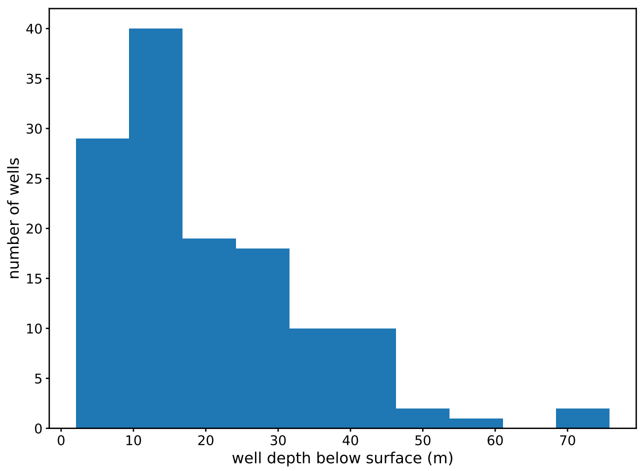

Figure L.2: Histogram of the depth of the wells where a groundwater sample was collected and a depth was reported.

M

Mass fluxes per kilometre coastline

Figure M.1 shows the mass fluxes of the three nutrient transport simulations for the current situations. The mass fluxes are divided by the length of the coast of the zone.

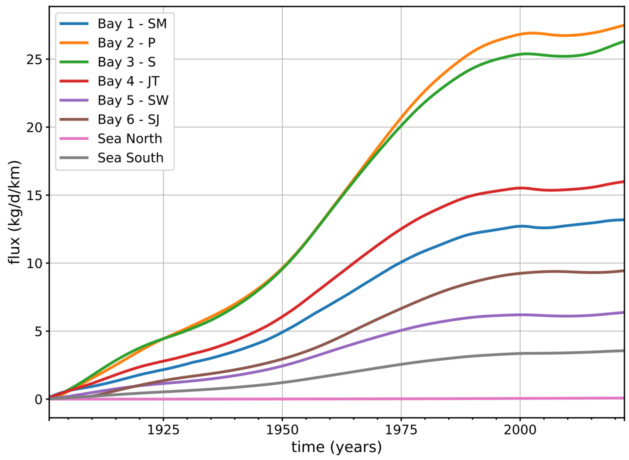

(a) N with conservative behaviour.

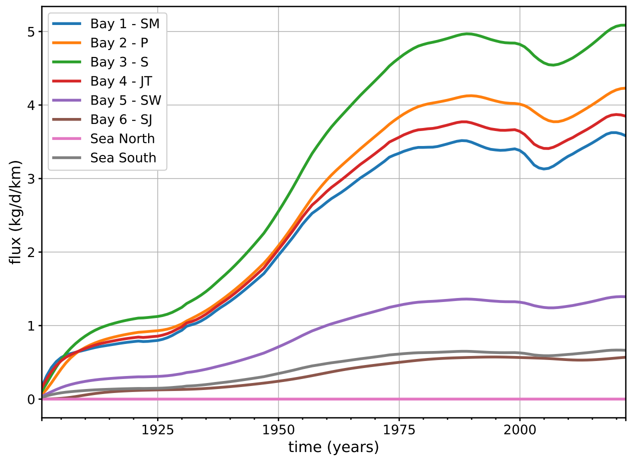

(b) N with decay.

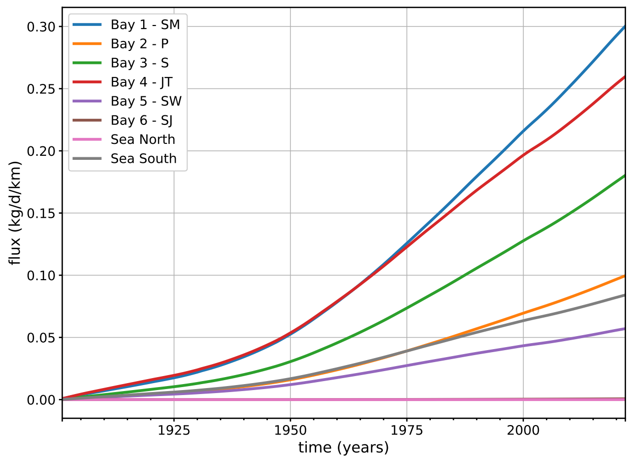

(c) P with sorption.

Figure M.1: Mass flowing into bays/sea coast per day per kilometre coastline for the current situation. Abbreviations for bays: SM = Sint Michiel, P = Piscadera, S = Schottegat, JT = Jan Thiel, SW = Spaanse Water, and SJ = Sint Joris.

N
Concentration future scenarios

Below the average concentrations maps of N and P can be found for the three future scenarios. The concentrations are at the last time step and represent the concentration in 2050.

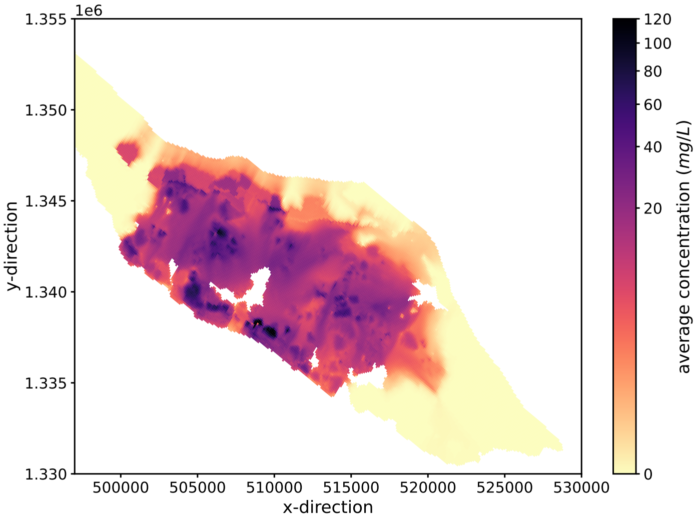

Figure N.1: Average concentration of N for the no-change scenario, modelled as conservative transport. The concentration is averaged over the first 50 m below the surface.

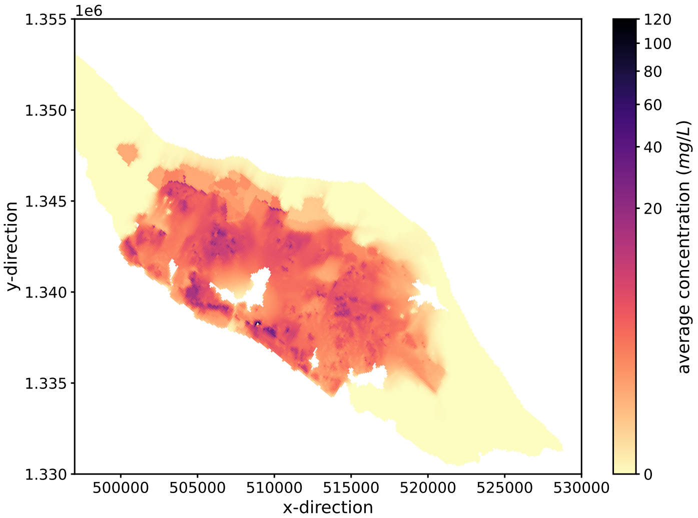

Figure N.2: Average concentration of N for the no-change scenario, modelled with decay. The concentration is averaged over the first 50 m below the surface.

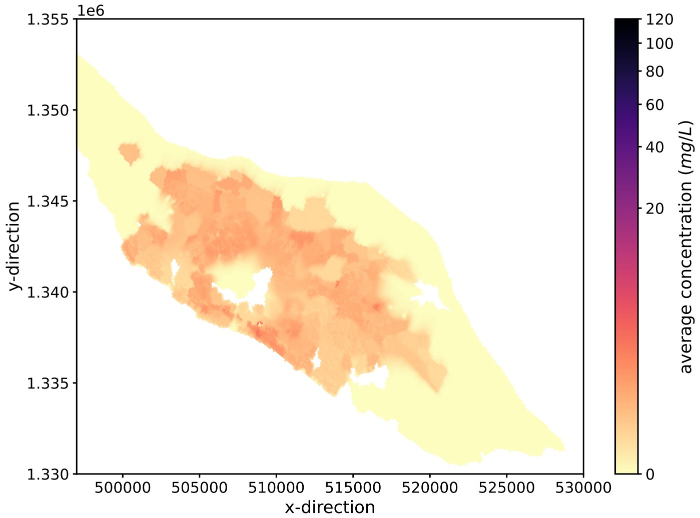

Figure N.3: Average concentration of P for the no-change scenario. The concentration is averaged over the first 50 m below the surface.

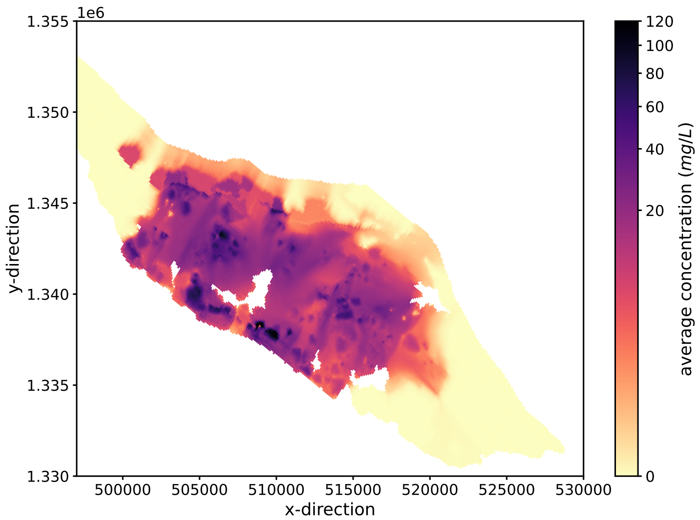

Figure N.4: Average concentration of N for the population growth scenario, modelled as conservative transport. The concentration is averaged over the first 50 m below the surface.

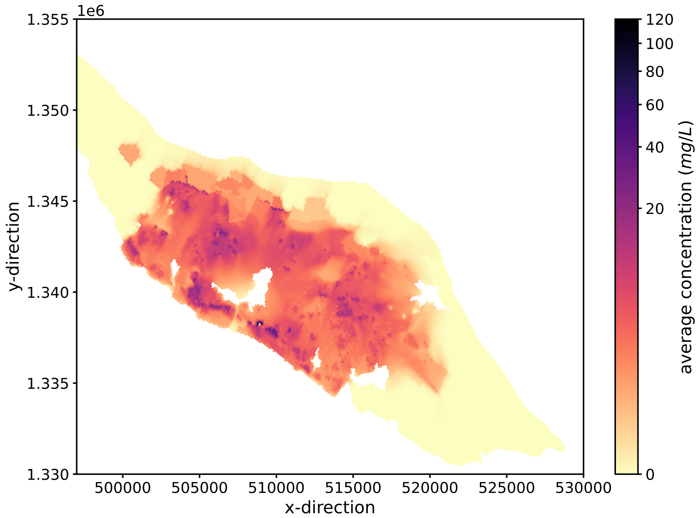

Figure N.5: Average concentration of N for the population growth scenario, modelled with decay. The concentration is averaged over the first 50 m below the surface.

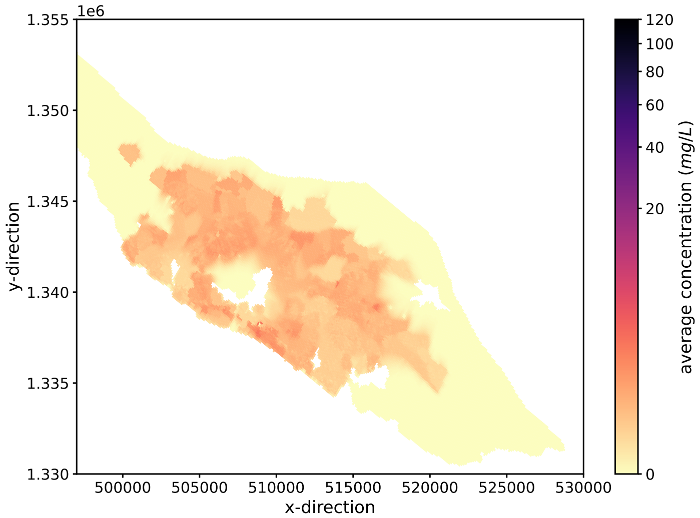

Figure N.6: Average concentration of P for the population growth scenario. The concentration is averaged over the first 50 m below the surface.

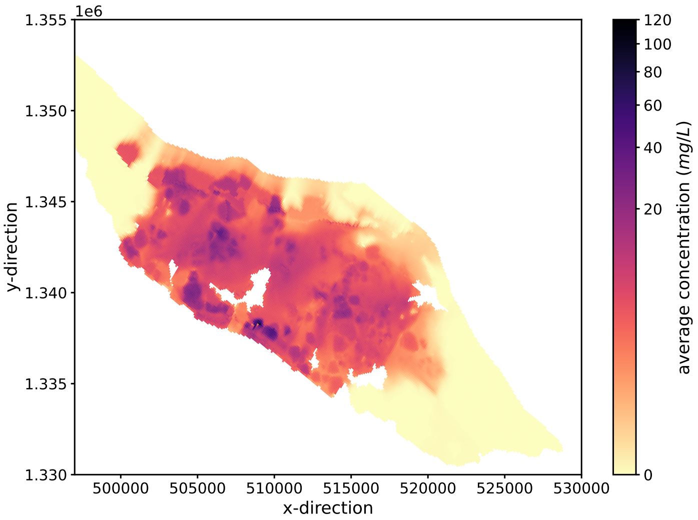

Figure N.7: Average concentration of N for the stopped pollution scenario, modelled as conservative transport. The concentration is averaged over the first 50 m below the surface.

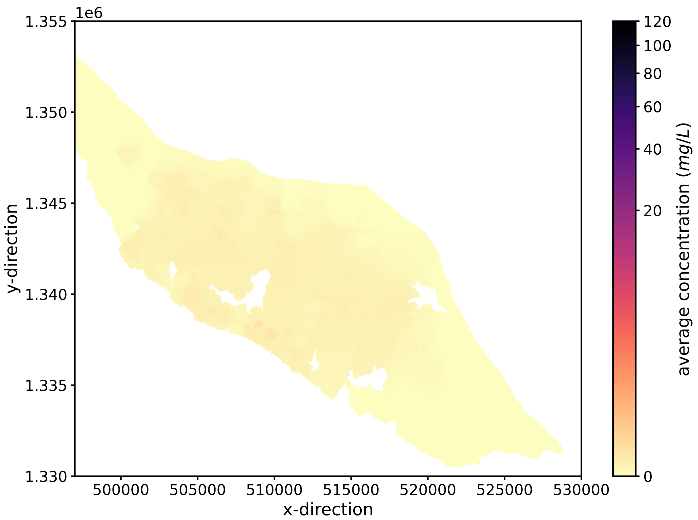

Figure N.8: Average concentration of N for the stopped pollution scenario, modelled with decay. The concentration is averaged over the first 50 m below the surface.

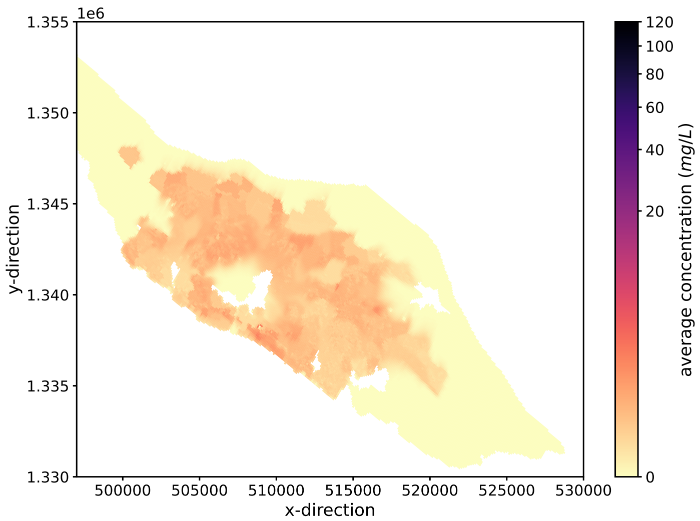

Figure N.9: Average concentration of P for the stopped pollution scenario. The concentration is averaged over the first 50 m below the surface.